Field Emission Energy Distribution (FEED)

J. W. Gadzuk and E. W. Plummer *

National Bureau of Standards, Washington, D. C. 20234

The technique of measuring the energy distribution of electrons which have been field emitted from a cold cathode is considered. The general historical and introductory theory is presented. A survey of the experimental techniques and existing energy analyzers is given. Specific studies on clean metal surfaces in which work functions, band structure effects, surface states, thermal effects, and many-body effects have been studied are reviewed from both the experimental and theoretical points of view. Field emission energy distributions have been particularly valuable in studies of atoms chemisorbed on surfaces. Several theories of enhanced resonance tunneling due to chemisorbed atoms are discussed. Specific systems studied experimentally are reviewed. Inelastic adsorbate enhanced tunneling is also treated.

CONTENTS

1. Introduction 487
2. General Theory 490
2.1. Classical TED—Basic Equations 490
2.2. Transmission Functions 492
2.2a. Matching Wave Function Method 492
2.2b. WKB Approximation 493
2.2c. Miller–Good Approximation 495
2.2d. Zener Effect: Internal Field Emission 496
2.2e. Other Approximations 496
2.3. Standard Results 498
2.4. Transfer Hamiltonian 499
3. Measurement Processes 501
3.1. Field Emission Source 501
3.1a. Electron Trajectory 501
3.1b. Radial Energy Distribution 503
3.2. Energy Analyzers 505
3.3. Data Analysis 508
4. Clean Surface Studies 510
4.1. Single Plane TED 510
4.1a. Work Function 512
4.2. Band Structure 513
4.2a. Experimental 513
4.2b. Theoretical 514
4.2c. Surface States 518
4.3. Thermal Field Emission 521
4.4. Many-Body Effects 523
4.4a. Single-Particle Tunneling 523
4.4b. Multi-Particle Tunneling 525
5. Adsorption Studies 527
5.1. Work Function Changes 528
5.2. Elastic Resonance Tunneling 528
5.2a. Alkaline Earths 535
5.2b. Hydrogen on (100) W 536
5.2c. Oxygen on W 537
5.2d. Krypton on W 538
5.2e. Germanium 539
5.3. Inelastic Tunneling 540
5.3a. Organic Molecules 542
5.3b. Hydrogen 544
6. Addenda 545

1. INTRODUCTION

The emission of electrons from a cold metal upon the application of a strong electric field was one of the earliest confirmations of tunneling as predicted in the new quantum theory of the nineteen twenties (FN28, N28, Op28). Succintly, field emission is the process of applying a large electrostatic field, approximately 30 million volts per cm, to a cold cathode so that the electrons can tunnel from the metal through the classically forbidden barrier into the vacuum. In order to achieve these high fields at reasonable voltages the cathode or emitter is usually etched by a combination of mechanical, chemical, electrical, or thermal processes to a very sharp point (~1000 Å in radius) (M37). Therefore, several thousand volts applied to an anode will produce the desired field at the emitter surface. The invention of the field emission microscope by Müller (M37) made this process a very useful experimental technique. The success Müller obtained with the field emission microscope was a consequence of his realization that if he produced an almost hemispherical tip which was thermally smoothed and cleaned, he could project a greatly enlarged image of the spatial distribution of electrons tunneling from the emitter onto a fluorescent screen. The image on this screen is nearly a stereographic projection of the hemispherical end of the emitter. The dark regions are where the tunneling barrier is higher or wider, i.e., the work function is larger or the field smaller. Likewise, bright regions originate because of low work function or high field.

This process is represented by the potential energy diagram in Fig. 1 and the emitter image is shown in Fig. 2. The surface barrier in the presence of the applied field is shown by the heavy curve which is the sum of V_{image} and V_F. Any electron within the metal with energy ϵ' in an occupied state can then tunnel through the classically forbidden barrier, roughly $0 \leq z \leq s_T$, where s_T depends upon ϵ'. This process forms the basis of the research area loosely referred to as field emission microscopy. There are three different sorts of data that are obtained by this technique, the first two of which we will discuss only briefly and the third of which forms the basis of the review presented here. These measurements are:

(i) Total current as a function of field and surface conditions,

(ii) Field emission micrographs,

(iii) Field emission energy distributions (FEED).

* Present address: Dept. of Physics, University of Pennsylvania, Philadelphia, Pa.

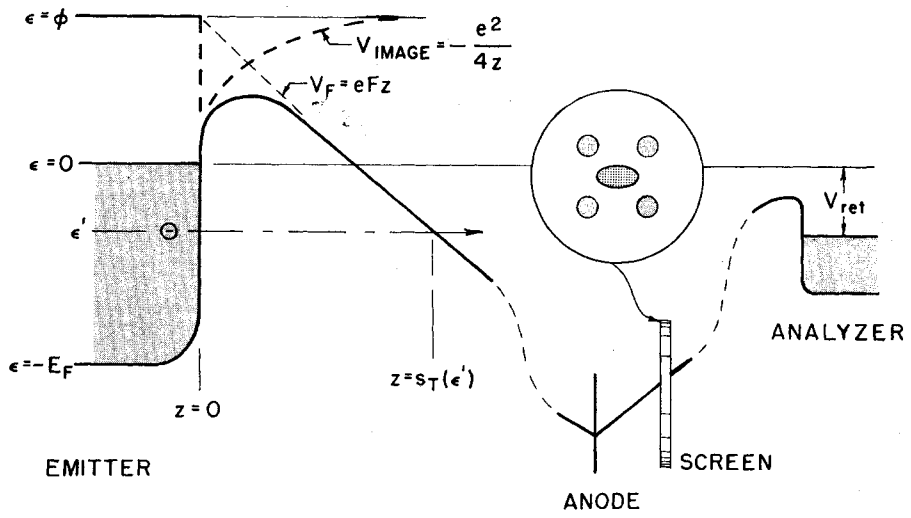

FIG. 1. Schematic surface potential and experimental setup for a retarding potential energy analysis experiment.

An extensive literature exists on measurements of the total field emitted current reaching the screen. As we will see, the measurement of current versus applied field, colloquially referred to as Fowler–Nordheim plots (FN), theoretically should be able to yield work functions of surfaces and also work function changes upon adsorption. Excellent summaries of applications of this method exist (GM56, Go61, SGo65, Oo66, T71, SB72).

It is also possible to obtain very useful information by studying the changes in the field emission pattern as one or more parameters are changed. This is what we refer to as (ii) field emission micrographs. This procedure has been applied successfully to determinations of the relative changes in work function for different crystallographic directions for many adsorption systems (Go61, E66) throughout a wide range of coverage and temperature. Another unique sort of measurement is related to the thermally induced migration of one material over another (Go61, K68). Foreign material is deposited on one side of an emitter. Then the rate of advance of the boundary can be recorded as a function of temperature and crystallographic direction to obtain activation energies for diffusion.

The major object of interest in the present review concerns (iii), the distribution in total energy of the field emitted electrons (Y59, EDK61, Ga69).

The simplest experimental configuration for such measurements is shown in Fig. 1. If a third electrode is placed to the right of the anode (now assumed transparent), then by measuring the collected current as a function of voltage between the analyzer and emitter and differentiating this quantity with respect to the bias voltage one can hypothetically obtain a retarding potential "total energy distribution" (TED) for the hemispherical geometry of a field emission apparatus. It should be quite evident that a TED contains more information related to both inherent properties of the emitter and to the basic tunneling process than either the total current which is an integrated quantity or a micrograph from which it is difficult to obtain quantitative data. It will be one of the major objectives of this article to show how measurement and interpretation of TED's has led to a better understanding of surface and electron emission properties of metals.

Historically, the first observed field emissions must have occurred in many early high-voltage experiments in evacuated containers. The first detailed description was given by Wood (W97) in 1897, who really observed a fireworks in his discharge tube (GM56). Field emission did not progress much either experimentally or theoretically until the late 1920's or early 1930's. The instability and nonreproducibility of experiments coupled with the inability to explain a quantum effect without quantum mechanics delayed any progress. With the development of quantum mechanics and the Sommerfeld electron theory of metals, the theoretical side was immediately clarified by Fowler and Nordheim (FN28, N28). Their end result was the widely used zero temperature Fowler–Nordheim (FN) equation relating the emitted current density J from a metal of work function ϕ_e to the influence of a field F.

In 1931 Henderson and Bodgley (HB31) made the first attempt at measuring an energy distribution of field emitted electrons from a platinum wire. Even though their resolution was very poor they did show that the electrons originated at the Fermi level as Fowler and Nordheim had predicted. Both Dahlstrom, Mackenzie, and Henderson (DMH35) and Müller (M36) used concentric spheres and an emitting point to measure the energy distribution, but again both systems had too low a resolution to accurately measure the total energy distribution. It is a curious fact that Dahlstrom and co-workers recorded in their 1935 paper that what they measured was a total energy distribution. Confirmation of this fact would have to wait nearly twenty five years until Young and Müller (Y59, YM59) built an improved retarding energy analyzer,

capable of measuring the narrow width of the total energy distribution. This observation led to Young's (Y59) calculation of the total energy distribution and subsequently to a calculation by Elinson and coworkers (EDK61).

Not until the 1950's did effort become focussed on the theory of energy distributions. Work such as that of Guth and Mullin (GuMu40) had been directed towards an improved understanding of total current measurements by considering improved transmission functions which have aided TED analysis. Dyke and Dolan (DD56) have reviewed the progress up to the mid 50's. Even though Good and Müller calculated normal energy distributions, their treatment of the transmission function has proven useful in much later work (GM56). Murphy and Good considered the combined effects of thermionic emission and of field emission and the transition between the two regions often referred to as thermal field or TF emission (MurG56). They present examples of the "normal energy distribution" (NED) for various choices of fields and temperatures. The NED is the distribution of kinetic energy associated with the component of momentum perpendicular to the surface and is what is measured in an experiment in which both the emitter and collector are in a parallel plane configuration. It is however not what is measured in the hemispherical geometry of point field emitters. In addition to DD56, GM56, Go61, Oo66, T71, and SB72, this era of field emission has been reviewed in an excellent survey by Müller (M67).

The intent of this article is to present a review of recent work in the area of field emission energy distributions and to indicate some of the significant contributions to solid-state and surface physics that have resulted from such studies. The remainder of the paper takes the following structure. The theory of the field emission process is explored in Sec. 2. Here we try to present the theory as developed historically and in terms of the unified language of the transfer Hamiltonian theory which has proven useful in the theory of junction tunneling (B61, H61, CFP62, AB63, P63, BL69, Du69). The actual measurement techniques are discussed in Sec. 3. A brief discussion of the dominant features of the retarding versus electrostatic deflection analyzers used in FEED studies will be given. Section 4 concerns itself with the applications of FEED studies to the production of useful knowledge of interest to workers both inside and outside the world of field emission. In Sec. 4.1 a brief account is given of clean surface work-function studies and the difficulties encountered using the field emission technique together with the concept of work function. These problems lead us to a discussion of band structure and surface state effects. Thermal field emission (TF emission) is covered in Sec. 4.3. In the course of recent development of the FEED technique, evidence for electron–electron and electron–hole scattering in the solid was obtained in the high-energy tail of a FEED as discussed in Sec. 4.4. Surfaces with adsorbed atoms, partial monolayers, or films are discussed in Sec. 5. What we refer to as classical adsorption studies are briefly discussed in Sec. 5.1. In these studies work function changes due to chemisorption are measured. Adsorbed atoms can affect a FEED in other ways as discussed in Sec. 5.2. Here the role of elastic resonance tunneling through chemisorbed atoms is covered. Inelastic tunneling due to chemisorbed atoms or molecules is treated in Sec. 5.3. In almost all cases, we restrict our considerations to systems in which the field emitter is a metal since this has been the prevalent experimental situation.

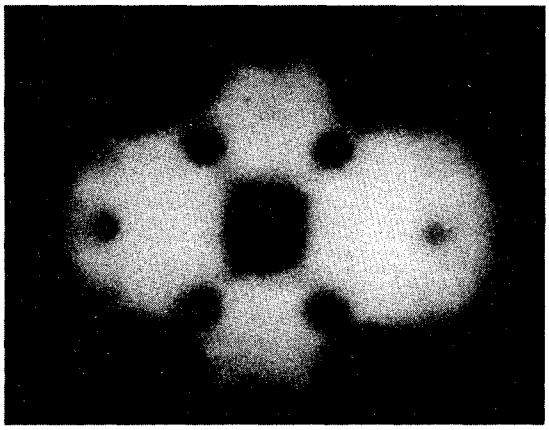

(a)

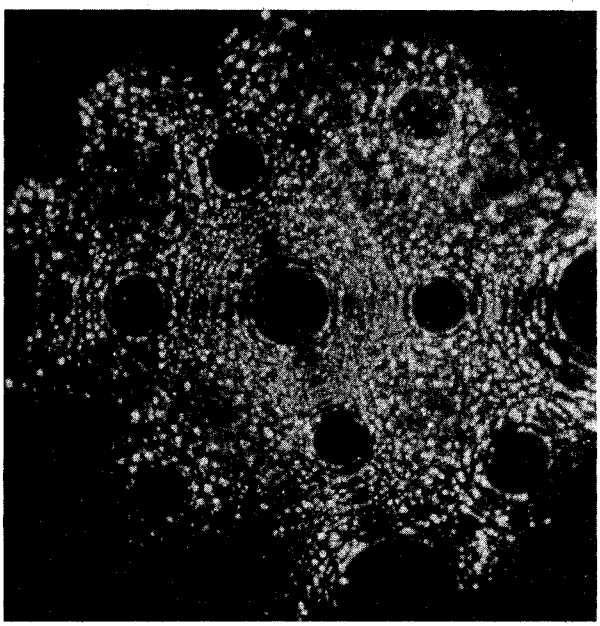

(b)

FIG. 2. (a) Field emission micrograph looking down the (110) plane of a W emitter. The dark (light) regions are high (low) work function or low (high) field planes. (b) Field ion micrograph of the same configuration with the tip cleaned by thermal annealing. (Courtesy of A. Melmed.)

2. GENERAL THEORY

The basic physics of simple field emission is easily illustrated in model calculations on a noninteracting, free-electron-gas metal. However experimentally significant complications arise due to both band structure and many-body effects. These complications have forced workers to seek more comprehensive theoretical models. To illustrate the theoretical developments in field emission, this chapter will be divided into several sections. The classical TED, as envisioned by Young (Y59) and Stratton (S64), forms the basis of Sec. 2.1. The tunneling probabilities for standard surface potentials are discussed in Sec. 2.2 and some useful numerical tables are given. The "standard" results of field emission are given in Sec. 2.3. A reformulation of the problem in terms of the modern transfer Hamiltonian theory of tunneling is the object of Sec. 2.4. This form of the theory will prove especially useful when discussing impurity-assisted tunneling in later chapters.

2.1. Classical TED—Basic Equations

Historically, Fowler and Nordheim (FN28) presented the first derivation of the total current field emitted from cold metals. However, the problem of the energy distribution of the electrons had not received as careful attention as it might have. Workers tacitly assumed that a retarding potential measurement of the energy distribution was a normal energy distribution, within the limits of the free-electron-gas approximation (GuMu40, DD56, MurG56). In 1959 Young (Y59) and shortly thereafter, Elinson, Dubriakova, and Krapivin (EDK61) realized that the geometry of the field emission microscope is such that the total energy distribution (TED) is the observed quantity. Here we will outline the essence of Young's original derivation together with some "band structure" embellishments due to Stratton (S64) and some added features.

The physical situation is as follows: As shown in Fig. 1, an electric field F, typically $\sim$0.2–0.4 V/Å, is applied to the metal, the surface barrier is bent down, and electrons in occupied states of the metal incident upon the surface have a finite probability of tunneling from the metal on the left to the vacuum on the right. In order to treat this mathematically, we must be able to identify some dynamical variables of the electron which remain conserved as the electron goes from the left to the right. Since we are, at this stage, considering only elastic tunneling, the total energy $\equiv E$ should be conserved. For a perfectly smooth surface and a free-electron gas, it is also usually assumed that the two components of the electron transverse k vector $\mathbf{k}_t$ are also conserved since there are no forces acting in the transverse direction during the tunneling process. Thus it would seem reasonable to label the transmission function or tunneling probability by the set of quantum numbers (E, k_x, k_y) or $(E, \mathbf{k}_t)$ and thus the probability of tunneling is of the form $D(E, \mathbf{k}_t)$. Functional forms for D will be discussed in Sec. 2.2. Here we note that only in the free-electron approximation are the total energy E and $\mathbf{k}_t$ simply related to the normal energy W through $W=E+V_0-(\hbar^2/2m)k_t^2$, with $V_0=E_f+\varphi_e$, E_f the Fermi energy, and φ_e the electron work function. Since there is no periodic potential and since the surface potential is assumed to vary only in the z direction normal to the surface, there can be no other coupling between transverse and normal "energy." Consequently, it is reasonable to take $D(E, \mathbf{k}_t)=D[E+V_0-(\hbar^2/2m)k_t^2]=D(W)$, but for free-electron-gas models *only*.

As indicated in the traditional approaches, the TED of field emitted electrons is written as a product of a supply or incident flux function $\equiv N(E, W)$ which depends upon both the normal and total energy, multiplied by the barrier-transmission probability $D(W)$, and then integrated over all normal energies consistent with a total energy E. Schematically this is

$$\frac{dj}{dE} \equiv j' = \int_0^E N(E, W)\, D(W)\, dW, \qquad (2.1)$$

with j' the differential change of current with respect to energy at total energy E. Roughly, the supply function is the product of a Fermi function $f(E)=\{\exp[(E-E_F)/kT]+1\}^{-1}$ times an arrival rate the group velocity $v_z=\hbar^{-1}(\partial E/\partial k_z)$, times a density of states $\rho(E)\sim(\partial E/\partial k_z)^{-1}$ in one dimension. As argued by Harrison (H61), there is an apparent cancellation between the group velocity and the "density of states" resulting in a TED of the form

$$j' \sim f(E) \int_0^E D(W)\, dW.$$

This is the form originally given by Young (Y59). To go further, specific expressions for $D(W)$ must be given. Gadzuk has pointed out (Ga69a) that the cancellation between v_z and $\rho(E)$ is not complete due to the fact that in three-dimensional systems the density of states is given by $\rho=\int |\nabla_k E|^{-1}\, d\mathbf{S}$, where the surface integral is done over a constant energy surface. In this case $v_z\rho$ does not equal a constant and thus, since the tunneling current is proportional to $v_z\rho$, some residual density-of-states information could be contained in the TED.

To quantify these notions we proceed as follows: The number of field-emitted electrons with total energies between E and $E+dE$ is

$$(dj/dE)\,dE = 2ef(E) \int^{E,E+dE} [\hbar^{-1}(\partial E/\partial k_z)] \times D(E, \mathbf{k}_t)[d^3k/(2\pi^3)]. \qquad (2.2)$$

The factor of 2 accounts for spin degeneracy. The differential volume element in k space between the energy surfaces E and $E+dE$ is

$$\iiint^{E,E+dE} \cdots d^3k \rightarrow dE \iint \cdots (d\mathbf{S}/|\nabla_k E|),$$

where the surface integral is done over the constant energy surface E which is a sphere in the free-electron gas. Thus Eq. (2.2) can be written as

$$\frac{dj}{dE} = \frac{2ef(E)}{\hbar(2\pi)^3} \iint D(E, \mathbf{k}_t) \frac{\partial E/\partial k_z}{|\nabla_k E|} d\mathbf{S}.$$

If we define an angle θ' which is the angle between the vector $d\mathbf{S}$ and the z axis, then $d\mathbf{S}$ can be expressed in terms of its projection in the plane transverse to k_z, call it ds, through $\cos\theta' d\mathbf{S} = ds$ as schematically shown in Fig. 3(a). Conveniently, θ' also satisfies $z \cdot \nabla_k E = \cos\theta' \times |\nabla_k E| = \partial E/\partial k_z$, so that with $ds = k_t dk_t d\phi$, Eq. (2.2) assumes the more tracable form

$$\frac{dj}{dE} = \frac{2ef(E)}{\hbar(2\pi)^3} \int_0^{2\pi} d\phi \int_{k_t^{\min}(E,\varphi)}^{k_t^{\max}(E,\varphi)} D(E, k_t, \phi) k_t \, dk_t, \tag{2.3}$$

with $k_t^{\max(\min)}(E, \varphi)$ the maximum (minimum) value of k_t for a given value of E and φ. The integration in the k_t plane extends over all values of k_t falling within the shadow of the energy surface E on the transverse plane. This method of expressing the k_t integration is useful if the actual energy surfaces are slightly perturbed spherical surfaces. Then the integration can be divided into the sum of a spherical energy surface term which does not depend on φ plus a small correction term. A not uncommon type of distorted sphere might be as illustrated in Fig. 3(b). The protrusions could be rough approximations to necks (B63) such as those along the (111) directions in the Fermi surface of Cu or, better still, energy surfaces in alkali metals (L71). Actually for the case of the (111) Cu necks, a hole whose radius is that of the neck is cut out of the middle of the shadow. This would place a nonzero lower limit on $k_t^{\min}$ in Eq. (2.3). As the energy surface in Fig. 3(b) is rotated about the k_y axis, for example, the shadows of the necks in the k_x direction are reduced, thus tending to reduce the upper limit $k_t^{\max}$ in Eq. (2.3) to the value k_t of the unperturbed sphere. More importantly, the projection of the hole at the origin is squashed, reducing $k_t^{\min}$, and effectively increasing the tunneling current.

To proceed, call k_t the radius of the unperturbed sphere in Fig. 3(b). Then in the Stratton model, which does not consider anything but a zero lower limit in Eq. (2.3), the integral is schematically broken up as

$$\int_0^{2\pi} d\phi \int_0^{k_t(E,\phi)} \cdots = 2\pi \int_0^{k_t(E)} \cdots + \int_0^{2\pi} d\phi \int_{k_t(E)}^{k_t(E,\varphi)} \cdots,$$

where the second integral supposedly accounts for the states in the cross-hatched area of Fig. 3(b) but not for any holes in the Middle of the shadow. It is what is often referred to as the "band structure integral" of

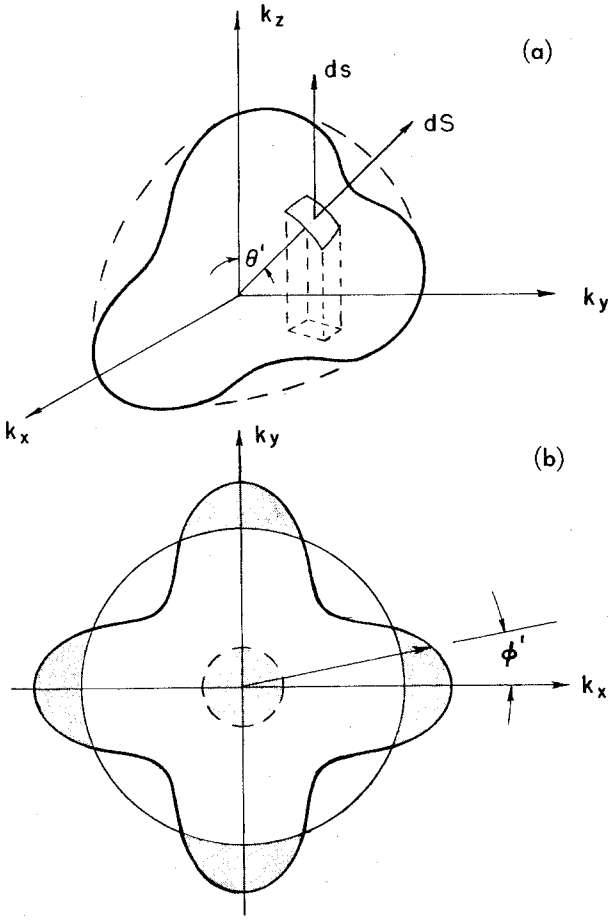

FIG. 3. (a) Schematic distorted spherical constant energy surface. (b) Projection of an energy surface with protrusions in the k_x and k_y direction and a neck in the k_z direction, onto the transverse plane.

Stratton. With these considerations Eq. (2.3) becomes

$$\frac{dj}{dE} = \frac{ef(E)}{\hbar 2\pi^2} \left[\int_0^{k_t(E)} D(E, k_t) k_t \, dk_t + (2\pi)^{-1} \times \int_0^{2\pi} d\phi \left(\int_{k_t(E,0)}^{k_t(E,\varphi)} - \int_{k_t^{\min}(E,0)}^{k_t^{\min}(E,\varphi)} \right) D(E, k_t) k_t \, dk_t \right], \tag{2.4}$$

where we have taken D to be independent of φ. The second group of integrals in square brackets in Eq. (2.4) are the band structure corrections. To go farther, we need functional forms for D. Already we have made a drastic approximation in taking $D \neq D(\varphi)$. The further approximation of taking $D(E, \mathbf{k}_t) = D(W)$ can lead to incorrect results when one tries to account for band structure effects solely in the manner put forth by Stratton. This has been discussed more extensively by Itskovich (I66, I67), Gadzuk (Ga69a), Politzer and Cutler (PC70, P72), and Duke and Fauchier (DuF72) and will be treated in Sec. 4.

For the free-electron gas, we have $D(E,\mathbf{k}_t)=D(W)$, $k_t dk_t=(-m/\hbar^2)dW$ since $dW=-dE_t$ at constant E and thus Eq. (2.4) is simply

$$\frac{dj}{dE}=\frac{4\pi me}{\hbar^3}f(E)\int_0^E D(W)\,dW, \qquad (2.5)$$

which is precisely the form following the discussion after Eq. (2.1). The next section will be concerned with forms for D.

2.2. Transmission Functions

To proceed further we must explicitly consider the barrier penetration probability-D. A myriad of possible theoretical techniques are available for calculating either *exact* transmission functions for *approximate* model problems or *approximate* transmission functions for fairly *exact* models, but needless to say, exact transmission functions for exact models of reality are evasive. Specifically, in this section we will consider the exact wave-matching technique originally used by Fowler and Nordheim (FN28). Then we will consider the more widely used WKB approximation (FrFr65) on both the triangle barrier and the image-rounded triangle barrier. Necessary numerical tables will be supplied. A useful extension of the WKB tunneling probability stated by Kemble (K37) and applied to field emission by Miller and Good (MG53) is discussed. A time-dependent formulation of field-induced breakdown in insulators as introduced by Zener (Z34) is simply related to vacuum field emission. Various improvements on the form of the surface potential by Cutler and co-workers are discussed. The possibility of angular as well as linear momentum-dependent tunneling probabilities is also considered. Lastly, the tunneling matrix element or time-dependent perturbation theory viewpoint is considered. As is well known from elementary quantum mechanics, tunneling, of which field emission is one specific example, is the passage of particles from one side of a barrier to the other without supplying the energy necessary for the particle to go over the barrier. Intuitively one might expect such a process to occur more easily as both the barrier height and thickness are made smaller. In fact the penetrability of the barrier is roughly dominated by an exponential factor $D\sim\exp(-A)$ with $A/2$ the area

$$\int_{s_1}^{s_2} k(z)\,dz$$

under the curve $k(z)=\{(2m/\hbar^2)[V(z)-W]\}^{1/2}$, and with s_1 and s_2 the classical turning points where $V(z)=W$. As will be shown, almost all theories of transmission functions ultimately reduce to such a "phase integral" exponential times some slowly varying pre-exponential of order unity.

2.2a. *Matching Wave Function Method*

The neatest solution to the field emission transmission problem is the exact solution to the triangular barrier in which the surface potential is taken as a step function plus the applied field. Thus for a free-electron gas, the one-dimensional Schrödinger equation must be solved with $V(z)=-V_0\theta(-z)-eFz\theta(z)$, F the applied field, and θ the unit step function. Shifting the origin of the energy scale to the bottom of the conduction band, we have $V(z)=(V_0-eFz)\theta(z)$. Thus in the region of the metal, $z\leq 0$, the solution of

$$-(\hbar^2/2m)(d^2\psi_m/dz^2)-W\psi_m=0,$$

which is required for present purposes, represents a wave of unit amplitude incident upon the surface plus its reflected component: i.e.,

$$\psi_m(z)=\exp(ik_z z)+R\exp(-ik_z z)$$

with $k_z=[(2m/\hbar^2)W]^{1/2}$. For $z>0$, the Schrödinger equation

$$-(\hbar^2/2m)(d^2\psi_f/dz^2)-(W-V_0+eFz)\psi_f=0 \qquad (2.6)$$

must be solved. First we note that if the solutions ψ_f are anything like oscillating functions characterized by a "wave number," $k\sim(W-V_0+eFz)^{1/2}$, then for $W<V_0-eFz$, k is imaginary and the "oscillations" are in fact exponential decays or growths. This behavior could occur for bound electrons ($W<V_0$) in the geometrical domain $0\leq z\leq s_T\equiv(V_0-W)/eF$. This is the classically forbidden region. Once z becomes greater than s_T, k is pure real and we would hope to find a strictly outgoing oscillating wave. As was done by Fowler and Nordheim, Eq. (2.6) is easily reduced to

$$(d^2\psi_f/d\eta^2)+\eta\psi_f=0, \qquad (2.7a)$$

with

$$\eta\equiv(2meF/\hbar^2)^{1/3}\{z+[(W-V_0)/eF]\} \qquad (2.7b)$$

whose solutions are precisely Airy functions (HMF65) or sums of Bessel functions of orders $\pm 1/3$ and $\pm 2/3$. The solution representing an outgoing wave at large z is

$$\psi_f=c(\eta)^{1/2}H_{1/3}^{(2)}(\tfrac{2}{3}\eta_{3/2}),$$

where $H_{1/3}^{(2)}$ is the second Hankel function of order 1/3. From the NBS Math tables (HMF65) one sees that the Hankel function is a representation of the two linearly independent Airy functions $\mathrm{Ai}(\eta)$ and $\mathrm{Bi}(\eta)$ required for a complete solution of Eq. (2.7). Thus the transmitted wave function for $z>0$ is written in the more familiar form

$$\psi_f(z)=T[\mathrm{Ai}(-\eta)+i\,\mathrm{Bi}(-\eta)], \qquad (2.8)$$

where T is the transmission amplitude. In the forbidden region we have $\eta<0$ whereas $\eta>0$ once the electron has passed through the surface barrier and is free. The convenience of the Airy functions is that the total problem can be broken up into only two domains. Consequently only one logarithmic derivative must be matched, at $z=0$, in contrast to a textbook square barrier penetration problem in which there are three regions. In this case, two matchings are done at either

end of the forbidden region (Me61). The disadvantage is that Airy functions do not provide the intuitive feel of sine waves or simple exponentials. To proceed towards a transmission function we need to know the ratio of the asymptotic current in the outgoing waves ψ_f as $z\to\infty$ to the incident current in the wave ψ_m. In general the quantum-mechanical current density in a wave ψ is given by $j=(i\hbar/2m)[\psi(d\psi^*/dz)-\psi^*(d\psi/dz)]$. Again from (HMF65), it is seen that the asymptotic terms of the Airy functions are

$$\mathrm{Ai}(-\eta)\to(\pi^2\,|\,\eta\,|)^{-1/4}\sin(\gamma+\pi/4),$$
$$\mathrm{Bi}(-\eta)\to(\pi^2\,|\,\eta\,|)^{-1/4}\cos(\gamma+\pi/4),$$

with $\gamma=\frac{2}{3}(|\,\eta\,|)^{3/2}$. Consequently the asymptotic form of ψ_f given in Eq. (2.8) is

$$\lim_{z\to\infty}\psi_f(z)=T(\pi^2\,|\,\eta\,|)^{-1/4}\exp[i(\gamma+\pi/4)],$$

which, when inserted in the expression for the current density yields $j_f=(\hbar k_e/\pi m)\,|\,T\,|^2$ with $k_e\equiv(2meF/\hbar^2)^{1/3}$. Similarly the density in the incident part of the wave ψ_m is just $j_0=(\hbar/m)k_z$. The barrier transmission function $D(W)$ is defined as the ratio of transmitted to incident flux. Thus we have $D(W)=j_f/j_0=(k_e/\pi k_z)\,|\,T\,|^2$. The factor T is obtained by demanding that at $z=0$ the wave functions and their derivatives be continuous. Letting $\eta_0\equiv k_e[(W-V_0)/eF]$ and defining

$$x_1\equiv\mathrm{Bi}(-\eta_0)-(k_e/k_z)\,\mathrm{Ai}'(-\eta_0),$$
$$x_2\equiv\mathrm{Ai}(-\eta_0)+(k_e/k_z)\,\mathrm{Bi}'(-\eta_0),$$

the matching procedure then gives the transmission function

$$D_m{}^e(W)=(k_e/\pi k_z)(x_1{}^2+x_2{}^2)^{-1},$$

where the subscript m labels the function obtained by matching and the superscript e labels that the result is exact. In the asymptotic limit of large $-\eta_0$, we have

$$\mathrm{Bi}(-\eta_0)\simeq\pi^{-1/2}\,|\,\eta_0\,|^{-1/4}\exp[\tfrac{2}{3}(-\eta_0)^{3/2}],$$
$$\mathrm{Bi}'(-\eta_0)\simeq\pi^{-1/2}\,|\,\eta_0\,|^{+1/4}\exp[\tfrac{2}{3}(-\eta_0)^{3/2}],$$

and the Ai terms are much smaller. Then the transmission function reduces to

$$D_m{}^e(W)\simeq[4(V_0-W)^{1/2}W^{1/2}/V_0]\times\exp[-(4/3eF)(2m/\hbar^2)^{1/2}(V_0-W)^{3/2}]. \quad (2.9)$$

Typically $\varphi_e\sim4.5$ eV, $E_F\sim8$ eV, and $W\sim E_F$, the pre-exponential term is roughly unity and slowly varying with energy, and is thus taken equal to one. If the quantity $|\,W-E_F\,|$ is small then a convenient expansion of the energy-dependent term in the exponential is

$$(V_0-W)^{3/2}=\varphi_e{}^{3/2}[1-(W-E_F)/\varphi_e]^{3/2}\simeq\varphi_e{}^{3/2}\{1-\tfrac{3}{2}[(W-E_F)/\varphi_e]\}.$$

Since field emission is usually concerned with electrons near the Fermi energy, we have $|\,W-E_F\,|\ll\varphi_e$ and the expansion is valid. With these simplifications, Eq. (2.9) can be written

$$D_m(W)\simeq\exp\{-c_0+[(W-E_F)/d_0]\} \quad (2.10a)$$

with the omission of the superscript labeling the transmission function given by the lowest-order expansion and

$$c_0=\tfrac{4}{3}(\varphi_e{}^{3/2}/eF)(2m/\hbar^2)^{1/2}=0.683\varphi_e{}^{3/2}/F, \quad (2.10b)$$
$$1/d_0=(2\varphi_e{}^{1/2}/eF)(2m/\hbar^2)^{1/2}=1.025\varphi_e{}^{1/2}/F\ \mathrm{eV}^{-1}, \quad (2.10c)$$

when φ_e is given in eV and F in V/Å. This procedure emphasizes both the basically exponential behavior of the transmission function and the simple functional dependence of the controllable variables φ_e and F.

2.2b. WKB Approximation

So much has been written about the WKB approximations that we will assume this to be basic knowledge, aside from a few comments here (Me61; I63,64; FrFr65; Du69). This approximate method is commonly used when $V(z)$ in the Schrödinger equation is such that the Schrödinger equation cannot be reduced to one of the standard equations of mathematical physics. If the spatial variation of the potential is small over an electron wavelength in the classically allowed region or over a characteristic decay length in the forbidden region, then the WKB approximation is useful and valid. For our purposes, the WKB transmission function for a particle of energy W traversing a barrier extending from z_1 to z_2 is given by an exponential of a phase integral

$$D_{\mathrm{WKB}}{}^e(W)=\exp\left(-2\int_{z_1}^{z_2}|\,k(z)\,|\,dz\right)\equiv\exp[-A(W)], \quad (2.11)$$

with $k(z)=\{(2m/\hbar^2)[V(z)-W]\}^{1/2}$. For the triangle barrier in field emission, we have $V(z)=\varphi_e+E_F-eFz$, $z_1=0$, $z_2=s_T=(eF)^{-1}(\varphi_e+E_F-W)$, and the integral is performed exactly yielding

$$D_{\mathrm{WKB}}{}^e(W)=\exp\{-(4/3eF)(2m/\hbar^2)^{1/2}\times[\varphi_e-(W-E_F)]^{3/2}\} \quad (2.12)$$

which is the same exponential obtained in the wave-matching formalism given in Eq. (2.9).

In order that we might construct a theory to compare with experimental results, some of the obvious and severe problems of the triangular barrier in WKB must be dealt with. The problem of concern in this section arises because at zero field the potential at the surface is not a step potential but instead a smoothly varying and continuous function matching onto the interior periodic potential for $z\ll0$ and smoothly going to zero for $z\gg0$. Various treatments for the surface potential have been given (CDa64, CNa65, BeDu69, Du69,

TABLE I. Values of the functions $v(y)$, $s(y)$, and $t(y)$.

y	$v(y)$	$t(y)$	$s(y)$
0	1.0000	1.0000	1.0000
0.05	0.9948	1.0011	0.9995
0.1	0.9817	1.0036	0.9981
0.15	0.9622	1.0070	0.9958
0.2	0.9370	1.0111	0.9926
0.25	0.9068	1.0157	0.9885
0.3	0.8718	1.0207	0.9835
0.35	0.8323	1.0262	0.9777
0.4	0.7888	1.0319	0.9711
0.45	0.7413	1.0378	0.9637
0.5	0.6900	1.0439	0.9554
0.55	0.6351	1.0502	0.9464
0.6	0.5768	1.0565	0.9366
0.65	0.5152	1.0631	0.9261
0.7	0.4504	1.0697	0.9149
0.75	0.3825	1.0765	0.9030
0.8	0.3117	1.0832	0.8903
0.85	0.2379	1.0900	0.8770
0.9	0.1613	1.0969	0.8630
0.95	0.0820	1.1037	0.8483
1	0	1.1107	0.8330

S69, LK70, LK71) but ultimately they all must reduce to the classical image potential when the electron–surface separation is greater than a few screening lengths (Ne69a, Ga70). In fact, theoretical analysis of experimental studies of periodic Schottky deviations (discussed in the next section) indicate that the image potential is valid at e–s separations of the order of tens of angstroms (GuMu40, CGi58, Gr70). Thermal field emission studies (GaP71) indicate that the image potential is reasonable even to distances ~3–4 Å. The surface potential in the WKB phase integral must include the image potential so that now for $z \geq e^2/4(\varphi_e+E_F)$, $V(z)=\varphi_e+E_f-e^2/4z-eFz$, where $z_{\min}$ was chosen by requiring that the image potential, at zero field, matches continuously (with discontinuous slope) to the interior potential $-V_0 \equiv -\varphi_e-E_f$. The remaining problem is to express the phase integral containing the image potential in terms of standard mathematical functions, namely elliptic integrals. This was first done by Nordheim (N28) and discussed further by Burgess, Kroemer, and Houston (BKH53). Their result for the tunneling probability including image potentials is

$$D_{\mathrm{WKB}^e}(W)=\exp\{-(4/3eF)(2m/\hbar^2)^{1/2} \times[\varphi_e-(W-E_f)]^{3/2} \times v[(e^3F)^{1/2}/(\varphi_e-(W-E_f))]\}, \quad (2.13)$$

which is identical with the triangle barrier result except for the $v(y)$ term. This term increases the tunneling probability as it must since part of the barrier present in the triangle model is removed by the image potential. The function $v(y)$ is related to certain elliptic functions, and is numerically presented in Table I. If a small $(W-E_f)$ expansion is made on the exponent in Eq. (2.13) as was done before Eqs. (2.10), then the approximate WKB tunneling probability is

$$D_{\mathrm{WKB}}(W) \simeq \exp\{-c+[(W-E_f)/d]\}$$

with

$$\begin{aligned} c &= c_0 v[(e^3F)^{1/2}/\varphi_e] \\ &= (0.683\varphi_e^{3/2}/F)v(3.79F^{1/2}/\varphi_e), \\ d^{-1} &= d_0^{-1}t[(e^3F)^{1/2}/\varphi_e] \\ &= (1.025\varphi_e^{1/2}/F)t(3.79F^{1/2}/\varphi_e)\ \mathrm{eV}^{-1}. \end{aligned} \quad (2.14)$$

The quantity $t(y)$ is also a slowly varying function and is tabulated in Table I. Equations (2.14) are the "standard" results used in most analysis of field emission data. In principle, the applied field and work function uniquely determine the tunneling probability. In practice, there are some difficulties. It is difficult to accurately determine the effective applied field and more difficult to determine the work function. In the derivation, all aspects of the surface barrier, both the height and the width, have been assumed to be characterized by a single parameter, the electron work function. In fact there are many reasons why caution must be exercised. As defined thermodynamically, the work function is the difference in energy between an electron on the Fermi surface and an electron at rest just outside the surface (HeN49). With this definition, it is irrelevant how the electron got from the metal to the vacuum. On the other hand, in field emission the path is important. For instance if an extra barrier is placed between an electron at the Fermi energy and free space then additional terms in the potential $V(z)$ in the WKB phase integral must be included. This will lead to altered tunneling probabilities in the real physical situation. However if these extra potentials are not included in the mathematical development of the phase integral and one tries to use Eqs. (2.14) to describe the tunneling, then unrealistically large values for the effective work function are often obtained. This is because the field emission "work function" is also being used as a parameter describing the action at each point in the barrier rather than as a difference in energy. Examples of the sorts of barrier possibly causing large field emission "work functions" are the following: (1) Centrifugal barriers due to high angular momentum states such as found in d bands add terms of the type $V_c(r)=\hbar^2l(l+1)/mr^2$. These barriers confine d electrons to tight-binding states in metals like the noble metals (HoEL66) and should similarly further confine d-like band electrons within the metal without changing the work function (Ga69a); (2) Another source of problems has to do with the screening charge induced at the surface by the applied field. Tsong and Müller have discussed screening charge effects in field ion studies in terms of altered apparent work functions

(TM69). Smith has pointed out that the screening charge can account for upwards of 0.5 eV increases in apparent field emission work function due to altered dipole layers (S70). The screening charge could also add thickness to the barrier without changing the thermodynamically defined work function; (3) Patch fields also add their contributions (YC66, PoFe70). On the other hand, if one understands the possible dangers and goes to more detailed theories when the physical situation merits such a move, then Eqs. (2.14) are and have been very useful. A final restriction has to do with the range of validity of these results. Since tunneling is exponentially limited, most of the field emitted electrons come out with normal energy W within d of the highest occupied states, the Fermi level at zero temperature. The expansions in Eqs. (2.10) are on the parameter $|W-E_F|/\varphi_e$ which is small for $W\sim E_F\pm d$ since d typically is $\sim 0.1-0.4$ eV. However with new electrostatic deflection analyzers (KP72), one is able to look at states several electron volts below E_F where the expansion parameter is of order unity and higher-order corrections must be introduced as discussed in the next section.

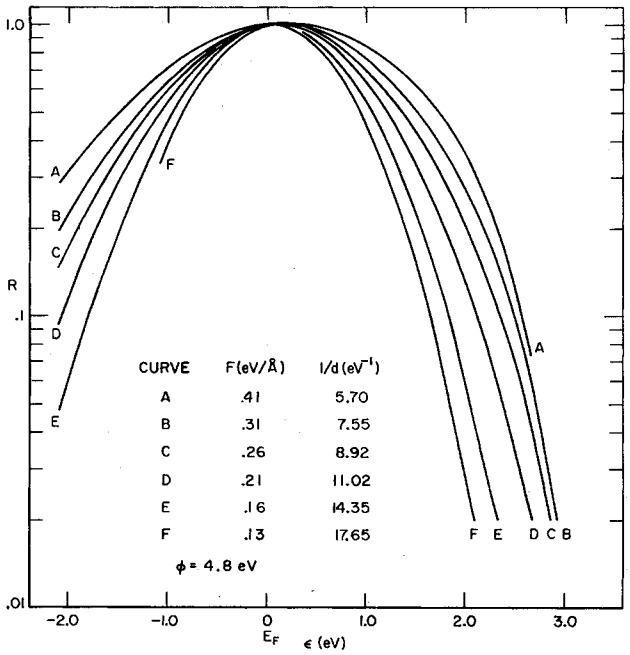

FIG. 4. Ratio of "exact" to expansion tunneling probability as a function of energy from the Fermi level. Field and thus $1/d$ is treated parametrically. (GaP71.)

2.2c. *Miller-Good Approximation*

For tunneling calculations, the rigorous justification for the WKB approximation breaks down in at least three instances. Certainly near the classical turning points where $k(z)\approx 0$ in the phase integral of Eq. (2.11), the spatial variation of the potential is large over a characteristic decay length which goes as $1/k(z)$. This obvious violation of the WKB validity criterion can be dealt with by the so-called connection formulae if the turning point region is "small" compared to the total length of the barrier (K37). The problem of concern here has to do with electrons whose kinetic energies are near the top of the tunneling barrier where the division between transmission over the barrier and penetration through the barrier loses significance. Ideally, the transmission function must go to a constant as $W\gtrsim(E_F+\varphi_e)$, which the WKB function does not do. Also the exponential behavior for $W\sim E_F$ must still remain. Miller and Good have adapted a simple WKB-like expression (K37) to the field emission transmission function which has just these limiting properties. Their generalization of the WKB transmission function of Eq. (2.11) is simply

$$D_{\mathrm{MG}}{}^{e}(W)=\{1+\exp[A(W)]\}^{-1}, \qquad (2.15)$$

where the phase integral $A(W)$ is the same as WKB. Clearly, since A becomes large as W decreases we have $D_{\mathrm{MG}}{}^{e}(W)\to D_{\mathrm{WKB}}{}^{e}(W)$ even for $W\approx E_F$. If one is considering emission near the barrier maximum $W_m=\varphi_e+E_F-(e^3F)^{1/2}=\varphi_e+E_F-3.79F^{1/2}$, then a transmission function with the properties of D_{MG} in which $D(W_m)\to$constant must be used.

It is convenient at this point to consider the overall breakdown of the WKB tunneling probability within the small $|W-E_F|$ expansion approximation. From Eq. (2.5), it is seen that the important quantity in energy distributions is the integral of the transmission function over all normal energies. Thus in Fig. 4 the quantity

$$R\equiv\int_0^E D_{\mathrm{MG}}{}^{e}(W)\,dW\Big/\int_0^E D_{\mathrm{WKB}}(W)\,dW$$

is drawn for some typical field strengths as a function of energy from the Fermi level $\epsilon=E-E_F$. Here $A(W)$ in $D_{\mathrm{MG}}(W)$ is evaluated exactly for each value of W using the numerical results given in Table I and performing the integral numerically. On the other hand, D_{WKB} given by Eq. (2.14) has $v(y)$ evaluated only for $W-E_F=0$ as is the common practice. It is quite apparent that the errors involved in using the WKB expansion are quite small for emission within $\sim\pm 0.5$ eV of the Fermi level but that rather significant deviations occur for larger energies for two reasons. The first reason has to do simply with the fact that the Miller-Good function makes significant corrections for E near E_m which must be included when looking at emission in this energetic region. This correction is insignificant for energies beneath the Fermi energy. The second correction which gives rise to the symmetric appearance of R results from the quadratic term in the expansion of the phase integral of Eqs. (2.13) and (2.14). In the energy region for $|W-E_F|\gtrsim 0.5$ eV, the phase integral

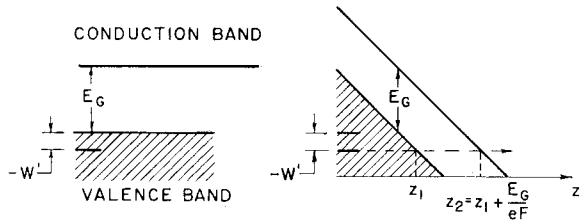

FIG. 5. Model bands as a function of position for field free (left) and applied field (right) configurations of an insulator. The Zener tunneling of the valence band electron at energy $-W'$ into the conduction band is analogous to vacuum field emission with E_G playing the role of work function.

should read

$$A(W)\simeq c-[(W-E_F)/d]+[(W-E_F)^2/g^2]-\cdots.$$

Stratton (S64) has shown that the quadratic expansion term is

$$\frac{1}{g^2}=\frac{0.256}{F\varphi_e^{1/2}}\frac{v(3.79F^{1/2}/\varphi_e)}{(1-3.79F^{1/2}/\varphi_e)}\ \text{eV}^{-2}.$$

Plummer and Young (PY70) have demonstrated that inclusion of such a quadratic term in the tunneling probability can result in good agreement with experimental data.

Before leaving the Miller–Good treatment we should consider the effects neglected in their formulation. By having a constant "pre-exponential," any possible quantum interference effects resulting from extra reflections in regions where the potentials have discontinuous slopes or changing signs in higher derivatives such as $z\sim 0$ or at the barrier maximum $z_m=(e/4F)^{1/2}=1.9/F^{1/2}$ Å are eliminated. This of course is of no real consequence for high-field tunneling emission. On the other hand, for treating low-field thermionic emission over the barrier, in situations were periodic Schottky deviations are expected, a more detailed transmission function than that provided by Miller–Good is required (CGi58, DCo66, Gr70).

2.2d. *Zener Effect: Internal Field Emission*

Although we will not go into much detail here, there is another closely related phenomenon, that of internal field emission first treated by Zener (Z34, K61). Basically the idea is shown in Figs. 5(a) and (b) where an energy level versus position diagram is drawn for an insulator or semiconductor with a bandgap E_G between the valence and conduction bands. Upon application of a field the band edges become tilted in space as shown in Fig. 5(b). Now an electron with energy $-W'$ with respect to the valence band edge can make a transition from the valence to the conduction band not only vertically (requiring an amount of energy $>E_G+W'$) but can also make a horizontal transition into the conduction band due to the action of the applied field. Viewed from another point of view, the valence band electron can tunnel into a current carrying conduction band state. There are a number of different ways to theoretically treat this phenomenon, which has been thoroughly reviewed by Duke (Du69). In all cases the rate limiting factor for electrons making transitions from the valence to the conduction band is an exponential. This result is obtained by solving the one-dimensional time-dependent Schrödinger equation

$$[-(\hbar^2/2m)(\partial^2/\partial z^2)+E_G\cos Qz-eFz-i\hbar(\partial/\partial t)]\psi(z,t)=0, \quad (2.16)$$

where the $\cos Qz$ term is the weak periodic lattice giving rise to the bandgap in the two-band approximation. The two-band, time-dependent wave function is expanded as

$$\psi(z,t)=a_0(t)\exp[ik(t)z]+a_1(t)\exp[i(k(t)-Q)z] \quad (2.17)$$

with $k(t)=k_0+(eF/\hbar)t$. Using the boundary conditions $a_0(t\to-\infty)=1$, $a_1(t\to-\infty)=0$, which say that initially the electron is in the valence band, the probability of tunneling is given by $D=\lim_{t\to\infty}|a_1(t)|^2$. Using standard approximations, it can then be shown that Eqs. (2.16) and (2.17) lead to a valence to conduction band tunneling probability of the form

$$D_{Ze}\sim\exp[-a_0(m^*)^{1/2}E_G^{3/2}/\hbar eF]$$

with the constant a_0 dependent upon the detailed model but always of order unity and m^* an appropriate effective mass. The similarity between this result for internal field emission and Eq. (2.12) for field emission into vacuum is apparent when it is realized that E_G plays the same role as φ_e the work function. In fact with $a_0=4/3\sqrt{2}$ and $E_G\to\varphi_e$, then we have $D_{\text{WKB}}(E_F)=D_{Ze}$, when D_{WKB} is evaluated for the triangle barrier. Viewed as a Zener breakdown, vacuum field emission can be thought of as a process in which electrons make time-dependent, field-induced transitions from the Fermi sea to the tilted conduction band which is the vacuum region.

2.2e. *Other Approximations*

This last section can be regarded as a sort of bouillabaisse of other significant developments in field emission transmission functions.

Cutler and Davis (CDa64) performed calculations for reflection or transmission coefficients for various surface potential barriers with particular emphasis on a model potential $V_s(z)=-e^2/4z+\eta e^2/4z^2$ for $z>z_c$ $[V_s(z_c)\equiv -E_F-\varphi_e]$ which incorporates several new features, namely a minimum in the potential at the surface as first discussed by Bardeen (B36, B40) and the quantum corrections to the image force of Sachs and Dexter (SaDe50). The importance of these corrections is felt through the choice of the numerical parameter η. Cutler and Nagy (CNa65) then applied this potential to the calculation of WKB field emission

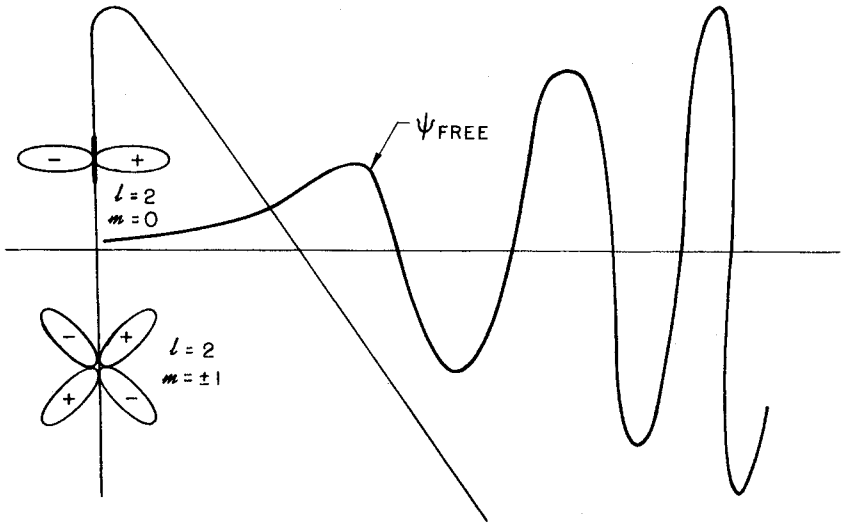

FIG. 6. Schematic diagram of some d-band orbitals overlapping electron wave functions in the vacuum. By symmetry arguments, the $m=\pm 1$ orbitals give zero overlap with Ψ_{free}.

tunneling probabilities. Using the value $\eta=0.0679$ Å, they calculated both normal and total energy distributions and also total current as a function of field (FN plots). The FN corrections are hardly discernible for field strengths $\lesssim 0.35$ V/Å typically used in field emission. With regards to the TED, Cutler and Nagy conclude that "Although small, there is a measurable improved agreement between the computed distributions of the present work and the experimental curves." The numerical nature of the final results preclude any explicit dependency on field and work function. Engle and Cutler (EnC67) have applied the Cutler and Nagy transmission function to a calculation of the anomalous inversion temperature of the Nottingham effect (ChStSM64, SCrCh66). Their result is that, "Although calculable changes generated by the introduction of the modified surface potentials are qualitatively correct, it is nevertheless apparent that the surface effect by itself cannot provide the explanation of experimentally measured values of the inversion temperature."

Another modification to tunneling probabilities has to do with d-band tunneling. Gadzuk has shown that tunneling from the $(n-1)d$ band would be suppressed relative to tunneling from the ns band at the same energy by a factor $\sim 10^{-2}$ due to the extra spatial confinement of the d-wave functions (Ga69a). This occurs for the same reason that d bandwidths are much smaller than s bandwidths. The effect was illustrated by a model calculation using the Oppenheimer perturbation theory of field ionization of atoms (Op28). The relative tunneling probabilities of $(n-1)d$ to ns electrons was given in the Oppenheimer approximation as

$$B(E)=|\langle \text{free}\,|\,eFz\,|\,(n-1)d\rangle|^2\times|\langle \text{free}\,|\,eFz\,|\,ns\rangle|^{-2},$$

where the magnitude of the matrix elements clearly depends upon the overlap of the metal wave function with the free wave function as shown in Fig. 6. Certain magnetic substates give vanishing matrix elements due to symmetry selection rules. Of the allowed states, the $m=0$ state with a large lobe sticking out into vacuum gives the larger contribution (Ob68, Ga69a). The result that $B(E)\sim 10^{-2}$ is consistent with the data obtained with ion neutralization by Hagstrum in which he found d-band tunneling off by as much as a factor of 1/40 relative to s-band tunneling (Ha66). Since the tunneling distance in ion-neutralization is only $\sim$2–4 Å whereas the distance s_T in field emission is $\sim$15 Å, the suppression in field emission would be expected to be greater.

Politzer and Cutler have considered the d-band tunneling from a different point of view in which they perform a wave-matching calculation for the transmission function (PC70, PC72). Ultimately they treat the d-band wave functions in the tight-binding approximation so that the incident state is

$$\varphi=N^{-1/2}\sum_{R_j}\exp(i\mathbf{k}\cdot\mathbf{R}_j)\varphi_n(\mathbf{r}-\mathbf{R}_j)=\exp(i\mathbf{k}\cdot\mathbf{r})u_{nk}(\mathbf{r}),$$

with $\mathbf{R}_j$ the location of the jth atom. This function is matched to an outgoing function of the form given in Eq. (2.8). The final result evaluated for parameters representing nickel is $6\times 10^{-3}<B(E=E_F)<1.5\times 10^{-1}$ which is quite consistent with previous calculations and the ion neutralization results. The results were very sensitive to the position of the matching plane with the smaller limit occurring for the matching plane one lattice constant from the last layer of ion cores, and the upper limit occurring for the matching plane one-half layer from the ion core centers. We feel that the success of free-electron theories of tunneling results from the fact that the tunneling process exponentially filters out current from nonfree-electron-like bands as illustrated here. Thus the measured current results from the free electron part of the electron states and the free-electron theory is successful.

2.3. Standard Results

We have now arrived at the point where all the various pieces of the TED theory can be put together to construct the "standard" results which form the basis upon which most field emission data has been analyzed. The standard result for the TED, first obtained by Young (Y59), consists of inserting the image rounded WKB transmission function, Eqs. (2.14a–c), into the general free-electron gas expression for the TED, Eq. (2.5), and performing the integration to get

$$dj/d\epsilon \equiv j'(\epsilon) = (J_0/d)\ \exp\ (\epsilon/d) f(\epsilon), \quad (2.18)$$

with

$$J_0 \equiv (4\pi med^2/h^3) e^{-c} = (1.537\times 10^{10} F^2 e^{-c})/\varphi_e t^2(y) \quad \text{A/cm}^2$$

and

$$\epsilon = E - E_F.$$

This result is obtained since $j'(\epsilon = -E_F) \lll j'(\epsilon \approx 0)$ and thus the integral is evaluated with the lower limit taken at minus infinity. Note that the energy scale has now been shifted so that the zero is at the Fermi level. The total current is

$$j = \int_{-\infty}^{+\infty} j'(\epsilon)\ d\epsilon$$

which for zero temperature is simply

$$j = J_0. \quad (2.19)$$

Equation (2.19) which is known as the Fowler–Nordheim equation has been the basis of most classical field emission work. When we insert the expressions for c and d and rearrange a bit, the convenient form for analyzing data becomes

$$j/F^2 = A\ \exp\ [-B\varphi_e^{3/2}/F],$$

with

$$A = \{e^3/8\pi h\varphi_e t^2[(e^3F)^{1/2}/\varphi_e]\}$$

and

$$B = (4/3e)\,(2m/\hbar^2)^{1/2} v[(e^3F)^{1/2}/\varphi_e].$$

In principle graphs of j/F^2 vs $1/F$ on semilog paper should allow one to ascertain the work function from the straight line slope proportional to $\varphi_e^{3/2}$.

A few points of note are that the value of the zero temperature TED at the Fermi energy ($\epsilon = 0$) is simply the total current J_0 divided by the slope of the energy distribution d. Due to the strong exponential dependence of J_0 on c, one can also say that the total current is proportional to the slope of the TED at the Fermi level or vice versa. This point will be useful in the section on the interacting electron gas (LeGo70, GaP71a).

Since the value of the field at the emitter tip is hard to obtain unambiguously, Young and Clark have suggested combining the FN data together with the slope of TED to obtain values for the work function in the following manner (YC66, 66a). The field between the emitter and the accelerating anode is determined by the applied voltage which is really the experimentally controllable variable. If patch fields are neglected, then the field is related to voltage as $F = \beta V$ with β some undetermined geometrical factor. It is furthermore assumed that the field distribution over the emitter area seen in the probe hole is constant. Then the slope of an experimental FN curve (j_{tot}/V^2 vs $1/V$) is given by $s_{\text{FN}} = \log_{10} e \times 0.683\varphi_e^{3/2} s(y)/\beta$ with $s(y) = v(y) - y/2dv(y)/dy$ which is also given in Table I. Similarly the slope of the TED is $s_E = \log_{10} e \times 1.025\varphi_e^{1/2} t(y)/\beta V$. Dividing these relations gives the "absolute" work function

$$\varphi_e = -\tfrac{3}{2}(s_{\text{FN}}/s_E)\, V^{-1}[t(y)/s(y)]\ \text{eV} \quad (2.20)$$

in terms of the slopes and the applied voltage. Equation (2.20) must be solved iteratively to get a self-consistent solution since $y = 3.79F^{1/2}/\varphi_e$ in the slowly varying elliptic functions whose values have been given in Table I.

The last item of this section is concerned with the limits imposed upon the TED measurements by the finite resolution of the energy analyzer (YK68, Ga69). Typically a retarding potential analyzer has a resolution of a few tens of millivolts. Depending upon the temperature of the emitter, the leading edge of the TED is smeared out by both thermal effects and instrumental resolution. A criterion for determining the resolution effects on the TED was devised by Young and Kuyatt (YK68). The analyzer smearing is represented by convolving the TED, Eq. (2.18), with a Gaussian instrument function

$$I(\epsilon, \epsilon') = (\sqrt{2}\pi\Gamma)^{-1} \exp\ \{-\tfrac{1}{2}[(\epsilon - \epsilon')/\Gamma]^2\},$$

with Γ the value of $\epsilon - \epsilon'$ for which I has dropped by a factor of e and is related to the full width at half-maximum by $\Delta E_{\text{FWHM}} = 3.44\Gamma$. The observable energy distribution is

$$j_{\text{obs}}'(\epsilon) = \int_{-\infty}^{+\infty} I(\epsilon, \epsilon') j'(\epsilon')\ d\epsilon'. \quad (2.21)$$

Young and Kuyatt numerically evaluated Eq. (2.21) for a number of different temperatures and resolutions. Using Eq. (2.18) in Eq. (2.21), the zero temperature result has been expressed exactly as (Ga69)

$$j_{\text{obs}}'(\epsilon; T = 0) = \frac{J_0}{2d} \exp\ (\epsilon/d)\ \exp\ (\Gamma^2/2d^2) \times \left[1 + \text{erf}\left(\frac{-\epsilon - \Gamma^2/d}{\sqrt{2}\Gamma}\right)\right]. \quad (2.22)$$

Equation (2.22) is drawn in Fig. 7 for a number of different values of ΔE_{FWHM} where the smearing effects on the leading edge are apparent.

Young and Kuyatt then give a numerical graph from which the resolution of the instrument can be obtained from an experimental TED knowing the temperature.

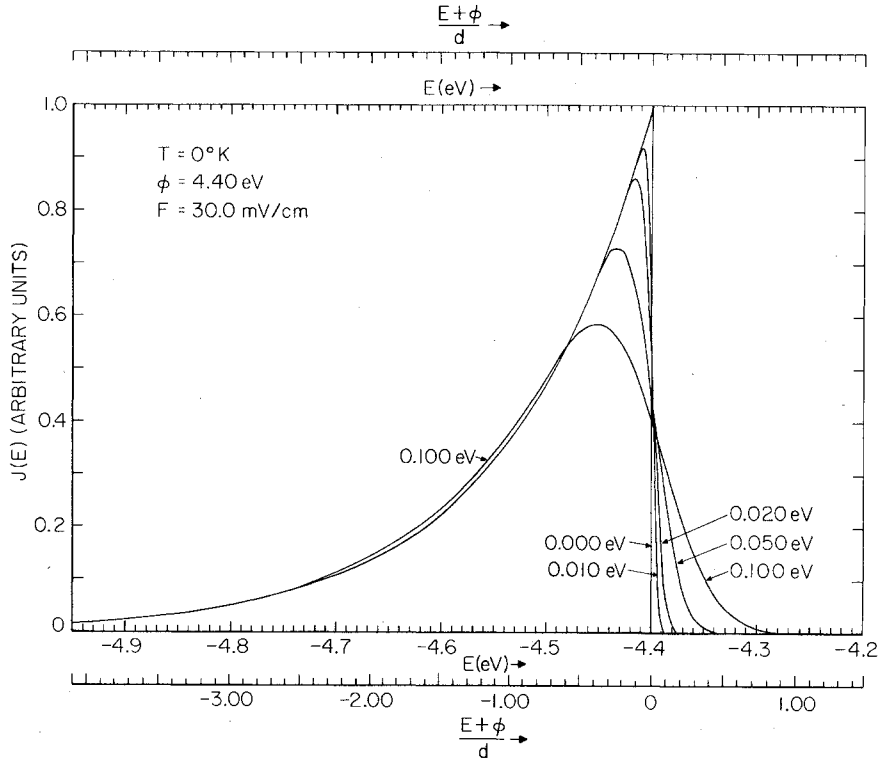

FIG. 7. Theoretical total energy distribution of field emitted electrons from a free-electron metal with various analyzer widths for zero temperature. (YK68.)

From their paper, "since the leading edge suffers the greatest distortion due to the analyzer transmission function, the difference in energy between the 10 and 90% points of the leading edge of the energy distribution has been chosen as the pertinent parameter." Their result is reproduced in Fig. 8 where it is apparent that between 0 and 20.3 K, the analyzer width is approximately equal to the energy difference between the 10 and 90% points. This approximation is particularly accurate in the practical range of available high-resolution analyzers.

2.4. Transfer Hamiltonian

The final topic of general theory deals with the transfer Hamiltonian theory of tunneling which in

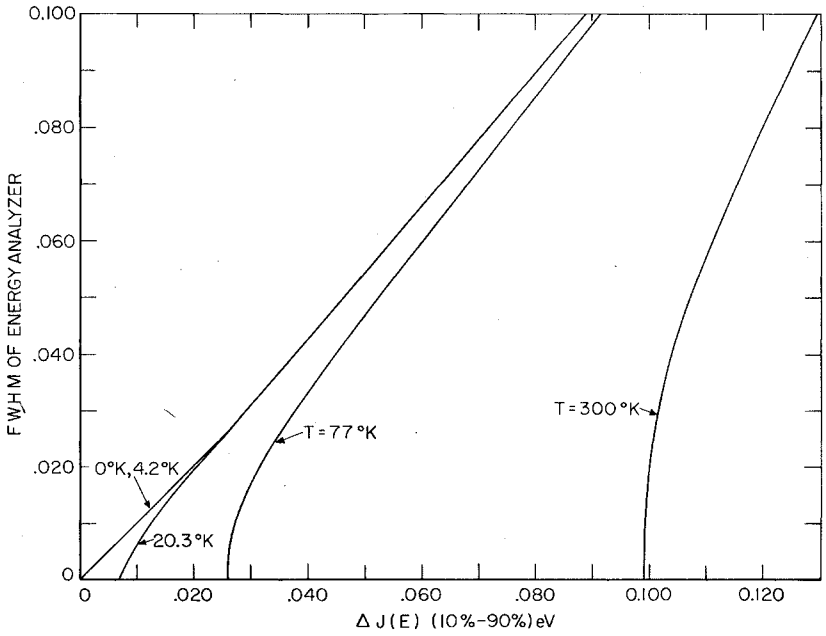

FIG. 8. FWHM of energy analyzer as determined from the leading edge of a TED at various temperatures: FWHM vs measured energy difference between the 10 and the 90% points on the leading edge. Note that $T \ll 300$ K is required for meaningful resolution determination.

many cases reduces simply to the result one would obtain through a naive application of the Golden Rule of time dependent perturbation theory (B61, CFP62, AB63, P63, Du69). The Golden Rule gives the probability per unit time that a particle in the state $|i\rangle$ with energy ϵ_i will make a transition to state $|f\rangle$ with energy ϵ_f when some perturbation H_T that couples the two states is turned on. In its crudest form, the probability per unit time of making such a transition is $w_{i\to f}=(2\pi/\hbar)\sum_f |\langle f|H_T|i\rangle|^2\delta(\epsilon_f-\epsilon_i)$. The total current which results from such transitions is given by the product of an arrival rate $\nu_i(\epsilon_i)$ times a density of states $\rho(\epsilon_i)$ for initial states times an occupation factor $f(\epsilon_i)$ times the transition probability integrated over initial states. Thus we have

$$j=\int \rho(\epsilon_i)\nu_i(\epsilon_i)f(\epsilon_i)w_{i\to f}\,d\epsilon_i$$

and the resulting energy distribution

$$dj/d\epsilon_f\sim\int f(\epsilon_i)\,|\langle f|H_T|i\rangle|^2\delta(\epsilon_f-\epsilon_i)\,d\epsilon_i \quad (2.23)$$

since $\rho\nu\simeq$constant as discussed in Sec. 2.1. This result is convenient since the tunneling is now characterized by a matrix element. However formal difficulties arise since in the transfer Hamiltonian formulation of tunneling the initial state is to the left of the barrier and the final state is to the right. These states are not eigenstates of the same Hamiltonian and thus it is not so clear why the Golden Rule, which describes transitions between orthogonal states of the same Hamiltonian, should be valid for tunneling (P63, ApBr69, Du69). We will now put some of these loose ideas into a more formal framework which will be useful for describing tunneling which involves either many-body effects or adsorbate assistance.

The actual field emission current can be calculated from the transfer Hamiltonian. As outlined elsewhere (ApBr69, BL69) the tunneling current per unit energy is

$$dj/d\epsilon=[4ef(\epsilon)/\hbar]\sum_{\mathbf{k},\mathbf{q}}|\Lambda_{\mathbf{k},\mathbf{q}}|^2\,\mathrm{Im}\,G(\mathbf{k},\epsilon)\times\delta(\epsilon-\epsilon_{\mathrm{fin}}), \quad (2.24)$$

where the sum is over all quantum numbers $\mathbf{k}$ and $\mathbf{q}$ characterizing states localized on the left or right of the barrier and Im G is the imaginary part of the single-electron Green's function or the spectral weight function in the solid. For a noninteracting free electron gas we have $\mathrm{Im}\,G(\mathbf{k},\epsilon)=\pi\delta[(\hbar^2k^2/2m)-E_{\mathrm{Fermi}}-\epsilon]$. On the other hand, if many-body interactions in the solid are important, then the spectral weight function will be more complicated since the metal state which results from the injection or extraction of one physical electron is a mixture of all quasiparticle states. This effect would be reflected in Im G or identically, the spectral weight. The Λ's are configuration space matrix elements of some operator between wave functions of electrons on the left- and right-hand sides,

$$\Lambda_{\mathbf{k},\mathbf{q}}=\int d^3r\psi_{\mathbf{k}}^*(\mathbf{r})T(\mathbf{r})\psi_{\mathbf{q}}(\mathbf{r}). \quad (2.25)$$

In field emission, the right-hand wave function would be a decaying Airy function as z decreases in the region $z\leq s_T$. The left-hand wave function would be either a decaying exponential or Airy function as z increases.

In the Oppenheimer formulation (Op28)

$$T(\mathbf{r})=-eFz \quad (2.26)$$

and the integral of Eq. (2.25) can be readily performed yielding a basically exponential tunneling amplitude.

In Bardeen's (B61) original formulation of many-body tunneling, it was suggested that $T(\mathbf{r})=i\hbar J_{\mathrm{op}}(z)$, where J_{op} is the current operator. With this choice the Λ function becomes

$$\Lambda_{\mathbf{k},\mathbf{q}}{}^B=(\hbar^2/2m)[\psi_{\mathbf{q}}(d\psi_{\mathbf{k}}^*/dz)-\psi_{\mathbf{k}}^*(d\psi_{\mathbf{q}}/dz)], \quad (2.27)$$

where the expression should be evaluated on the plane separating the left from the right side. Harrison (H61) has shown that use of WKB wave functions in Eq. (2.25) leads to a Λ such that

$$|\Lambda_{\mathbf{k},\mathbf{q}}{}^H|^2=(1/4\pi^2)\frac{\delta_{k_t,q_t}}{\rho^R(W)\rho^L(W)}\times\exp\left[-2\int_0^{s_t}k(z)\,dz\right], \quad (2.28)$$

with $\rho^R(W)$ the one-dimensional density of states on the right (left) which is associated with normal energy W.

It can easily be shown that Eq. (2.24) is in fact equivalent to the WKB field emission result in the free-electron gas approximation, Eq. (2.18), if the Harrison matrix element, Eq. (2.28) is used. The utility of the method for our purposes is that j' is now given in terms of matrix elements of a t matrix, $\Lambda_{\mathbf{k},\mathbf{q}}$ of Eq. (2.25), so that we know where to make changes if the static potentials in the barrier are changed, thus affecting the tunneling probability.

The inelastic tunneling is handled in much the same way except that the initial and final states are now product wave functions of the electron $\psi(\mathbf{r})$ and the vibrational (Boson) excitation $\varphi(\mathbf{u})$ wave functions. The initial and final electron states are at different energies and the resulting tunneling matrix element will be of the form of a vibrational matrix element multiplied by an appropriate tunneling matrix element as will be discussed in Sec. 5.

One area of omission in the section has been a discussion of spin-flip tunneling (An66, Ap66, 67) in which the inelastic mode excited could be a localized magnon on a paramagnetic impurity in a magnetic field. In principle this can be treated with the formalism outlined here although in practice the problem is nontrivial (Hee69, Ko69).

At this point the general theory has ended. The

remaining sections will be concerned with the experiments, results, and interpretations in terms of the concepts put forth here.

3. MEASUREMENT PROCESS

In this section we will endeavor to describe what is actually measured in a field emission energy distribution, what types of analyzers are employed, and how the data are analyzed. A classical electron trajectory calculation for spherically symmetric geometry will be presented in Sec. 3.1 (Ev67). The results of this calculation will be utilized to demonstrate what can be measured in a field emission energy distribution. Section 3.2 contains a brief discussion of the various analyzers being used for field emission studies at the present time. Finally, in Sec. 3.3 we will discuss some procedures used by us to analyze energy distributions.

3.1. Field Emission Source

3.1a. Electron Trajectory

Since the time of Young's (Y59) original calculation of the total energy distribution, it has been generally recognized that an electron energy analyzer connected to a field emission source measures a total energy distribution. However, it is useful to point out some of the pitfalls which led to the earlier presumption that normal energy distributions were measured. The problem originates from the initial transverse energy of the tunneling electron. Whether this transverse energy or equivalently the normal component of energy can be measured is the question we hope to answer by the following calculation.

In order to simplify the calculation we will use the spherically symmetric field emission geometry shown in Fig. 9. The emitter is a sphere of radius r_0 and the anode is a concentric sphere of radius R. There is an infinitesimally small hole in the outer sphere in the direction denoted by the unit vector $\hat{n}_0$. This hole is denoted as the "probe hole." In an actual experiment the field emission pattern is manipulated until the projection of the desired crystallographic direction is over the probe hole. Then the electrons passing through this aperture are energy analyzed. The purpose of this section is to calculate which electrons of energy E enter the probe hole and where on the emitter surface they originated. Stated another way, which electrons have the appropriate initial conditions to pass through the probe hole (Ev67)? Herein lies the distinction between what is actually measured and what is usually calculated for a total energy distribution. The instrument in the "probe hole" configuration of Fig. 9 measures the energy distribution of all those electrons which have the appropriate initial transverse energy and origin on the emitter to pass through the "probe hole". The trajectory shown in Fig. 9 illustrates one such condition. Almost all theoretical calculations for the total energy

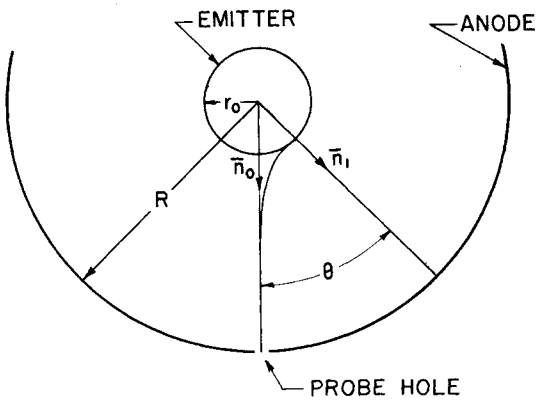

FIG. 9. Spherically symmetric geometry for field emission calculation. A spherical emitter of radius r_0 is concentric with a spherical anode of radius R, with an infinitesimally small probe hole in the $\hat{n}_0$ direction. An electron leaving the emitter at the position indicated by the radial unit vector $\hat{n}$ must traverse an angle θ if it is to enter the probe hole.

distribution calculate the energy distribution for all those electrons tunneling from a given point on the emitter. In other words the actual energy distribution depends on the electron trajectory whereas most theoretical calculations do not. Fortunately, as we will show, they generally reduce to the same answer.

It is clear that we must determine what initial transverse energy E_T is necessary so that an electron originating from a unit area of the emitter determined by the unit vector $\hat{n}_1$ (Fig. 9) will pass through the "probe hole" in the $\hat{n}_0$ direction. Coupling this with the distribution of electrons with total energy E and transverse energy E_T originating from the unit area at $\hat{n}_1$, we can integrate over the emitter surface to obtain all those electrons of energy E which pass through the probe hole.

If V is the applied potential between the anode and the emitter and F_0 is the field at the emitter surface, then the field as a function of r is

$$F(r)=F_0(r_0/r)^2, \tag{3.1}$$

where

$$F_0=(V/r_0)[1-(r_0/R)]^{-1}. \tag{3.2}$$

The potential energy at any r is the integral over r of Eqs. (3.1). Using Eq. (3.2) in Eq. (3.1) we have

$$V(r)=-\int_{r_0}^{r}F(r')\,dr'=r_0F_0\left[1-\frac{r_0}{r}\right]=V\left(\frac{1-r_0/r}{1-r_0/R}\right).$$

The equation of motion in such a central force field can be found in any mechanics book (LL60, P70). The angular momentum M is conserved in a central force field so that

$$M=mr^2\dot{\theta}=\text{const.}$$

The constant is determined by the initial transverse velocity $v_T(r_0)$ so that

$$M=mr_0v_T(r_0).$$

This yields a simple equation for the transverse velocity v_T and transverse energy E_T as a function of r

$$v_T(r)=r\dot{\theta}=v_T(r_0)\,(r_0/r), \tag{3.3}$$

$$E_T(r)=E_T(r_0)\,(r_0/r)^2, \tag{3.4}$$

where $\dot{\theta}$ is the total time derivative of θ measured from n_1.

It is easy to deduce from Eq. (3.4) that the transverse energy is rapidly converted to radial energy because of the conservation of angular momentum. This is the reason that a field emission energy analyzer measures a total energy distribution instead of a normal energy distribution. At a distance of one radius from the emitter ($r=2r_0$) 75% of the transverse energy has been converted to radial energy. At $r=10r_0$ there is only 1% of the transverse energy remaining. When the electron finally arrives at the anode, which is usually at least a few centimeters in radius, it has only about one part in 10^{10} of its original transverse energy. For example, if an electron left the surface with a transverse energy of 1 eV it would have only one-tenth nanoelectron volt of transverse energy at the anode. Meanwhile, its radial energy would have been increased by the applied field, probably by about 10^3 eV. Consequently the ratio of transverse energy to radial energy at the anode would be 10^{-13}.

The radial velocity $\dot{r}$ can be solved using the conservation of energy and angular momentum (LL60, P70) to give

$$\tfrac{1}{2}m\dot{r}^2=E_T(r_0)\left[1-\left(\frac{r_0}{r}\right)\right]^2+eV\,\frac{(1-r_0/r)}{1-r_0/R}\,. \tag{3.5}$$

We have assumed that the radial velocity at the emitter surface is zero. This is not exactly true since the electron is tunneling out of the emitter, but for the purpose of this calculation it is an adequate assumption.

Combining Eqs. (3.3) and (3.5) we can solve for θ as a function of r to find

$$\cos\theta=\frac{1+\{[2E_T(r_0)\,(1-r_0/R)\,](eV)^{-1}\}\,(r_0/r)}{1+[2E_T(r_0)/eV](1-r_0/R)}\,. \tag{3.6}$$

It is apparent from Eq. (3.6) that for $r\gg r_0$ the angle θ does not change much, that is, the motion becomes radial. In a typical situation $eV\gg E_T(r_0)$ and $R\gg r_0$, so Eq. (3.6) can be simplified, especially since we are only interested in the case where $r=R\gg r_0$. With these approximations Eq. (3.6) can be written as

$$\cos\theta\cong 1-(2E_T/eV), \tag{3.7}$$

where we have shortened $E_T(r_0)$ to E_T.

If an electron originating at the position on the surface described by the unit vector $\hat{n}_1$ is to pass through the probe hole in the direction $\hat{n}_0$, then we have

$$\hat{n}_0\cdot\hat{n}_1=\cos\theta\cong 1-(2E_T/eV)$$
$$=1-(\hbar^2k_T^2/2\text{ meV}),$$

where k_T is the transverse k vector at the surface.

Equation (3.7) defines the magnitude of the transverse momentum, but not its direction. For convenience, define a cartesian coordinate system by the three unit vectors $\hat{n}_1$, $\hat{n}_2$, and $\hat{n}_3$ where

$$\hat{n}_2=\hat{n}_0\times\hat{n}_1,$$
$$\hat{n}_3=\hat{n}_1\times\hat{n}_2. \tag{3.8}$$

Then we can define the angle ϕ of the transverse k vector in the plane of the surface at the intersection of the unit vector $\hat{n}_1$ with the emitter surface as

$$\cos\phi=(\mathbf{k}_T\cdot\hat{n}_3)/|\,k_T\,|.$$

Therefore the electron has the proper direction to enter the probe hole when $\phi=0$ or

$$\mathbf{k}_T\cdot\hat{n}_1\times(\hat{n}_0\times\hat{n}_1)=1.$$

Let us define two functions:

$N(E, E_T, \phi, \hat{n}_1)\equiv$ Number of electrons with energy E and transverse energy E_T emitted per second per unit area in the direction ϕ from the area of the emitter denoted by the unit vector $\hat{n}_1$;

$Q(\hat{n}_0, \hat{n}_1, E_T, \phi)\equiv$ Probability that an electron emitted from the emitter surface at $\hat{n}_1$ with transverse energy E_T in the direction ϕ will enter the probe hole at $\hat{n}_0$. The probability is per unit solid angle collected by the probe hole.

With these definitions the number of electrons $P(\hat{n}_0, \hat{n}_1, E)$ entering the probe hole with energy E originating from the unit area at the intersection of $\hat{n}_1$ with the emitter surface is given by

$$P(\hat{n}_0, \hat{n}_1, E)=\int_0^{E_f}\int_0^{2\pi} N(E, E_T, \phi, \hat{n}_1)$$
$$\times Q(\hat{n}_0, \hat{n}_1, E_T, \phi)\,dE_T\,d\phi. \tag{3.9}$$

The total energy distribution $P(\hat{n}_0, E)$ collected per unit solid angle of the probe hole in the $\hat{n}_0$ direction is obtained by integrating over the emitter surface

$$P(\hat{n}_0, E)=\int_0^{\pi}\int_0^{2\pi} P(\hat{n}_0, \hat{n}_1, E)r_0^2\sin\theta\,d\theta\,d\phi. \tag{3.10}$$

Likewise the total energy distribution $P(\hat{n}_1, E)$ of electrons emitted from the unit area denoted by $\hat{n}_1$ is obtained by integrating over all directions of the probe hole ($\hat{n}_0$)

$$P(\hat{n}_1, E)=\iint P(\hat{n}_0, \hat{n}_1, E)\sin\theta\,d\theta\,d\phi, \tag{3.11}$$

where $\cos\theta=\hat{n}_0\cdot\hat{n}_1$ and ϕ is the polar angle measured with respect to the $\hat{n}_0$ axis in Eq. (3.10) and with respect to the $\hat{n}_1$ axis in Eq. (3.11). Equation (3.11) is what is in fact usually calculated for the total energy distribution while Eq. (3.10) represents what is actually measured. If $P(\hat{n}_0, \hat{n}_1, E)$ is only a function of θ

and does not depend on the actual direction of $\hat{n}_1$ or $\hat{n}_0$ then Eqs. (3.10) and (3.11) are equivalent.

The trajectory function can be specified for our simple geometry by using Eq. (3.7) and our coordinate system described by Eqs. (3.8) to give

$$Q(\hat{n}_0, \hat{n}_1, E_T, \theta) = (dE_T d\phi/d\Omega) \times \delta[E_T - \tfrac{1}{2}eV(1-\hat{n}_0\cdot\hat{n}_1)]\delta(\phi)$$
$$= (dE_T d\phi/d\Omega) \times \delta[E_T - \tfrac{1}{2}eV(1-\cos\theta)]\delta(\phi),$$

where Ω is the solid angle of the probe hole. Using Eq. (3.7), we then have

$$dE_T d\phi/d\Omega = \tfrac{1}{2}eV,$$

and therefore

$$Q(\hat{n}_0, \hat{n}_1, E_T, \theta) = \tfrac{1}{2}eV\delta[E_T - \tfrac{1}{2}eV(1-\cos\theta)]\delta(\phi).$$

There is a maximum angle $\theta_{\max}$ defined by the maximum transverse energy $E_T = E$. When $\theta > \theta_{\max}$ Q is 0 where

$$\cos\theta_{\max} = 1 - (2E/eV).$$

It is now easy to present several examples where the actual measured total energy distribution represented by Eq. (3.10) is different from the theoretically calculated distribution of Sec. 2, represented by Eq. (3.11). When the properties of the surface are uniform with the angle θ the function $P(\hat{n}_0, \hat{n}_1, E)$ will depend upon the specific directions of $\hat{n}_0$ and $\hat{n}_1$ and not just on the angle between them. For example, the work function and field are usually functions of θ. This would mean that for electrons with the same normal energy component the tunneling probability would be a function of θ. Also, any band structure effects could cause a discrepancy between the two energy distributions. Consider an electron with energy E and wave vector $\mathbf{k}$ inside the metal. The tunneling probability in the calculation of Sec. 2 would be determined by the component of energy in the $\hat{n}_0$ direction, whereas in the trajectory calculation it would be determined by the component in the $\hat{n}_1$ direction, where $\hat{n}_1$ is determined by E and $\mathbf{k}$.

When the metal is free-electron-like and the geometry is spherical it is easy to show that Eqs. (3.10) and (3.11) are identical. This means that the trajectory calculation gives the same answer as that calculated in Sec. 2. For a free-electron metal N has the form

$$N(E, E_T, \phi, \hat{n}_1) = [2ef(E)m/\hbar^3]D(E, E_T). \quad (3.12)$$

Where the tunneling probability is given by Eq. (2.14) we find

$$D(E, E_T) = \exp\{-c + [(E - E_T - E_f)/d]\}.$$

Using Eq. (3.7) we have

$$D(\theta) = \exp\{-c + [(E-E_f)/d] - (eV/2d)(1-\cos\theta)\}.$$

This gives N as

$$N(E, E_T, \phi, \hat{n}_1) = N(\theta, E) - [2ef(E)m/\hbar^3] \times \exp\left[-c + \frac{E-E_f}{d} - \frac{eV}{2d}(1-\cos\theta)\right].$$

Since N depends only on θ and not on the specific direction of $\hat{n}_0$ or $\hat{n}_1$, it is obvious that Eqs. (3.10) and (3.11) have the same functional form. Also, from Eq. (3.9), we have

$$P(\hat{n}_0, \hat{n}_1, E) = \frac{4\pi ef(E)meV}{2\hbar^3} \exp\left(-c + \frac{E-E_f}{d}\right) \times \exp\left[-\frac{eV}{2d}(1-\cos\phi)\right],$$

and, using Eq. (3.10), find the measured total energy distribution in the direction $\hat{n}_0$ to be

$$P(\hat{n}_0, E) = \frac{4\pi ef(E)meV}{2\hbar^3} \exp\left(-c + \frac{E-E_f}{d}\right) \times \int_0^{\theta_{\max}} \int_0^{2\pi} \exp\left[-\frac{eV}{2d}(1-\cos\theta)\right] r_0^2 \sin\theta \, d\theta \, d\varphi$$

or

$$P(\hat{n}_0, E) = [4\pi ef(E)md(2\pi r_0^2)/2\hbar^3] \times \exp[-c + (E-E_f)/d]. \quad (3.13)$$

This is identical to Young's (Y59) original calculation for the free-electron energy distribution. We have illustrated by this trajectory calculation what is actually measured in a "probe hole" geometry energy analyzer, and how that may differ from the standard total energy distribution. It should be apparent that there will never be any gross discrepancy between these two distributions because the tunneling probability decreases exponentially as θ^2. It is evident also by now that effectively all traces of the transverse energy are lost because of the conservation of angular momentum. We will devote the next section to a calculation of the radial and transverse energy distributions as a function of distance from the emitter.

3.1b. Radial Energy Distribution

The simplest system for observing the field emission energy distribution would be to use the geometry of Figs. 1 and 9 with a spherical retarder after the probe hole and an additional anode so that the aperture caused by the probe hole was in a field-free region and therefore would not act as a lens. This system would then measure the radial component of the energy distribution. What we intend to do in this section is a sort of gedanken experiment. That is, assuming that we can move the probe hole as close as we like, what does the measured energy distribution look like? At what distance from the emitter surface does it look like a

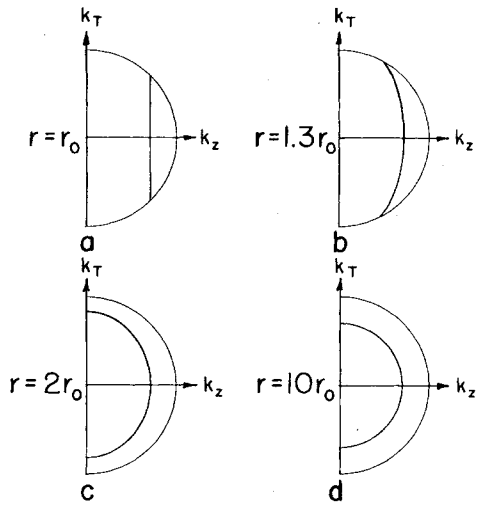

FIG. 10. Two-dimensional diagram of the energy surfaces within a free-electron metal which contribute electrons of energy $\frac{1}{2}E_F$ (E_F is Fermi energy) to the radial energy distribution as a function of the distance of the probe hole from the emitter (Fig. 9). a is for $R=r_0$; b for $R=1.3r_0$; c for $R=2.0r_0$; and d for $R=10r_0$. r_0 is the spherical emitter radius.

total energy distribution? While we are doing this it will be easy to calculate the transverse energy distribution as a function of r.

Let us denote the radial energy distribution by

$$P(E_r, r)\,dE_r \equiv \text{the number of electrons per second with radial energy between } E_r \text{ and } E_r+dE_r.$$

We know from Sec. 2 that for a free-electron one-dimensional tunneling model

$$P(E_r, r)\,dE_r = 2e \int v_z D(W)[d^3k/(2\pi)^3] \quad (3.14)$$

where now we must integrate over an energy surface determined by constant E_r outside the metal. Using Eq. (3.4) of the last section we know the functional form of the transverse energy as a function of the radial distance. At a distance r from the emitter center those electrons with initial transverse energy $E_T(r_0)$ and normal energy W will have a radial energy given by

$$E_r = W + E_T(r_0)[1-(r_0/r)^2]. \quad (3.15)$$

Therefore the integral in Eq. (3.14) must be over all electrons with normal and transverse energy inside the metal which satisfies Eq. (3.15), that is, over an energy surface of constant E_r. Figure 10 illustrates, for a free-electron metal, this energy surface in k space for $r=r_0$, $1.3r_0$, $2r_0$, and $10r_0$ and an energy $E_r=\frac{1}{2}E_f$. In these drawings the z axis is the direction of emission. When $r=r_0$ the integration is performed over constant normal energy W (GM 56). Therefore the energy surface is a disk whose axis is the k_z or normal direction. Incidently it is easy to see from Fig. 10(a) why the normal energy distribution goes to zero at the Fermi energy at low temperatures. The size of the disk decreases to zero as W goes to E_f or as $k_z \to k_f$. As r increases [Figs. 10(b), (c), (d)] the energy surface gradually becomes more spherical until at $10r_0$ [Fig. 10(d)] it is within $\sim 1\%$ of being a sphere of constant total energy E, i.e., $P(E_r)$ is a total energy distribution.

We can evaluate Eq. (3.14) using these limits of integration and the following identity from Eqs. (3.15) and (3.4)

$$v_z = \hbar^{-1}(\partial E/\partial k_z) = \hbar^{-1}(\partial E_r/\partial k_z).$$

Then we have

$$P(E_r, r) = [2e/\hbar(2\pi)^3] \int_{E_r \text{ const}} f(E) D(W)\, dk_x\, dk_y.$$

We can simplify this by writing k_x and k_y in cylindrical coordinates, integrating over the angle and transforming from k_t to E_t as was done in Sec. 2 to get

$$P(E_r, r) = (4\pi me/h^3) \int_{E_r \text{ const}} f(E) D\{E_r - E_T(r_0) \times [1-(r_0/r)^2]\}\, dE_T(r_0).$$

The tunneling probability was given by Eq. (2.14) and the limits of integration for E_T are from 0 to $E_{\min}$. The radial energy distribution is then given by

$$P(E_r, r) = \frac{4\pi me}{h^2} e^{-c} \left(\frac{E_r - E_F}{d}\right) \int_0^{E_T(\min)} - \frac{\exp[-E_T(r_0)/d][1-(r_0/r)^2]}{1+\exp\{[E_r - E_F + E_T(r_0)(r_0/r)^2](kT)^{-1}\}}\, dE_T(r_0).$$

To simplify this integration consider the zero temperature limit only. Then the limits of integration are from 0 to $E_T(\min)$ where

$$E_T(\min) = \min\left[\frac{E_F - E_r}{(r_0/r)^2}, \frac{E_r}{1-(r_0/r)^2}\right].$$

The first situation occurs when the energy surface of integration intersects the Fermi energy [Fig. 10(b)]. The second case results when $k_z=0$. The resultant radial energy distribution is

$$P(E_r, r) = \frac{4\pi me}{h^3} \frac{(-1)d}{1-(r_0/r)^2} \left[\exp\left(-c + \left(\frac{E_r - E_F}{d}\right)\right)\right]\left\{\exp\frac{-E_T(\min)[1-(r_0/r)^2]}{d} - 1\right\}.$$

When r approaches r_0 the distribution is the normal energy distribution

$$\lim_{r\to r_0} P(E_r, r)$$
$$= (4\pi me/h^3)(E_F - W)\exp\{-c+[(W-E_F)/d]\}.$$

Likewise as $r\to\infty$, $P(E_r, r)$ goes to a total energy distribution

$$\lim P(E_r, r) = (4\pi me/h^3)\exp\{-c+[(E-E_F)/d]\}.$$

In Fig. 11 we have plotted $P(E_r, r)$ for the four values of r_0 used in Fig. 10. In Fig. 12 we have shown the equivalent transverse energy distribution for values of r used in Fig. 10 which is given by

$$P(E_T, r) \propto e\left[-c\frac{(r/r_0)^2}{d} - E_T\frac{(r/r_0)^2}{d}\right].$$

By now we hope it is clear that a normal energy distribution cannot be measured unless the probe hole is very close to the emitter or the aberrations in the electron optics are sufficiently small so that a Gaussian image of the tip can be formed with less than 1 part in 10^{13} distortion. This does not seem very realistic; surely none of the analyzers presently being used in this field come anywhere close to that. In fact, none of the analyzers we will discuss in the next section can measure any component of a normal energy distribution.

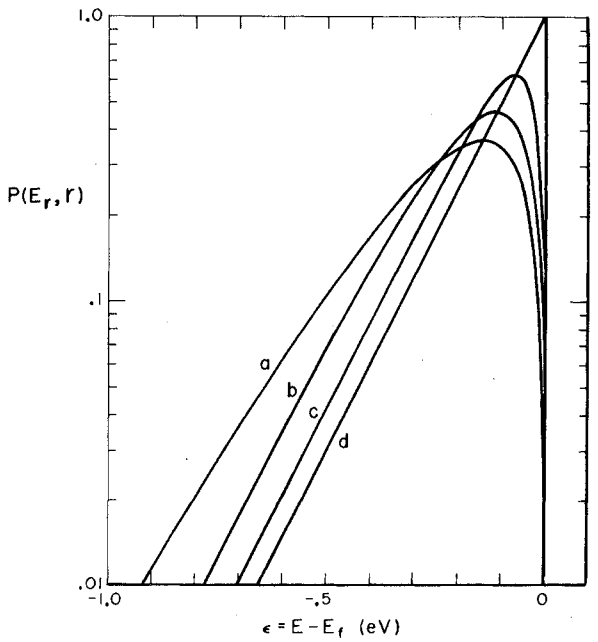

FIG. 11. Radial energy distribution $P(E_r, r)$ as a function of the distance from the emitter surface. Curve a is for $r=r_0$; b for $r=1.3r_0$; c for $r=2.0r_0$; and d for $r=10r_0$. r_0 is the spherical emitter radius. Curve a is a normal energy distribution and d is a total energy distribution.

3.2. Energy Analyzers

In this section we will give a brief description of the various energy analyzers which have been used to measure total energy distribution. Our objective will be to outline the advantages or disadvantages of each design and indicate through proper references where more detailed information can be found. All of the designs we will consider begin with the field emission projection geometry (M37) where the spatial image of the electrons tunneling from the tip is projected onto a fluorescent screen. A small hole usually denoted as the "probe hole" is cut in the screen through which the electrons of interest pass to be subsequently energy analyzed. The "probe hole" is usually stationary and the field emission pattern is deflected until the appropriate crystallographic region is over the probe hole.

There are several techniques for deflecting the field emission pattern relative to the "probe hole." These fall in three categories: (1) magnetic deflection, (2) electrostatic deflection, and (3) mechanical manipulation. The image of the tip must be maintained on the optical axis of the system independent of the scheme used. Magnetic deflection (YM59, Oo66, SwCr66, SwCr67) has two distinct disadvantages when applied in an energy analyzer system. It is very difficult to shield the analyzer from the magnetic field and the pattern moves when the voltage is changed to take a Fowler–Nordheim plot. The electrostatic deflection system (PY70) solves both of these problems but introduces other complications. Small electronically isolated deflection plates must be mounted near the tip and electrical connection must be made through the vacuum chamber. Some small degree of mechanical manipulation is usually needed with both magnetic and electrostatic deflection to position the effective source on the optical axis. After the emitter is originally positioned on this axis the additional motion needed to compensate for the magnetic or electrostatic deflection is usually small. The third alternative of mechanical manipulation is experimentally complicated. Basically the tip can be moved on a gimbal system which is internal or external to the vacuum system, the tip being at the center of this gimbal system. Schmidt and Gomer (ScGo66) have developed the internal gimbal system for Fowler–Nordheim total current work and Workowski and Czyzewski (WoCz71) have utilized it in an energy analyzer. As far as we know, Whitcutt and Blott (WhBl69) and Shepherd (Sh69) have the only analyzers utilizing an external gimbal system. Ordinarily it is very difficult to have an external gimbal system and still maintain adequate visibility of the field emission pattern.

The first energy analyzer used to successfully measure a total energy distribution was the retarding analyzer developed by Young and Müller (YM59) and shown in Fig. 13(a). Even though this analyzer was the first to have sufficient resolution to properly record a total

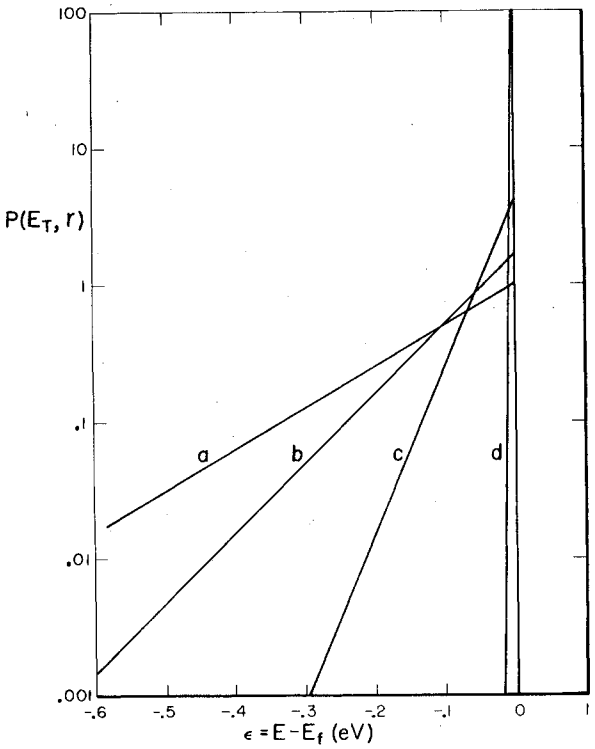

FIG. 12. Transverse energy distribution $P(E_T, r)$ as a function of the distance from the emitter surface. Curve a is for $r=r_0$; b for $r=1.3r_0$; c for $r=2.0r_0$; and d for $r=10r_0$. r_0 is the spherical emitter radius.

energy distribution and was also reasonably simple to construct, it has several disadvantages as pointed out by Young (PY70). These are: (1) secondary electron emission from the retarding elements, (2) poor sensitivity, and (3) a long time constant. Also there is no provision for deflecting the field emission pattern. Young's solution to these problems was a cylindrically symmetric retarding analyzer [Fig. 13(b)] where the radially diverging electron beam from the emitter is collimated beneath the imaging screen forming a parallel beam. This beam is retarded by a series of rings and a 1000-line/in. flat mesh followed by an accelerating lens and an electron multiplier. A cylindrical geometry was chosen by Young so that a very fine mesh could be supported. The emission pattern is deflected by electrostatic plates. This analyzer system furnished much of the early work (PGaY69, PY70) which substantiated the tunneling resonance predictions of Duke and Alferieff (DuAl67).

All of the other retarding analyzer designs used today are spherically symmetric. The most popular design is that of van Oostrom (Oo66) which has been modified slightly by Swanson and Crouser (SwCr67). The design of this instrument is shown in Fig. 13(c). This analyzer employs what we might class as strong electron optics in contrast to Young's weak optics. That is, the electron beam passing through the "probe hole" in the anode encounters a strong lens creating a crossover near the center of the hemispherical collector. Therefore the electrons have nearly normal incidence on the collector surface. This analyzer suffers from sensitivity problems because it does not employ an electron multiplier. Both Whitcutt and Blott (WhBl69) and Workowski and Czyzewski (WoCz71) have solved this problem by placing a hemispherical grid in place of all or part of the collector. The electrons passing through this grid are then accelerated into a multiplier. The problem with this system is that the beam is diverging radially after passing through the spherical mesh. It must then be focused onto the electron multiplier. Workowski and Czyzewski used an accelerating grid and Whitcutt and Blott apertured their system. Whether they can collect all the electrons as the mesh potential is changed to record an energy distribution cannot be ascertained from the data presented in their publications, but they are not having any major problems.

There is one spherically symmetric analyzer incorporating an electron multiplier which has been tested sufficiently to know that it operates successfully. This is the analyzer used by Lea and Gomer (LeGo71) and

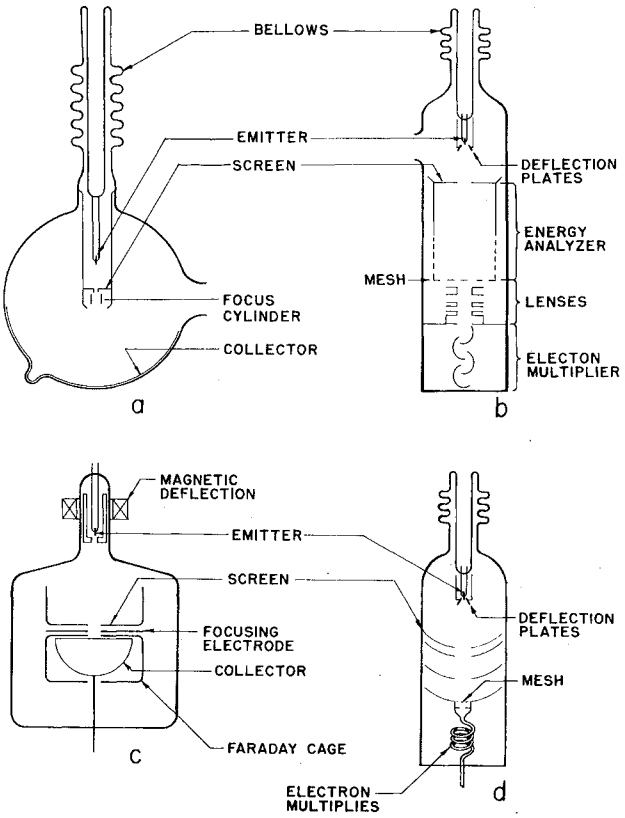

FIG. 13. Schematic diagrams of four common retarding energy analyzers. (a) Spherically symmetric analyzer of Young and Müller; (b) Cylindrical analyzer with multiplier developed by Young; (c) Spherically symmetric van Oostrum-type analyzer; and (d) Spherically symmetric analyzer used by Lea and Gomer.

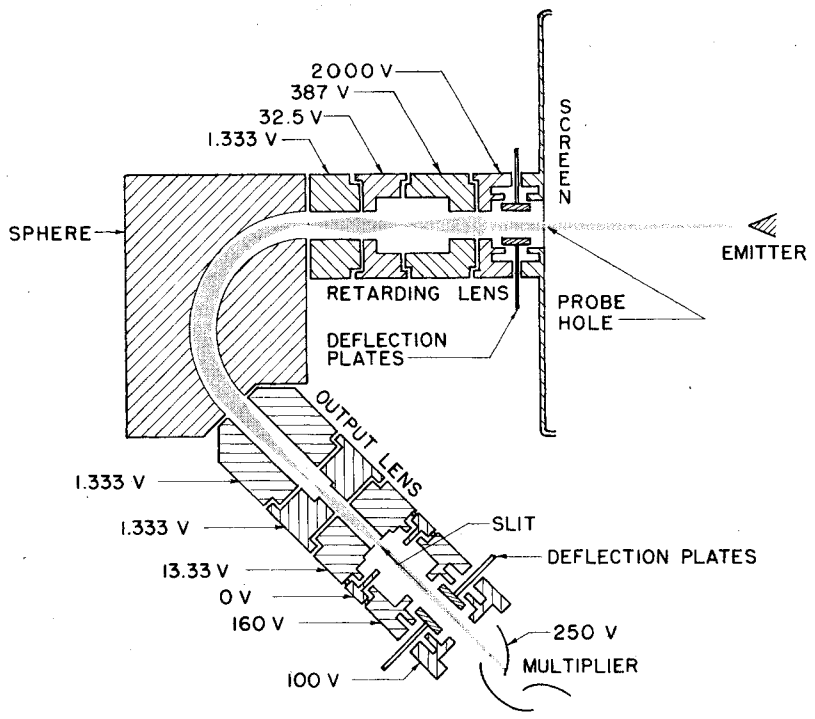

FIG. 14. 135° spherical deflection analyzer adaptation to a field emission source. The potentials on the lenses are the design voltages for a 2000-V emitter and 0.020-eV resolution.

shown in Fig. 13(d). It is a concentric spherical shell type, first described by Swanson and Crouser (SwCr68). It is possible in a system consisting of two concentric spheres to image the electron source at the center by repositioning the source, as pointed out by Simpson (Si61). Lea and Gomer added two intermediate hemispherical shells to maintain spherically symmetric geometry. All of the analyzer systems utilizing both an electron multiplier and electronic differentiation about which there is sufficient information available to evaluate their performance appear to work equally well. Both Lea and Gomer, with a spherical analyzer, and Plummer and Young, with a cylindrical analyzer, could achieve about 0.030-eV resolution and a current range of nearly three orders of magnitude. There are claims of better resolution but they were usually made before a legitimate criteria for resolution was developed by Young and Kuyatt (YK68) and in many cases the curves were hand differentiated. The original version of the cylindrical analyzer was three times larger than the one used by Plummer and Young (PY70) although both had the same mesh size. The PY version achieved a resolution of less than 0.020 eV.

Every retarding analyzer suffers from the same inherent limitation. It measures the integral of the desired energy distribution and the signal must be differentiated. Measurement of field emission energy distribution is especially difficult with a retarding analyzer because the number of low-energy electrons is exponentially less than that of those with the highest energy near the Fermi energy. The adaptation of a deflection energy analyzer to a field emission source would eliminate the shortcomings of a retarding analyzer. The analyzer should give a resolution of a few tens of milli-electron volts at an anode voltage of a few thousand volts and should be sufficiently versatile to allow operation over a wide range of energies and resolution. Also the luminosity of the system must be large enough to obtain reasonable signals.

The resolution ΔE of a deflection energy analyzer is proportional to the electron energy times the product of the entrance and exit slit widths (or the vertical width) and the inverse of the effective radius of the electrons in the analyzer (Si64, KSi66, KSi67). In the field emission case the initial energy is $\sim 10^3$ eV so that adequate resolution ($\sim$0.020 eV) can be achieved by either using a very large radius with small slit widths or retarding the electrons before they enter the analyzer. The two-deflection energy analyzers now being used for field emission studies are of the electrostatic spherical deflection type, with preliminary electron retardation (Sh69, KP72).

A schematic drawing of the Kuyatt and Plummer analyzer is shown in Fig. 14. In order to reduce the size of the ultrahigh-vacuum system it was decided to use a spherical deflector of mean radius 1.0 in. In order to maximize the product of area and solid angle (luminosity) of the system for the design conditions, the spherical deflector must be operated at the lowest possible energy. With the additional condition that the electron beam fill only two-thirds of the gap between the hemispheres, by use of the design equations previously

given (Si64, KSi66, KSi67), it was determined that the analyzer energy should be 1.33 eV for 0.020-eV resolution at 2000-V anode potential. The maximum beam diameter at the entrance to the hemispheres and the equivalent exit slit width should be 0.015 in. and the half-angle of divergence of the beam at the entrance to the hemispheres should be 0.08 rad.

Because a 180° spherical deflector placed the electron multiplier detector too close to the field emission source, a 135° spherical deflector was used. As can be seen from Fig. 14, this choice gives adequate spacing between the detector and emitter. The 135° deflector gives a magnification of 1.414 as compared to 1.0 for the 180° deflector. Since the energy dispersion is also increased, by a factor of 1.207, the equivalent exit slit should be 0.018 in. As in the previous designs by Simpson and Kuyatt (Si64, KSi66, KSi67) a 10 to 1 accelerating lens with a magnification of 0.667 is used to image the exit beam onto the actual exit slit. This slit therefore should be 0.012 in. wide. Finally, a Soa lens (Si61) is used to focus electrons emerging from the exit slit onto the first dynode of an electron multiplier.

The decelerating lenses reduce the electron energy from the anode potential to 1.33 eV such that the electron beam entering the analyzer satisfies the constraints discussed in the previous paragraphs. Since the decelerating ratio is quite large, it was decided to use three stages because little is known of the properties of lenses at voltage ratios greater than about 25. A nonlinear least-squares computer program was used to adjust the lens diameters, positions, and voltages so as to minimize the base width of the analyzer using first-order focal properties. This optimization procedure produced the lenses shown in Fig. 14, which for a 2000-V anode potential should result in a half-width of about 0.020 eV. The experimental results confirmed these estimates. Examples of the data obtained with this instrument will be given in the following sections.

The other spherical deflection energy analyzer being used for field emission energy distribution studies was designed by Shepherd at the University of Minnesota (Sh69). In his design the field emitter is in the center of an anode, spherical mesh, and spherical screen with a "probe hole" in the screen. The screen itself is used to retard the electrons. The retarded electrons which pass through the "probe hole" drift along a 0.3-in.-long drift tube before encountering the entrance aperture which is 0.040 in. in diameter. The potential across the aperture varies as $1/r$. The spherical deflector used by Shepherd had a mean radius of 1.25 in. An energy distribution was obtained by fixing the pass energy of the spherical deflector and sweeping the potential between the emitter and the analyzer input. This method of sweeping changes the brightness of the source, inversely proportional to the retarding voltage.

The only disadvantage of this system is the method of retardation. By using the screen as the retarding element coupled with the "probe hole"–drift tube–entrance aperture as the collimating element the luminosity of the system is considerably reduced. It is also very likely that scattering from the two apertures and the drift tube will cause spurious results when data are being taken far from the Fermi energy, or when the measured current is much less than the total current passing through the probe hole. There is not sufficient published data at present to properly evaluate this analyzer.

3.3. Data Analysis

In this section we will describe a method of data analysis used by us to extract the pertinent information from a measured total energy distribution. The reason that some sophistication is needed in data analysis is that nearly every total energy distribution from a metal looks the same at the first glance. The one exception to this statement seems to be the hump in the energy distribution from the (100) faces of tungsten and molybdenum (SwCr66, 67). It should be clear from the theoretical treatment of Sec. 2 that as long as there are any electrons in the specimen capable of tunneling, the predominant features of the total energy distribution result from the shape of the barrier that the electrons tunnel through. Nearly all of this barrier is in the vacuum region outside the metal where the electron's behavior is surely free-electron-like. An oversimplified but illustrative model would be one where all electronic properties of the solid and its surface were pre-exponential to the exponential tunneling probability. In other words, the statement that the total energy distribution in field emission is free-electron-like basically is not a statement about the properties of the substrate but about the behavior of electrons in a barrier in free space. We will illustrate this statement with data later in this section to show that the part of the total energy distribution which depends on the electronic properties of the substrate is not free-electron-like.

The problem in data analysis is to remove from the measured energy distribution the part which is due to the tunneling barrier. This can be accomplished by dividing the measured energy distribution $j'(\epsilon)$ by a calculated free-electron energy distribution $j_0'(\epsilon)$. This gives us an enhancement factor $R(\epsilon)$ as a function of energy

$$R(\epsilon)=j'(\epsilon)/j_0'(\epsilon). \tag{3.16}$$

If the measured energy distribution is free-electron and the calculation of j_0' is correct, $R(\epsilon)$ will be a constant equal to one. Any structure in the $R(\epsilon)$ curve will be a consequence of the nonfree-electron behavior of the measured energy distribution or the assumptions used in calculating $j_0'(\epsilon)$. The assumptions we use in calculating $j_0'(\epsilon)$ have been given in Sec. 2.

With these assumptions the free-electron energy distribution $j_0'(\epsilon)$ is given by Eq. (2.5) where the precise form of the tunneling probability D as a function of normal energy W is detailed in Sec. 2.2. It was

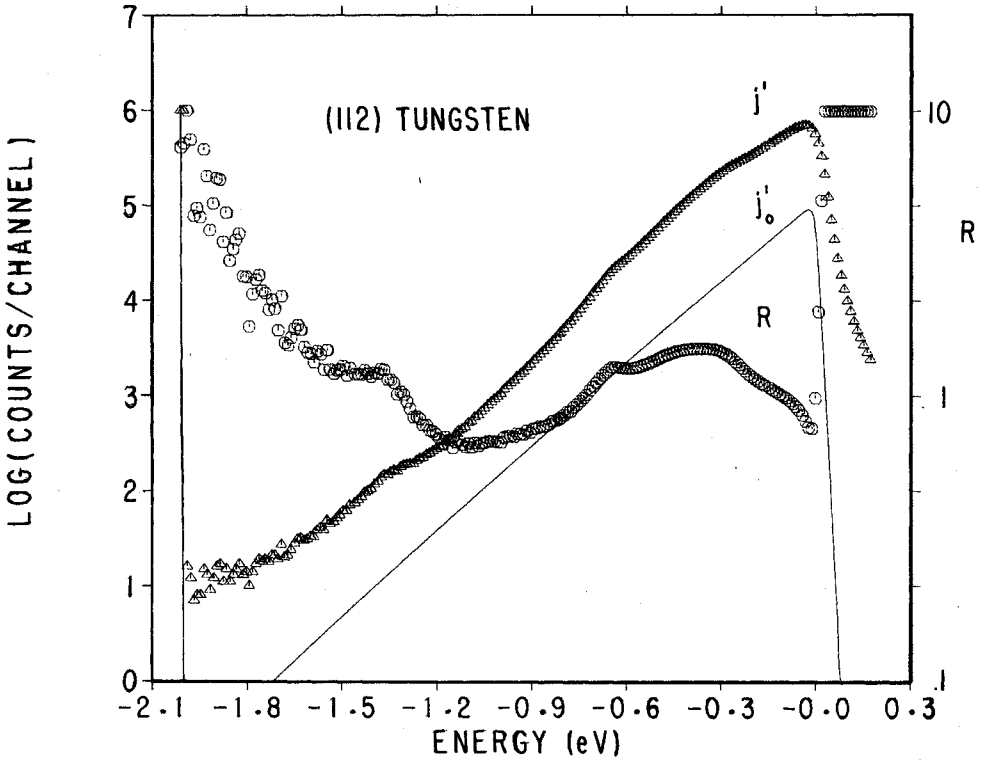

FIG. 15. Example of the data processing system. $j'(\epsilon)$ [△] is the measured energy distribution for (112) tungsten at 78 K as accumulated in 256 channels of a multichannel analyzer with 0.010 eV per channel. $j_0(\epsilon)$ [—] is the calculated energy distribution for a work function $\varphi = 4.90$ eV and a field calculated from the Fowler–Nordheim plot. $R(\epsilon)$ [⬡] on the right-hand scale is calculated by dividing j' by j_0' for each energy. R was arbitrarily normalized to equal 10 at $\epsilon = -1$ eV.

shown in Fig. 4 that the ordinary expansion of $D(W)$ about E_F cannot be used because it can introduce large discrepancies in the $R(\epsilon)$ curve. For example (see Fig. 4), if the work function is 4.8 eV and the field 0.21 V/Å, then $R(-1.)/R(0)=0.5$, even when $j'(\epsilon)$ is an ideal free-electron energy distribution. We calculate $j_0'(\epsilon)$ using either the Miller–Good transmission function, Eq. (2.15), or an expansion of $D(W)$ [Eq. (2.13)] about $W-E_F=\epsilon$. Either of these calculations must be done numerically and yields nearly equivalent results.

The tunneling probability is a function of the work function and applied field F. The work function for a clean surface is taken from other measurements on macroscopic crystals, whenever possible from the absolute measurements of the type used by Strayer and Swanson.[1] Using this work function the field is then calculated from the slope of the Fowler–Nordheim plot [see Eq. (2.19)]. When adsorption systems are being studied the change in the work function is calculated from the changes in the Fowler–Nordheim plot. Once the work function and field have been obtained for a given situation a free-electron energy distribution $j_0'(\epsilon)$ is calculated and divided into the measured energy distribution $j'(\epsilon)$. At the present time we cannot measure exactly the areas being sampled and the collection efficiency of the analyzer. Thus there is an arbitrary normalization constant introduced. For example, the constant might be chosen so that $R(0)=1$. To avoid the effects of this constant log R is plotted vs energy ϵ.

Figure 15 shows an example of the computer data analysis program. The measured energy distribution as recorded on a multichannel analyzer from the spherical deflection analyzer is shown as j'. This energy distribution is for (112) tungstein at 78 K. The work function used was 4.9 eV and the calculated field from the Fowler–Nordheim plot was 0.38 V/Å. The solid curve is the calculated free-electron energy distribution j_0' for these parameters. The energy scale is obtained from an analog to digital conversion of the actual sweep voltage. Finally the enhancement factor R obtained from $j'(\epsilon)$ and $j_0'(\epsilon)$ is shown. For comparison of this technique with the best curves previously published we refer the reader to the total energy distributions for (112) tungstein published by Swanson and Crouser (SwCr66, 67), Plummer and Young (PY70), and Lea and Gomer (LeGo71). The latter two recognized that the field emission characteristics of the (112) plane of

[1] L. W. Swanson and R. W. Strayer have measured the absolute work function by using the so-called Holscher technique. For adsorption studies the work function change was measured from the slope of the Fowler–Nordheim plot.

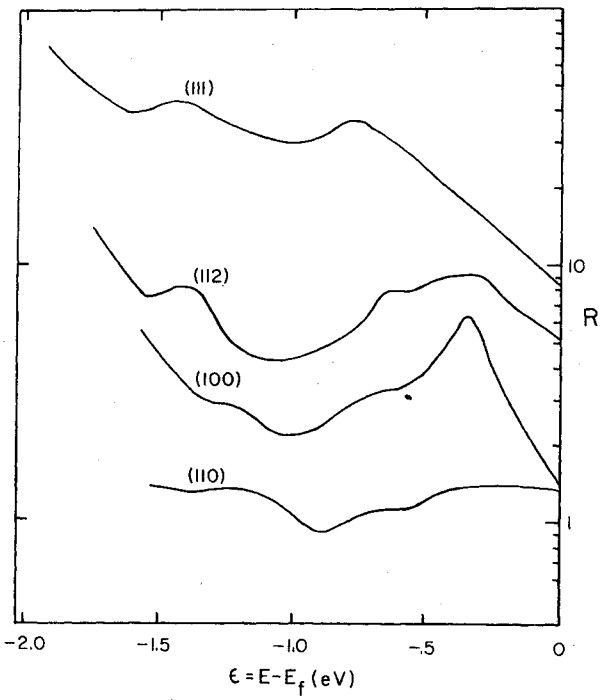

FIG. 16. The enhancement factor curves $R(\epsilon)$ for the four low index planes of tungsten. The free-electron energy distribution $j_0'(\epsilon)$ was calculated using the following work functions $\varphi(110) = 5.25$ eV, $\varphi(100) = 4.64$ eV, $\varphi(112) = 4.90$ eV, and $\varphi(111) = 4.45$ eV.

W could not be explained in terms of free-electron models. More clean surface enhancement factors will be shown in Sec. 4 and the application of this technique to adsorption systems will be illustrated in Sec. 5.

4. CLEAN SURFACE STUDIES

Having devoted a major portion of this article to the foundations for FEED studies, explicit studies and results can now be discussed. This chapter will be devoted to fundamental problems on ostensibly clean single-crystal surfaces. By this restriction, we put aside, until Sec. 5, any chemisorption work. Section 4.1 is a brief discussion of the characteristics of the measured energy distributions from single-crystal planes. The possibility of determining absolute work functions using the total energy distribution and Fowler–Nordheim plot will be discussed in detail. Both the complications and added richnesses of information due to band structure and surface state effects are presented in Secs. 4.1b and c. A brief exposition of thermal field emission from clean surfaces is given in Sec. 4.2. Field emission as a tool for the study of many-body effects in solids is discussed in Sec. 4.3 where both experimental and theoretical advances have been especially interesting.

4.1. Single Plane Total Energy Distributions

In this section we will present characteristic energy distributions from several single-crystal planes, primarily from tungsten. These curves will be compared to one-electron theoretical models for field emission; first with respect to the free-electron model outlined in Sec. 2 and then with respect to simple band structure and surface state models.

For a given single-crystal face of work function φ_e we can measure both the energy distribution $j'(\epsilon)$ as a function of energy at a fixed field and the total current J_0 as a function of field. Therefore, in principle, we can conduct a detailed comparison between experiment and the free-electron model. The area sampled by the probe hole could be determined by observing the field ion image, where the radius of curvature can be calculated by counting step edges (M60). In the free-electron model, the field F at a given voltage V can be determined from the slope of the Fowler–Nordheim plot S_{FN} [Eq. (2.19)]

$$S_{FN} \equiv \frac{\partial \ln J_0/V^2}{\partial V^{-1}} = \frac{4}{3e}\left(\frac{2m}{\hbar^2}\right)^{1/2} s\left(\frac{(e^3F)^{1/2}}{\varphi_e}\right)\frac{\varphi_e^{3/2}}{\beta}, \quad (4.1)$$

where

$$F = \beta V$$

and β is unknown but assumed constant. If the collection efficiency were known and $j'(\epsilon)$ corrected appropriately we could calculate the free electron energy distribution $j_0'(\epsilon)$ and compare it to $j'(\epsilon)$. The enhancement factor $R(\epsilon)$ described in Sec. 3.3 [Eq. (3.16)] is

$$R(\epsilon) = j'(\epsilon)/j_0'(\epsilon).$$

If $j'(\epsilon)$ were a free-electron-like energy distribution $R(\epsilon) = 1$. At the present time we have not completed the program outlined above. The area sampled and the collection efficiency have never been simultaneously measured. Nevertheless we have shown and will demonstrate later that the collection efficiency and obviously the area are not energy-dependent. Therefore we can check the free-electron model up to some constant scaling factor, as described in the previous section. By plotting $\log R(\epsilon)$ we can avoid the effects of this unknown constant on the structure in the $R(\epsilon)$ curves. If the $\log R(\epsilon)$ curve is a constant then the energy dependency of the energy distribution is free-electron like.

In Fig. 16 we have plotted the $R(\epsilon)$ curves for the four low index planes of a tungsten crystal. The work functions used for calculating $j_0'(\epsilon)$ were $\varphi_e(110) = 5.25$ eV, $\varphi_e(112) = 4.90$ eV, $\varphi_e(100) = 4.64$ eV, and $\varphi_e(111) = 4.45$ eV and a band depth of eight volts was used ($E_f = 8$ eV). These curves are very reproducible when the surfaces are clean and annealed. In fact the energy distribution from any of these planes is so characteristic that the crystallographic plane being sampled could easily be identified by observing the measured energy distribution. Only the (110), (100), and (112) planes develop on a thermally annealed field emitter (M56), while the (111) plane just denotes a direction on the emitter since the plane does not develop. It is obvious

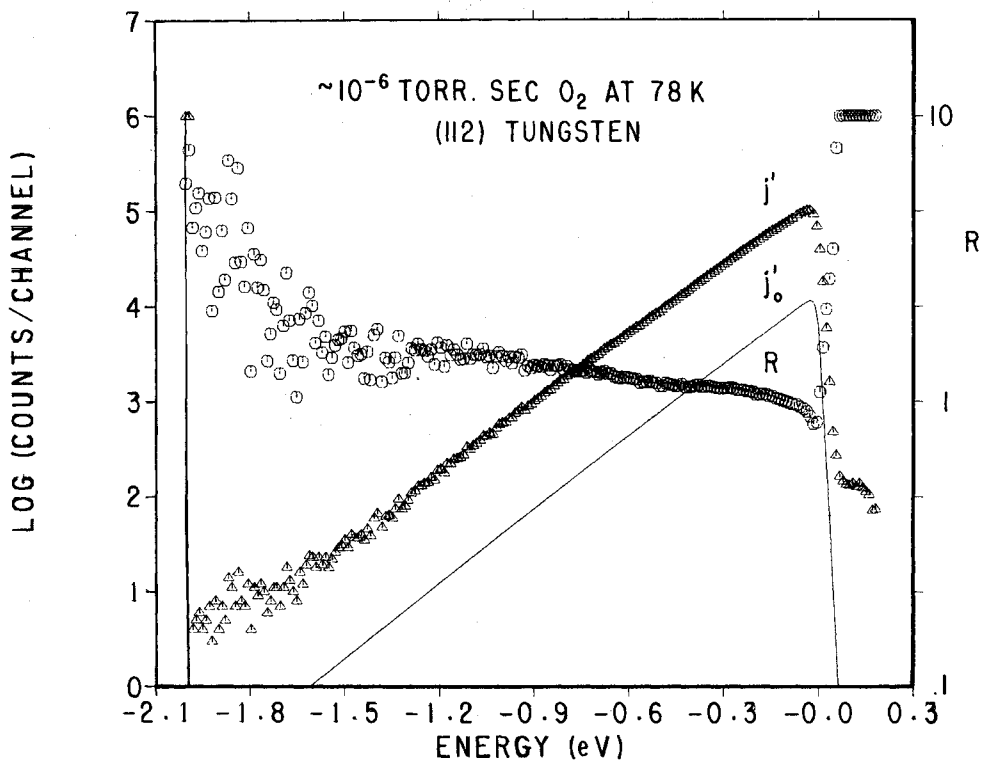

FIG. 17. Measured energy distribution $j'(\epsilon)$, calculated free-electron energy distribution $j_0'(\epsilon)$ [$\varphi=6.14$ eV], and enhancement factor $R(\epsilon)$ for 3×10^{-7} Torr·sec oxygen exposure on the (112) plane at 78 K.

from these curves that the energy distributions from tungsten are not free-electron like, at least when viewed in this manner. It is tempting to immediately interpret the structure in the $R(\epsilon)$ curves in terms of the electronic properties of the substrate but there are other explanations which must also be considered.

Structure induced by the analyzer can generally be ruled out because of the differences in the four curves, coupled with the fact that changing the optics in the analyzer (Fig. 14) results in changes in the resolution but not in the structure. Yet the collection efficiency of the analyzer could be a slowly varying function of energy creating a gradual slope to the log $R(\epsilon)$ curve. One example will be given to illustrate that this is not a major factor with the analyzer shown in Fig. 14. When the (112) plane of tungsten is exposed to oxygen at 78 K there is most likely a disordered oxygen layer and the total energy distribution exhibits no energy levels within the energy range scanned. Figure 17 shows the measured energy distribution $j'(\epsilon)$, the calculated free-electron energy distribution $j_0'(\epsilon)$, and the enhancement factor R for 3×10^{-7} Torr·sec oxygen exposure on (112) tungsten at 78 K. The work function change was obtained from the change in the slope of the Fowler–Nordheim plot and the clean work function was chosen as 4.9 eV. The clean (112) plane with $\varphi_c=4.9$ eV is shown in Figs. 15 and 16. The $R(\epsilon)$ curve in Fig. 17 has no structure and is nearly constant, indicating that when there are no relatively narrow energy levels near the Fermi level the free-electron energy distribution j_0' matches the energy dependence of the measured energy distribution j', i.e., the collection efficiency is constant over this range.

Another source of curvature in the $R(\epsilon)$ plots would arise from deviations of the surface potential barrier from the assumed image potential plus applied field. The potential near the surface surely deviates from a strict image potential and the applied field can polarize the surface, changing the work function (S70). The effect of these changes can be investigated by using different model potentials in the numerically calculated $j_0(\epsilon)$ curves. Any likely change in the work function or surface potential does not perturb the log $R(\epsilon)$ curve significantly. The gradual slope of the $R(\epsilon)$ curve in Fig. 17 could result from such effects or possibly because our estimate of the work function of the clean substrate is incorrect.

A potential source of error in calculating $j_0'(\epsilon)$ is the inadequacy of a one-dimensional tunneling model. The field is radially symmetric, not planar, which introduces slight energy dependence differences in $R(\epsilon)$ as shown by Politzer and Feuchtwang (PFe71). Also the tangential component of the field (Fig. 9) and its variation with position on the emitter caused by a nonspherical surface could introduce error. This can easily be demonstrated by looking at the total current emitted from

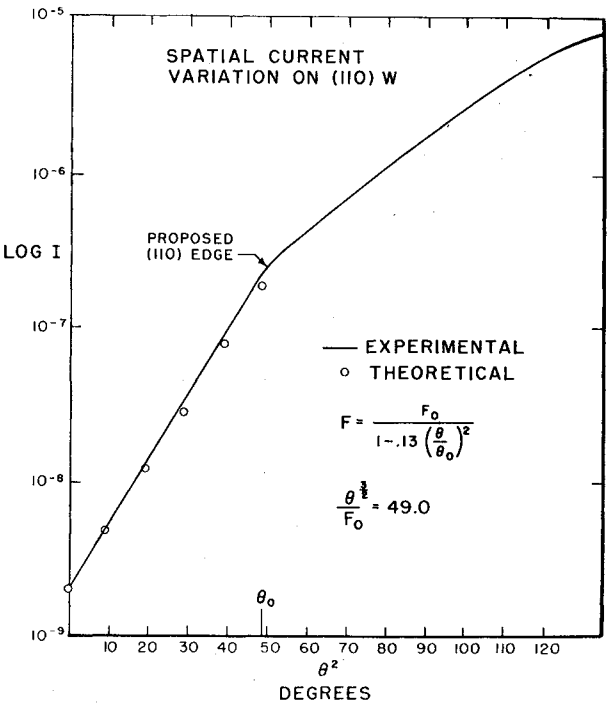

FIG. 18. Plot of the measured total current I as a function of the square of the angle θ from the center of the (110) plane on a thermally annealed emitter. The knee in the curve indicates the plane edge. The open circles are the calculated current for a field variation $F=F_0/[1-0.13(\theta/\theta_0)^2$ over the plane. F_0 is the field in the center of the plane.

different regions of a large crystal plane such as the (110) plane of tungsten. Figure 18 shows the measured total current as a function of θ^2, where θ is the angle from the center of the (110) plane. We have observed that the edge of the plane can be determined by the knee in this curve. Since the work function should be a constant for any region of the (110) plane, except very near the edge, the current change is due to changes in the field. This field change is a result of the flat plane on a hemispherical emitter. The field is lower in the center of the plane. The circles in Fig. 18 are the calculated current using the field variation over the (110) plane determined by Plummer and Rhodin from a consideration that there is a component of the field tangential to the surface (PRh68).

The point is that the tunneling is really not one-dimensional. How to treat this problem theoretically is not at all clear. Even if it is legitimate to treat the tunneling as one dimensional there will be effects due to the electron trajectories, as shown by the calculation in Sec. 3.1. If the probe hole is in the center of the plane, then at lower energies there will be more electrons with large transverse energy entering the probe hole than predicted by the calculation in Sec. 3.1. This effect can be calculated and is usually small. All of the aforementioned problems can induce gradual changes in $R(\epsilon)$ but seem unlikely to produce sharp structure. With these precautions in mind let us attempt a tentative interpretation of these enhancement curves.

4.1a. Work Function

In Secs. 2.3 and 3.3 we described the Fowler–Nordheim plot. To reiterate—it is a plot of the log of the measured total current I divided by the square of the applied voltage V as a function of the reciprocal voltage. The slope of the Fowler–Nordheim plot S_{FN} is given by Eq. (4.1). If the current I (hkl) is measured from a single-crystal plane (M55), then $S_{FN}(hkl) \propto \phi_e^{3/2}(hkl)/\beta(hkl)$, where $\beta(hkl)$ relates the applied voltage to the field on the given crystal plane and the indices (hkl) are the Miller indices of the plane in question. It is impossible to measure the work function from the slope of the Fowler–Nordheim plot unless assumptions are made about β or an additional independent measurement is made. The usual procedure is to assume that the field is uniform over the emitter surface so that β is independent of crystallographic direction. Then the total current from the whole emitter can be measured, an average work function assumed, and ratios of Fowler–Nordheim plots utilized to calculate $\phi_e(hkl)$. In fact there is no reason to expect that the field is uniform across the emitter surface and Fig. 18 has already been introduced to illustrate the field variation over a single-crystal plane. A dramatic illustration of how bad this assumption really is was furnished by Todd and Rhodin (ToRh72) who used this assumption to measure the work functions of the (110) plane for thermally annealed and field-evaporated tungsten emitters. The measured work functions were 5.9 and 5.4 eV, respectively. Obviously the work function of the (110) plane is not changing: the end form of the emitter is the change causing a variation in the β factor.

Young and Muller (YMu62) fully realized this problem and attempted to derive an independent measurement so that the field and the work function could be simultaneously measured. One of their proposed techniques, which is relevant to this paper, utilized the characteristics of the total energy distribution. Young and Clark (YC66a) elaborated upon this procedure, proving that if the total energy distribution and the Fowler–Nordheim plot could be described by a free-electron model, then absolute work functions could be calculated from slopes of the Fowler–Nordheim plot and the energy distribution [Eq. (2.20)]. Before this technique can be utilized it must be shown experimentally and theoretically that both the Fowler–Nordheim plot and the total energy distribution can be represented by a free-electron model.

The validity of the free-electron calculation of the Fowler–Nordheim plot has been demonstrated by Duke and Fauchier (DuFa72) for a model characterized by a one-dimensional Kronig–Penney potential in a three-dimensional electron gas. This validity is only true

when the Fermi surface is intersected by a reciprocal lattice vector in the direction being studied (I66, I67). In general whenever the total energy distribution peaks at the Fermi energy the slope of the Fowler–Nordheim plot can be described by a free-electron model. It is easy to understand this statement when one realizes that the Fowler–Nordheim plot is simply the rate of change of current at the Fermi energy with respect to the applied field.

On the other hand, we have already demonstrated experimentally in Fig. 16 that the total energy distributions are not necessarily free-electron like. If the total energy distributions were free-electron like, the $R(\epsilon)$ curves in Fig. 16 would have no structure. We could have erred in our choice of work function to calculate the free-electron energy distribution $j_0'(\epsilon)$. This would cause $R(\epsilon)$ to be nonconstant, but it is easy to demonstrate from our definition of $R(\epsilon)$ [Eq. (3.16)] and the Young and Clark (YC66a) equation [Eq. (2.20)] that

$$\partial \log R(\epsilon)/\partial\epsilon = \tfrac{3}{2}[\phi_0^{-1} - \phi_e^{-1}] \times (S_{FN}/V)[t(y)/s(y)], \quad (4.2)$$

where ϕ_0 is the work function used to calculate $j_0'(\epsilon)$ and ϕ_e is the actual work function assuming we have made an error in our original choice of ϕ_0. Equation (4.2) when applied to the data for (112) tungsten in Fig. 15 would predict a work function ϕ_e ranging from 5.3 to 4.5 eV depending upon the energy at which $\partial \log R(\epsilon)/\partial\epsilon$ was evaluated.

It should be clear by now that the total energy distribution from a nonfree-electron-like material is not adequately described by a free-electron model. Therefore, in general work functions cannot be obtained from the combination of the Fowler–Nordheim plot and the energy distribution, unless the effects of the electronic properties of the solid on the energy distribution are adequately described; this subject will be considered in the next sections. Furthermore, between field emission work function measurements and those on macroscopic crystals there exists no discrepancy which at the present time cannot be rationalized by a field variation over the emitter surface.

4.2. Band Structure

4.2a. Band Structure: Experimental

Field emission energy distributions can be helpful in the study of band structure effects even though field emission probes only states within ~1–2 eV of the Fermi level, because experimental band structure measurements using other techniques also suffer limitations. Any information obtained by field emission could serve as a check on the major techniques such as photoemission or soft x-ray emission. The theoretical problem in analyzing field emission energy distributions is to determine how the number of electrons tunneling with total energy E is related to the one-electron states in the solid or at the surface of the solid.

In Sec. 2 we discussed the necessity of artificially reducing the three-dimensional problem to one dimension in order to make the mathematical problem tractable. When this assumption has been made, the number of electrons tunneling with energy E is a two-dimensional integral of tunneling probability in the transverse k plane. The integration is over all values of transverse k falling within the shadow of the energy surface E on the transverse plane. Unfortunately, the tunneling probability will in general not be simply a function of normal energy. The complications of calculating this function were outlined in Sec. 2 and will be discussed further in this chapter. Not only will the tunneling probability depend upon the energy and k vector of the initial state in the solid but also upon its degree of localization at the surface. The discussion thus far still skirts the major issue; that is, what are the initial states at the solid surface from which the electrons tunnel and how are these states related to the bulk states.

The importance of the state of the surface relative to that of the bulk should have been dramatically illustrated in the total energy distribution shown in Fig. 17, which shows that a single monolayer of oxygen adsorbed at 78 K removes all the structure in the energy distribution (Fig. 15) which we might have prematurely interpreted as due to bulk electronic properties. The bulk band structure is calculated by solving the Schrödinger equation for a model potential utilizing periodic boundary conditions. But if different boundary conditions are invoked such as a real surface, some of the solutions to the Schrödinger equation rejected in the bulk may be resurrected to a physically meaningful role. Therefore it should be apparent that we should calculate in detail the wave functions at the surface and their relationship to the bulk states and to the measured energy distribution. An initial attempt at such a calculation was made for "Cambridge Surface States" (Ga72). This will be discussed in the next section.

Now let us consider an experimental method of separating the very surface sensitive electronic properties from the less surface sensitive ones which are probably more closely related to the bulk. The presence of a weakly bound adsorbate such as a noble gas has been shown to remove surface sensitive structure from the energy distribution (PlGa70, LeGo71). Since these gases do not form strong chemical bonds their effect should be only a change in the boundary condition at the surface. For example, the effect of Xe adsorption on the energy distribution from (100) tungsten is to remove the fine structure at $\epsilon = -0.35$ eV and -1.4 eV, while the broad structure at $\epsilon \sim -0.65$ eV still remains. This technique reveals which pieces of structure in an energy distribution are extremely sensitive to the surface conditions but it should not be concluded that the remaining structure necessarily reflects the bulk band structure.

There are a few existing examples of measured energy

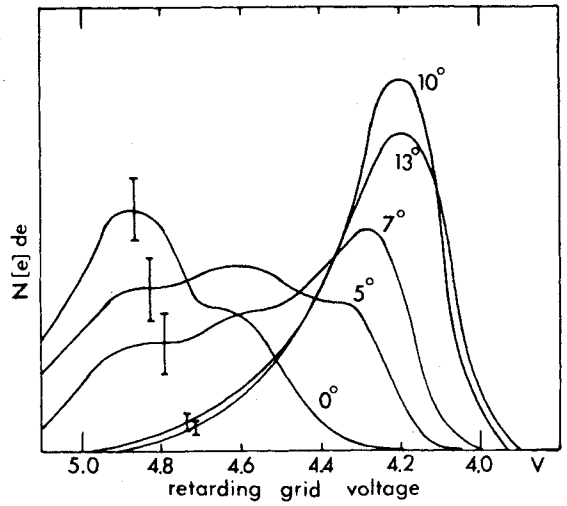

FIG. 19. Total energy distribution of electrons emitted from a copper (111) plane. The projection of the probe hole at the tip was 30 Å in diameter. The position of the probe hole is defined by the apparent crystallographic angle away from the ⟨111⟩ pole. (WbBl69.)

distributions which reveal the potential of this technique for band structure analysis. The observation of a band edge should be relatively easy to interpret. We have already discussed (in Sec. 2) the effect expected from the neck in the ⟨111⟩ direction of copper. Whitcutt and Blott (WhBl69) grew copper crystals on the (110) region of a tungsten field emitter. The energy distributions as a function of angle from the ⟨111⟩ pole are shown in Fig. 19. Indeed their energy distribution at 0° does not start at the Fermi energy because there are no electrons within the metal which have normal energy equal to the Fermi energy, i.e., there is a neck in the ⟨111⟩ direction. Whitcutt and Blott observed that this behavior seemed to be sensitive to the size of the dark ⟨111⟩ region. The energy distributions shown in Fig. 19 were taken when the central ⟨111⟩ region of the Cu field emission pattern was about 1000 Å in diameter. When the size is reduced to about 300 Å the energy distributions always peak at the Fermi energy. This work raises several very fundamental questions and suggests some interesting experiments. Is there a critical size of a single plane on a field emitter before the energy distribution reflects the bulk? In other words, are edge effects important? What would happen to the energy distributions shown in Fig. 19 if the surface was contaminated or disordered? Would the energy distribution peak at the Fermi energy under these conditions? Are there surface states in this gap? How thick does the copper layer have to be before the gap appears? Hopefully, in the near future many of these questions will be answered.

Another potential application of field emission energy distributions to band structure is the ability to vary the normal direction continuously. In the drawing of Fig. 9 we can vary $\hat{n}_0$ continuously from one region to another.

Figure 20 shows the enhancement factors (Sec. 3) R for tungsten for seven different directions along the [1$\bar{1}$0] zone. The angles are measured from the ⟨001⟩ direction. The peak at $\epsilon = -0.37$ eV in the (100) plane curve (SwCr66, 67) is believed to be a surface state (PlGa70), created by a spin–orbit split band gap in tungsten (Lo65) (see Sec. 4.2b). As the normal direction is moved away from the ⟨100⟩ direction this state decreases in amplitude and moves toward the Fermi energy. These two effects are related to changes in the gap with direction. It must close and move above the Fermi energy within 10° of the ⟨100⟩ direction (Ma65). Another feature is the angular sensitivity of the (111) energy distribution. Since the (111) is not a well defined plane on a field emitter we do not expect any effects from the surface two-dimensional order, but moving about 5° in any direction from (111) changes the shape of the energy distribution. This indicates that there is more structure in the energy surfaces in the ⟨111⟩ direction than indicated by Mattheiss's calculations (Ma65). These two examples indicate both the potential and the limitation of field emission energy distribution as a bulk band structure probe.

4.2b. Band Structure: Theoretical

Throughout this review, we have alluded to many of the various theoretical ideas put forth which might

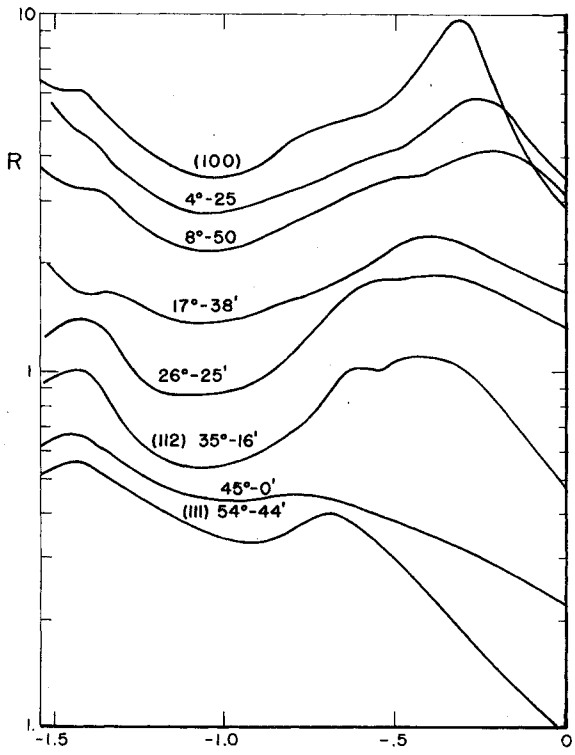

FIG. 20. The enhancement factor curves $R(\epsilon)$ for several directions along the [110] zone between the (100) plane and the (111) plane.

account for band structure effects in field emission tunneling. In this section we shall set up the ideas in a systematic manner. Basically, band structure can enter into a TED through both the supply function and the tunneling probability of Eq. (2.1).

Itskovich was responsible for the first detailed model treatment of band structure effects in field emission (J66, I67). The starting point is an expression for the total current

$$j=e\sum_{\mathbf{k}} n(\mathbf{k})D(\mathbf{k}) \tag{4.3}$$

which is equivalent to Eq. (2.1). Here $n(\mathbf{k})$ is the arrival rate of electrons and $D(\mathbf{k})$ is the barrier penetration probability of electrons in quantum state $\mathbf{k}$. The sum is over all such states. As most recently pointed out in the monumental work of Politzer and Cutler (PC70, 72, P72), band structure effects enter Eq. (4.3) in three distinctly different ways:

(1) $n(\mathbf{k})$ must be calculated from the quantum mechanical current $j(\mathbf{r})=(\hbar/2mi)(\psi^*(\mathbf{r})\nabla\psi(\mathbf{r})-\text{c.c})$, using linear combinations of actual Bloch functions of the solid;

(2) $D(\mathbf{k})$, which is three-dimensional, must be calculated from the actual wave functions rather than plane waves;

(3) The sum on $\mathbf{k}$ must be converted to a surface integral over the true surfaces of constant energy in the Brillouin zone rather than over free-electron spheres.

As discussed in Sec. 2, Stratton (S64) developed a simple integral relation, Eq. (2.4), for treating energy surface topology effects.

Itskovich carried out part of the above-mentioned procedure, with some technical approximations, for an s-band material with a periodic potential. He then considered some special energy surfaces. Although he did not treat the energy surfaces associated with a particular metal, he arrived at the conclusion that band structure can influence both the FN and TED. Specifically, the presence of hole surfaces slightly below the Fermi energy will result in maximum current coming from states lower in energy than might be expected from a free-electron model. Interpreting such results in terms of a free-electron model could lead to erroneous assignments of work function. Furthermore, emission from the hole surfaces could result in additional "anomalous" structure in an energy distribution.

Nagy and Cutler (NaC69) applied the Stratton procedure to model energy surfaces of W. As pointed out by Gadzuk (Ga69a), tunneling from d bands is hindered relative to s-band tunneling, a fact which is accounted for in item (2) above. Since the W energy surfaces near the Fermi level are composed of s and d bands, it seems likely that the Stratton procedure as carried out by Nagy and Cutler could yield misleading results since the tunneling probability variation is not considered.

Obermair (Ob68) developed a theory for spin-polarized electron beam production by field emission from ferromagnets. He outlined the procedure for calculating the band structure tunneling probability. By assuming that the surface potential varies only in the z direction, whereas the periodic potential of the metal is three-dimensional, $D(\mathbf{k})$ is obtained as follows: Inside the metal, the wave functions $\psi_{\text{in}}(\mathbf{r})$ are linear combinations of Bloch functions

$$\psi_{\text{in}}(\mathbf{r})=\psi_{n\mathbf{k}}(\mathbf{r})+\sum_{n'\mathbf{k}'} A(n',\mathbf{k}')\psi_{n'\mathbf{k}'}(\mathbf{r}), \tag{4.4}$$

and in the field region outside the metal the wave functions are

$$\psi_{\text{out}}(\mathbf{r})=\sum_{\mathbf{G}_{||}} C(\mathbf{G}_{||})\exp\left[i(\mathbf{k}_{||}+\mathbf{G}_{||})\cdot\boldsymbol{\varrho}\right]f_{\mathbf{G}_{||}}(z), \tag{4.5}$$

with n the band index, $\mathbf{G}_{||}$ a reciprocal lattice vector in the transverse plane, $f(z)$ an outgoing solution to the relevant one-dimensional Schrödinger equation with the potential $V=V_{\text{surf}}(z)-eFz$, and V_{surf} the particular surface potential chosen. The coefficients $A(n',\mathbf{k}')$ and $C(\mathbf{G}_{||})$ are determined by matching ψ and $d\psi/dz$ at the surface. It is important to note that the results are critically dependent upon the location of the matching plane. Three starting choices suggest themselves; at the last layer of ion cores, half an inner planer separation away, and a full planer separation away. With this latitude in choices, the calculated tunneling probabilities can vary over several orders of magnitude, all other things being equal. It is generally assumed that half an inner planer separation is the most reasonable choice. With this assumption the matching relates the coefficients, from which a transmission function can be readily calculated as in Sec. 2. Obermair carried this out, to a limited extent, for Cu but did not find the dramatic effects hoped for. This is due to the fact that d-band effects occur far beneath the Fermi level relative to the $\sim$0.5-eV depth within which most field emission current originates. More positive results were obtained for magnetic effects from $Eu_{1-x}Gd_xS$.

Probably the most extensive and realistic field emission calculation is that of Politzer and Cutler (P72, PC72). Their study was partially motivated by total current measurements such as those of Gleich, Regenfus and Sizman (GlReSi71) who observed a spin polarization $P=(J_\uparrow-J_\downarrow)/(J_\uparrow+J_\downarrow)$ of about -10% in field emission from ferromagnetic Ni where $J_{\uparrow(\downarrow)}$ is the total current of electrons with majority (minority) spin. In the theory of Politzer and Cutler, all three steps in the band structure procedure were carried out. Politzer and Cutler realized that the band structure of $3d$ metals can be considered as the superposition of unhybridized $4s$ and $3d$ bands. Hybridization or spin–orbit splittings create gaps which could result in surface states as will be discussed in the next section. Electron emission is then considered as the sum of emission from the independent bands. The Ni $4s$–p

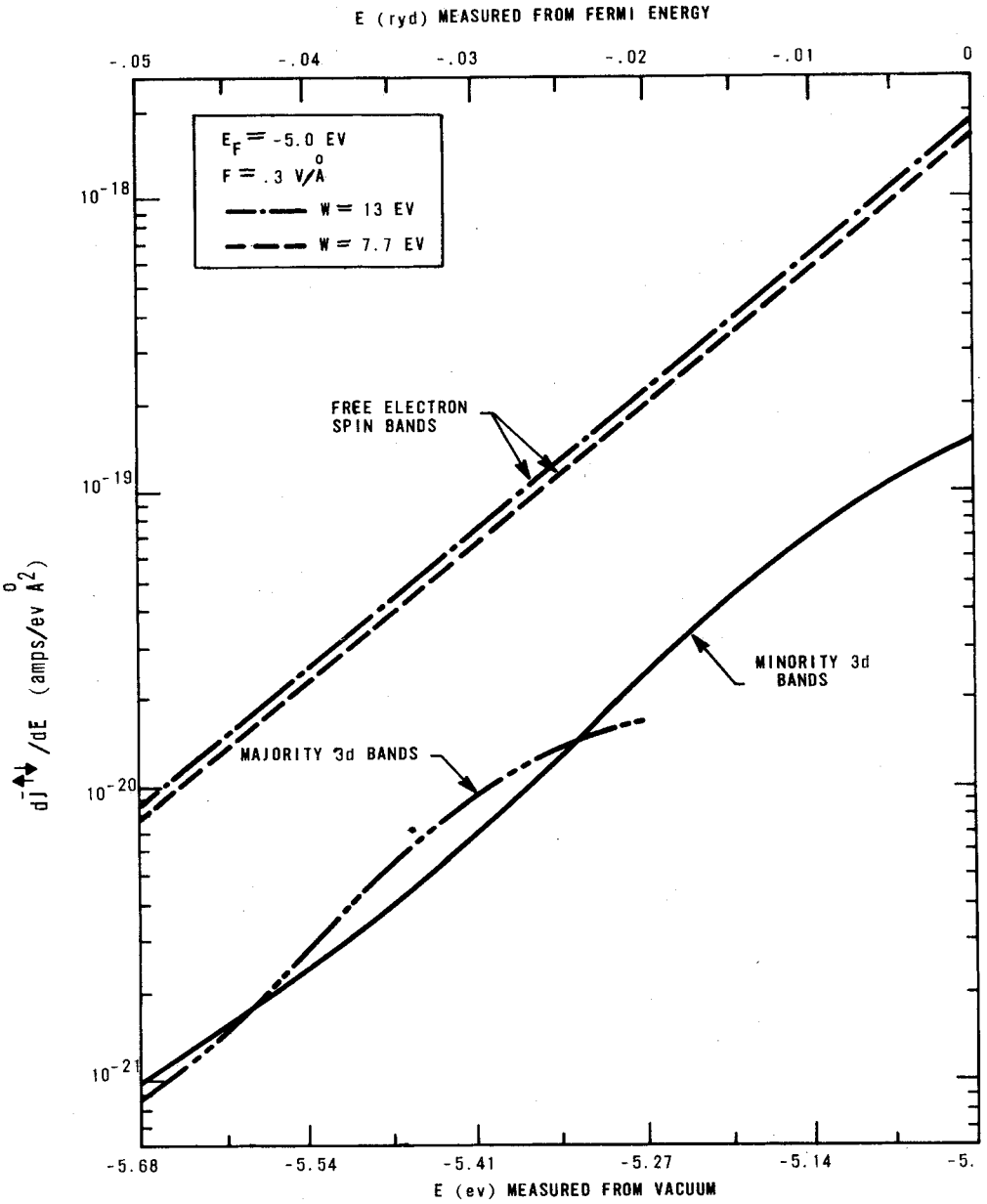

FIG. 21. Energy distribution for field-emitted electrons around the [100] axis of ferromagnetic Ni. The 3*d* distributions are compared with a free-electron-like 4*s*-*p* band with bottom at Γ_0 (13 eV below vacuum). There are no majority-spin bands above $E \simeq -0.02$ Ry (top scale). The structure in the 3*d* distributions results from the complicated topalogy of the constant energy surfaces. (PoC72.)

bands are approximated by free-electron bands. The 3*d* bands of majority and minority spin are separated by the exchange energy $\simeq$0.03 Ry. These bands are described by a tight binding calculation of Fletcher (Fl51) but modified by Politzer and Cutler to agree with the minority spin bands of Connolly (Co67). Bloch waves are formed from this model and used in Eq. (4.4). The surface potential without applied field is taken to be a step barrier so that the functions $f(z)$ in Eq. (4.5) are just the Airy functions of the triangle barrier discussed in Sec. 2. Transmission and supply functions are calculated with these wave functions. The sum on $\mathbf{k}$ is replaced by a surface integral as discussed after Eq. (2.2). Politzer and Cutler then calculate the actual energy bands, from which $\nabla_k E(\mathbf{k})$ is obtained, and the surface integration is performed over the true Ni energy surfaces. The principle energy distribution results are shown in Fig. 21. The dash–dot curve is the *s*-band emission. The minority spin-band emission (solid curve) and the majority spin emission (dash–

dot–dot curve) are down an order of magnitude. This follows from the fact that the shape of the ↑ and ↓ spin bands are quite similar but the ↑ spin band lies lower in energy. Since field emission exponentially prefers emission near the Fermi level, the polarization obtained in the total current by integrating the energy distribution is

$$P \simeq (J_{3d\uparrow} - J_{3d\downarrow})/(2J_{4s} + J_{3d\uparrow} + J_{3d\downarrow}) = -4\%$$

under the good assumption of unpolarized s bands. This is in good agreement with the experimental results of Gleich *et al.* (GlReSi71) and strengthens the evidence in support of the Stoner–Wolfart–Slater itinerant band model of ferromagnetism. It is a particularly important result in view of recent spin polarization photoemission experiments (BaBuCaSi70, BuCaSi71) in which positive polarizations were observed. In view of the conflicting experimental results and the importance of the results in terms of magnetism theory, considerable controversy has been generated over the validity of the field emission results (Siegmann, personal communication). Although this is a problem to be resolved in the future, it does not reflect upon the Politzer–Cutler calculation directly. They have calculated the correct consequences of an assumed band structure. It may be that the assumed band structure is wrong but this does not detract from their theory.

It is encouraging to see the results of thorough calculations confirming both experimental data and intuitive expectation of d-band tunneling. Previous feeling was that d-band tunneling was strongly discriminated against compared to s–p bands and that this was the reason that free-electron theories were so successful in explaining the gross features of field emission. This presumption now seems to have a firm basis.

The independent band picture has been used to explain some of the surface insensitive structure in the experimental enhancement curves such as Fig. 22. Figure 22 shows an enhancement curve for (100) W together with a relativistic energy band structure calculated by Loucks (Lo65). It is believed (PlGa70) that the structure in R centered at $\epsilon \sim -0.78$ eV arises from d-band emission from the high density of states states in which -1.0 eV $\lesssim \epsilon \lesssim -0.4$ eV and $k \lesssim 0.6\ \Gamma H$. The remaining structure, the so-called Swanson hump, is emission from surface states which exist in the gap at $k \simeq 0.3\ \Gamma H$. Although the amount of band structure information obtained from such measurements is not overwhelming, it is indeed possible to see some things such as band edges and high density of states regions in nonmagnetic metals.

Recently Duke and Fauchier (DuF72) have carried out exact model calculations on a Kronig–Penney solid in order to gain some understanding of possible band structure effects in field emission. The model they adopted is the following: The potential of the solid is taken to be delta function sheets spaced periodically in the z direction. Thus the three-dimensional solid has potential variations in only the z direction. The surface barrier is a square barrier modified by the applied field, thus resulting in the familiar triangle tunneling barrier. The field emission properties of this model can be calculated exactly using the wave-matching technique. In their study of clean surface properties, Duke and Fauchier systematically vary the parameters of the model such as the potential strength, bandwidth, and Fermi energy in order to investigate possible alterations to both the FN and TED.

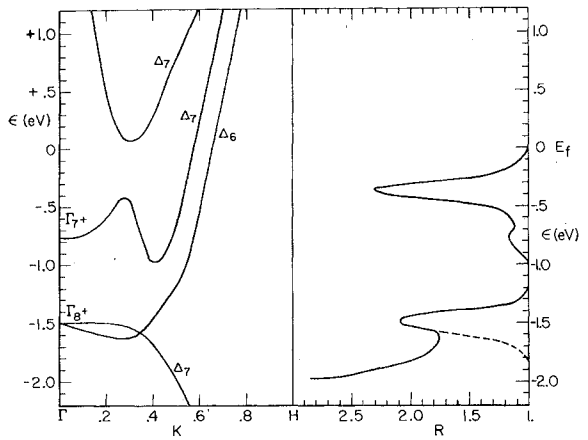

FIG. 22. (a) Relativistic energy bands for the (100) direction of tungsten calculated by Loucks showing the two gaps created by the splitting of the three Δ_7 bands. (b) An experimental enhancement factor for the (100) plane of tungsten. (PlGa70.)

The observations of Duke and Fauchier pertinent to the slope of the Fowler–Nordheim plot S_{FN} were: (1) S_{FN} is independent of the lattice potential to within about 3%; (2) S_{FN} is independent of F for 0.2 V/A$< F <$0.6 V/A; and (3) The calculated S_{FN} deviated only slightly from the Fowler–Nordheim value [Eq. (4.1)]. Therefore they concluded that the dependence of the total current on the field is dominated by the exponential factor in the transmission coefficient. Thus, if the Fermi energy does not lie in a gap, the measured slope of the Fowler–Nordheim plot can be used to extract the field if the work function is known (Sec. 2).

In contrast to the independence of the current on the lattice potential they found that the energy distribution was sensitive to band structure. Specifically they conclude "...in the case of clean surfaces we find that reasonable models of the lattice potential can, in the cases of Fermi energies near a critical point in the energy band or of narrow bands, cause a substantial change in the current and energy distributions relative to the free-electron model." They use their model to illustrate theoretically the conclusion we have drawn experimentally in Sec. 4.2; that band structure effects in the energy distribution will induce errors in a determination of the work function made by combining the slopes of Fowler–Nordheim plot and the energy distribution.

Next Duke and Fauchier examine various modeling

procedures used to obtain transmission functions, namely the free-electron, effective mass, and tight-binding approximations. Aside from pathological discrepancies, all approximations yield results roughly similar to the "empirical" tight-binding approximation which is somewhat more adequate over a wider range of energies. They conclude with "the ratio of tight-binding to free-electron contributions to the energy distributions is of order 0.5–1.0, not 10^{-1}–10^{-2} as claimed by some authors (Ga69a, PoC70)." This is a misinterpretation of the claims by Gadzuk and by Politzer and Cutler. What these authors claimed is that such a ratio exists between a tight-binding band (whose width is roughly 10% of the free-electron band) and the free-electron band. In fact Duke and Fauchier compare tight-binding and free-electron approximations of bands of the same width and even in this case find mild tunneling suppression in the tight-binding bands.

Further discussion of this work will be given in the next section on surface states and in the chapter on adsorption.

4.2c. Surface States

Field emission energy distributions offer an ideally suited technique for the study of surface states, either intrinsic or extrinsic. The structure in the energy distribution has already been shown to reflect only the electronic properties of the surface charge density (see Figs. 15–17). Therefore if samples of the desired material can be prepared, the existence of a surface state on any given plane can easily be confirmed or denied. We will discuss only intrinsic surface states in this section for both metals and semiconductors.

The structure at $\epsilon = -0.37$ eV in the energy distribution from the (100) plane of tungsten (Fig. 16) has motivated a large amount of literature in an attempt to explain its source. It is now commonly believed that this structure originates from a surface state in a spin–orbit–split gap in the ⟨100⟩ direction of tungsten, but the historical development of this interpretation is worth pursuing briefly. Swanson and Crouser (SwCr66, 67) first observed this structure in an energy distribution. They realized that there were dramatic band structure effects in the (100) direction of tungsten (Lo65), and as a result, postulated that this peak represented a high density of states at the top of the lower band in the spin–orbit–split gap. This discovery and proposed explanation created a number of theoretical papers attempting to reproduce the measured energy distribution using model band structures (Ga69a, NaC69, PoC70). Experiments by Plummer and Young (PlY70) demonstrated that this peak was sensitive to surface contamination of Ca and CO. They (PlY70) suggested that if the hump in the energy distribution originated from a narrow tight binding d band as postulated by the theoretical papers referred to above, then its disappearance could result from the formation of a strongly covalent bond with the adsorbed species. This bonding would result in molecular energy levels at different energies for the outer tungsten atom compared to the atoms in other layers. The inadequacy of this argument was pointed out by the experiments of Plummer and co-workers (PlGa70, PlB72) and Lea and Gomer (LeGo71) where it was shown that not only partial monolayers of chemisorbates such as CO, H_2, O_2, and N_2 but even noble gases like Kr and Xe removed this structure.

Theoretical predictions of metallic surface states first by Goodwin (Go39) and recently by Stern (St67) and Forstmann, Heine, and Pendry (Fo70, FoHe70, FoPe70, and He70) led Plummer and Gadzuk (PlGa70) to postulate that the observed structure in the (100) tungsten energy distribution was a surface state. Figure 22 displays the R factor (Sec. 3.3) for the (100) plane of tungsten plotted adjacent to the relativistic energy bands for the ⟨100⟩ direction of tungsten calculated by Loucks (Lo65). Plummer and Gadzuk (PlGa70) suggested that the peak at $\epsilon = -0.37$ eV was a surface state in the spin–orbit–split Δ_7 symmetry bands whereas the small peak at $\epsilon \cong -0.8$ eV reflected a bulk high density of states. The low energy structure at $\epsilon = -1.5$ eV was very difficult to observe experimentally (PlGa70). It was originally interpreted as a surface state (PlGa70) in the lower gap, but more recent experiments (PlBe72) make that interpretation questionable. The enhancement curves shown in Fig. 20 illustrate that the surface state is localized within $\sim 8°$ of the ⟨100⟩ direction.

Using the results of Forstmann *et al.*, Gadzuk has constructed a theory of tunneling from such surface states in which the total surface state current is given in terms of parameters obtainable from the bulk band structure, the work function, applied field, and density of surface atoms (Ga72). The end result is that the total current per unit area which is field emitted from surface states of energy ϵ_{ss} is

$$j_{ss}(\epsilon_{ss}) = (2e/\hbar l^2)(\hbar^2 k_r \kappa/2m) D_{Tot}(\epsilon_{ss})$$
$$= 1.85 \times 10^{13} [(k_r \kappa/l^2) B] D_{WKB}(\epsilon_{ss}) \text{ A/cm}^2. \quad (4.6)$$

Here l^2 is the area per surface atom in Å^2, k_r is the magnitude in Å^{-1} of the electron wave number where the gap occurs in the Brillouin zone, $D_{Tot} \equiv B D_{WKB}$, D_{WKB} is the tunneling probability given by Eq. (2.14), and B is the tunneling probability reduction due to the centrifugal barrier discussed in Sec. 2. From surface state theory (Ga72) we have

$$\kappa = m^{-1}(\Delta_k^2 - \epsilon^2 - m^2 k_r^2 + 2mk_r\epsilon)^{1/2}, \quad (4.7)$$

with $m = dE/dk\,|_{k=k_r}$ the slope of the energy band at k_r before hybridizing and Δ_k the width of the gap. κ is a measure of the localization of the surface state within the metal. Typically we have 20 Å $\lesssim 1/\kappa \lesssim$ 100 Å as can be obtained by using true band structure determined values of m, Δ_k, and k_r.

In actual practice, the tunneling current from surface states is spread over a band of energies due to two-

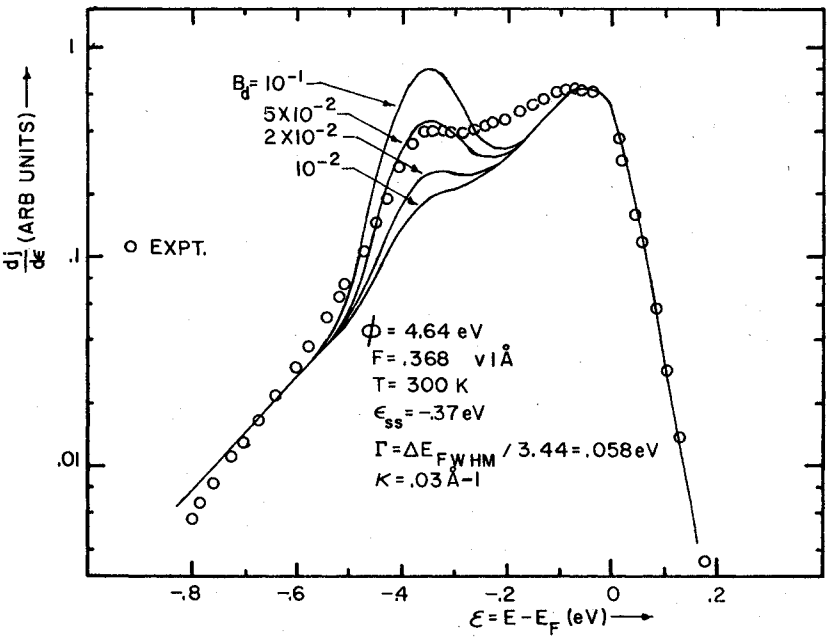

FIG. 23. Experimental (O) and theoretical (—) TED from (100) plane of W at 300 K. (Ga72.)

dimensional bands, finite lifetimes, and scattering into other bands. To allow for these processes, a Gaussian distribution (width Γ) of surface state energies has been taken which preserves the total surface state current, $j_{ss}(\epsilon_{ss}) = \int (dj_{ss}/d\epsilon)\, d\epsilon$. The complete TED is thus considered to be $j_{Tot}' = j' + j_{ss}'$ with j' given by Eq. (2.18) and

$$j_{ss}' = \frac{j_{ss}(\epsilon)}{(2\pi)^{1/2}\Gamma} \exp\left[-\frac{1}{2}\left(\frac{\epsilon-\epsilon_{ss}}{\Gamma}\right)^2 - \frac{1}{2}\frac{\Gamma^2}{d^2}\right]. \quad (4.8)$$

Combining Eqs. (2.18) and (4.6)–(4.8), and using the parameters characterizing the experimental system of (100) W, we find the theoretical and experimental results shown in Fig. 23 for various choices of B within the range $10^{-3} < B < 1.5\times10^{-1}$ suggested by Politzer and Cutler (PoC70). The integrated current under the surface state hump is in quite good accord with the theoretical calculations; this adds support to the surface state interpretation.

This calculation by Gadzuk (Ga72) illustrates the characteristics of a surface state. It has a given charge density per atom and a characteristic penetration depth $1/\kappa$ into the bulk. To remove any doubt about the $\epsilon = -0.37$-eV peak being a surface state, the decay of the charge density into the bulk would have to be measured. Because of the surface nature of a field emission energy distribution it is impossible by this technique to measure the penetration depth of this state. Therefore the proof that this is a surface state still hinges on model calculations such as the one outlined above. This fact led Duke and Fauchier (DuFa72) to attempt a model calculation which would explain the observed behavior of the $\epsilon = -0.37$-eV peak without invoking the presence of a surface state.

Duke and Fauchier's (DuFa72) band structure calculation was discussed in the band structure section (4.2b). The essence of their ideas is the superposition of emission from two independent bands, a narrow tightbinding band and a broad free-electron band. The narrow band produces the peak in the clean energy distribution. In their model this peak is diminished in amplitude when a potential well (delta function) with a bound state slightly above or below the tightbinding band energy is placed close enough to the surface to form "bonding and antibonding" molecular energy levels with the surface atom. This shifts the bulk energy level on the surface atom causing a reduction in the tunneling current in the energy range of the tightbinding band. With Duke and Fauchier's calculation (DuFa72) the pendulum has made a complete cycle. They have returned to the band structure explanation (Ga69a, NaC69, PoC70) to quantify, expand, and illustrate ideas put forth by Plummer and Young (PlY70) when they first observed the surface sensitivity of the $\epsilon = -0.37$-eV peak. Duke and Fauchier's mode calculation does not explain the experimental fact that the angular dependence of the surface state structure varies in the same way that the gap does, as discussed previously. From the fact that the hump follows the gap, it seems reasonable to expect that the presence of a gap is a necessary ingredient in the theory.

All this discussion means we cannot unequivocally demonstrate by the use of field emission energy distributions that we have observed a surface state. The doubts introduced by the model field emission calculation of Duke and Fauchier (DuFa72) have recently been partially alleviated by the photoemission energy distribution measurements of Waclawski and Plummer

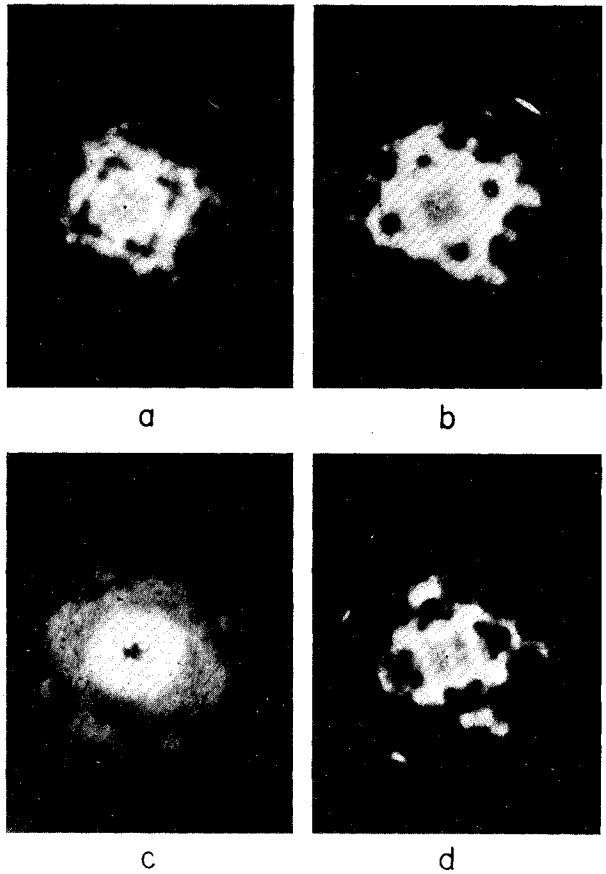

FIG. 24. Ge field emission patterns from test microscope. (a, b) Incompletely cleaned; (a) partial anneal, (b) full anneal. (c, d) Emitter not completely rounded; (c) field evaporated from too rapid field evaporation, (d) clean, annealed. (Sh69.)

(WaPl72). They have reproduced all the essential characteristics of the state observed in field emission. Therefore the field emission process can not produce these observed properties. Unfortunately photoemission measurements are also unable to determine the penetration depth of the surface state!

There are some beautiful and as yet unpublished works on field emission energy distribution from germanium which we feel should be included in this review, even though we stated in the introduction that we would concentrate on metals. Shepherd (Sh69) set up the analyzer system discussed in Sec. 3.2 to study Ge(100) and subsequently Smith and Peria (SmPe71) utilized this analyzer to study the (111) face of Ge. Shepherd cut and etched his emitter from 40 Ω-cm bulk Ge. A series of photographs of the field emission pattern from these emitters is shown in Fig. 24. Figure 24(a) shows the emitter in a condition of partial anneal from the field-evaporated state. The emitter according to Shepherd was not completely clean at this stage, accounting for the spurious emission at the pattern edges. The field emission pattern in Fig. 24(b) is fully annealed. The tip was further cleaned by sputtering before the photographs in Fig. 24(c), (d) were taken. Figure 24(c) is the field evaporated end form while Fig. 24(d) is nearly fully annealed. The void in Fig. 24(c) was caused by too rapid field evaporation. After the tip was formed, field emission energy distributions were studied as a function of surface condition. Annealing was accomplished after field evaporation by heating to approximately 400°C for 5 sec.

The annealed end form in Fig. 24(d) yielded a reproducible energy distribution from the center of the (100) region (center of pattern in Fig. 24). This energy distribution had two peaks. The high-energy peak was between 0.6 and 0.7 eV below the Fermi energy (determined from a tungsten emitter) and was sensitive to the surface preparation and orientation of the emitter. Figure 25 shows the result of rotating the analyzer by increments of several degrees about the pattern center. The high-energy peak definitely is associated with the bright cross in the (100) plane of Fig. 24(d). Shepherd also observed that the high-energy peak was reduced in amplitude with adsorption. This effect is shown in Fig. 26. Note that this is very reminiscent of the surface states on tungsten. Three other observations support this surface state model. (1) Shepherd noted that as the field was increased the relative intensity of the high-energy peak decreased abnormally with respect to the low-energy peak. (2) The intensity of the high-energy peak would oscillate with time as the tip was being slowly field evaporated indicating that the surface state does not exist when the (100) plane is too small. (3) Sputtering the emitter caused disorder and removed the high-energy peak.

Shepherd concluded from a comparison with a theoretical model similar to that developed in Sec. 2 that the lower-energy peak originated from the valence band and the higher-energy peak from a surface state band. The total number of surface states as calculated by Shepherd was 6.3×10^{12} states/cm^2 on the clean annealed emitter. He also concluded that his sensitivity did not allow the observation of the emission from the bottom of the conduction band because it was not in the center of the zone but in the ⟨111⟩ direction.

It would be very interesting to look at this face of Ge using an analyzer with much more sensitivity to see if both the valence band and conduction bands could be located.

Smith and Peria (SmPe71) looked at the (111) face of Ge using the analyzer developed by Shepherd (Sh69). Since the conduction band has its minimum in this direction, it could be observed if populated. They did observe both the conduction and valence bands in their energy distributions. A broad band of electrons with energies in the forbidden gap was also present. This band was ascribed to occupied surface states. The (111) surface was found to be $\sim 1kT$ n type, at an applied field of 40 MV/cm. This corresponded to $\sim 2\times10^{13}$ electrons/cm^2 residing in the filled surface

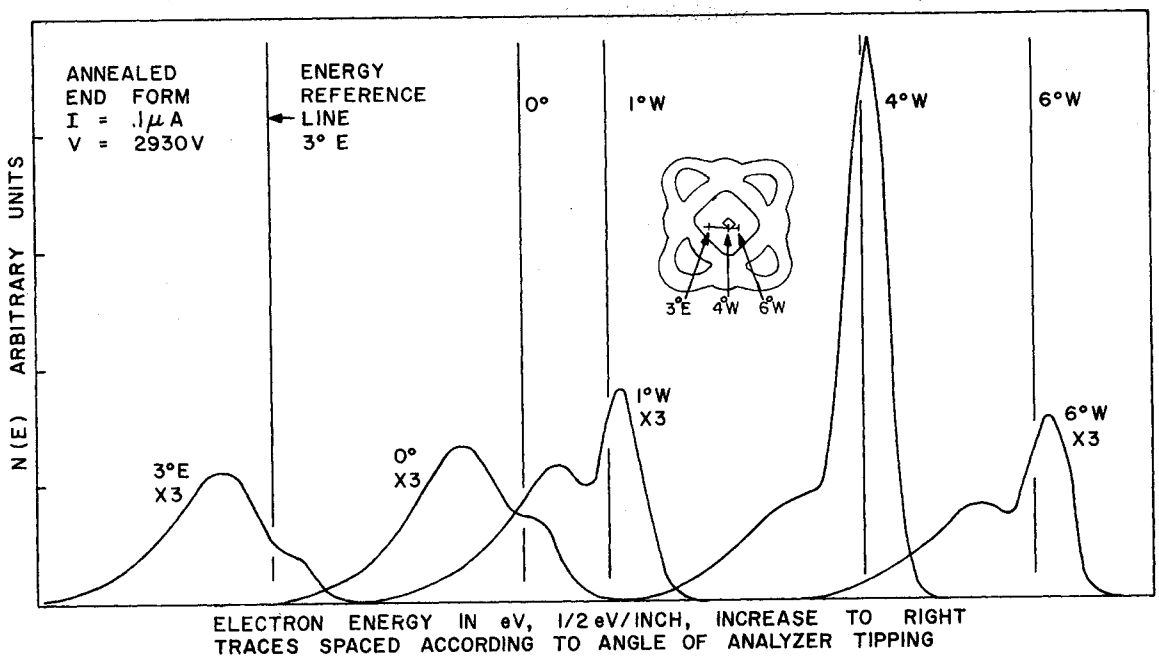

FIG. 25. Energy distributions as a function of position on (100) facet of Ge. Analyzer tipping increments 1–2°. Clean, annealed end form. Tip centered at about 4°W. (Sh69.)

states. Smith and Peria (SmPe71) were able to retrieve more information from their energy distributions than Shepherd by plotting on semilog paper as described in Sec. 3.3. Both of these studies suggest that field emission energy distributions may be very useful for studying semiconductors, *if* the emitters can be prepared.

It is very encouraging that this surface state on (111) Ge has also been observed in photoemission (EaCr72, WaSp72).

4.3. Thermal Field Emission

So far we have been concerned with emission from energy levels very close to the Fermi energy. The population of higher energy states by temperatures in the range 1000–2000 K allows one to obtain some interesting information concerning the shape of the surface potential. Dolan and Dyke (DoDy54) presented the first calculations for high-temperature field

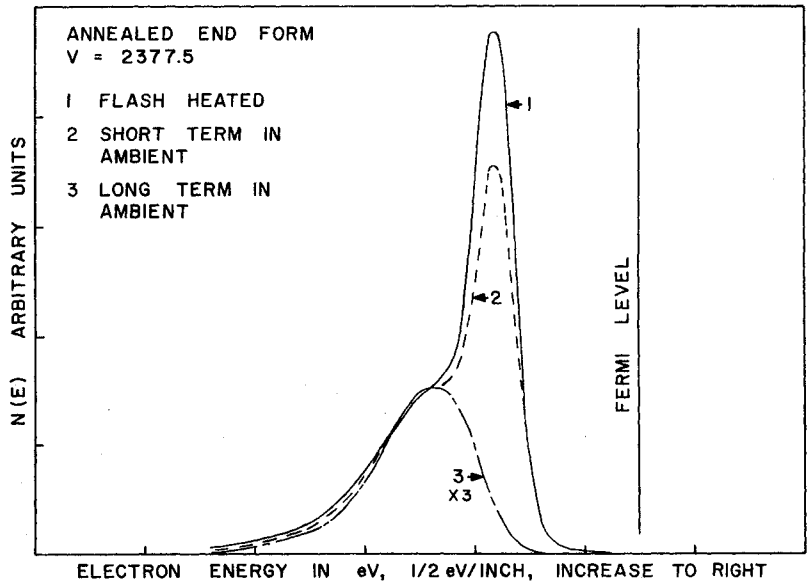

FIG. 26. Energy distribution from the center of the (100) facet of Ge. Annealed end form. (1) Clean; (2) light ambient contamination; and (3) extended ambient exposure. (Sh69.)

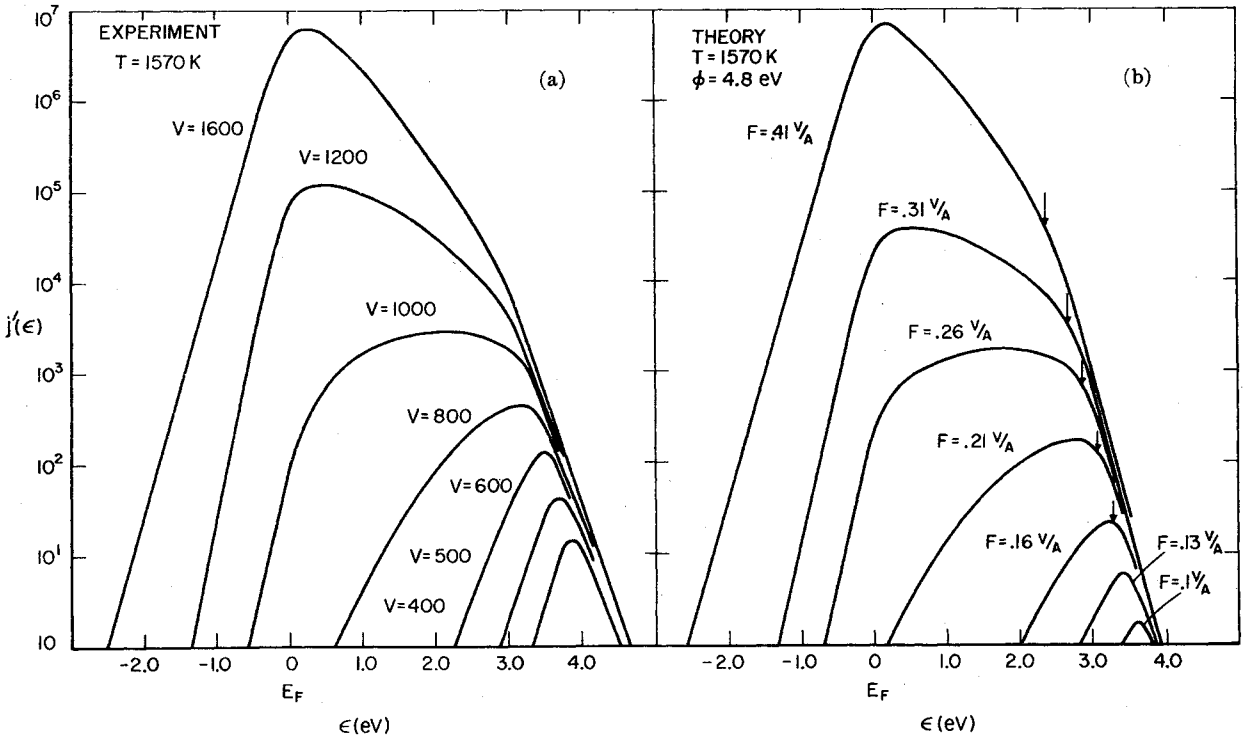

FIG. 27. (a) Experimental TED with emitter-to-anode voltage varied parametrically for $T=1570$ K. (b) Theoretical TED with field treated parametrically for $\varphi=4.8$ eV and $T=1570$ K. The units of j' are arbitrary. (GaP71.)

emission using the Sommerfeld–Bethe transmission function (SoBe33). They calculated normal energy distributions for a range of temperatures in which the emission mechanism went through the transitions from pure field emission to thermal field emission to pure thermionic emission. Murphy and Good (MurG56) used the tunneling probability given by the Miller and Good approximation (MG53) to calculate normal energy distributions.

Gadzuk and Plummer have presented an experimental and theoretical study of thermal field emission which we will now discuss (GaP71). The experiments were performed using a tungsten field emitter and the Kuyatt–Simpson-type spherical deflection energy analyzer (KP72). The inherent thermal noise in a field emitter was overcome by appropriate signal averaging using a multichannel analyzer. The field emitter was dc heated at 1570 K (measured by an optical pyrometer) in the presence of an electric field for many hours prior to making an energy distribution measurement in order to stabilize the emitter end form. As a consequence of this prolonged heating, a noticeable carbon contamination built up on the tip which raised the work function (GM56) above 4.4 eV. There was no noticeable contamination from the ambient gases at the pressure of 10^{-11} Torr during a measurement.

For calculation of the thermal energy distribution, the following procedure was adopted. The Miller–Good tunneling probability of Eq. (2.15) was taken to provide an adequate representation of the tunneling probability. Since the emission occurs for sufficiently large electron energies so that the expansion parameter $|W-E_F|/\varphi_e$ is not small, the exact WKB phase integral, given in Eq. (2.13), is used in Eq. (2.15) which is then inserted into the TED expression of Eq. (2.5) which is then integrated numerically.

The results for a sequence of $T=1570$ K TED's are shown in Figs. 27(a) and (b). Figure 27(a) displays the experimentally measured results for a series of emitter-to-anode voltages corresponding to electric fields at the tip ranging from ~0.08 to 0.4 V/Å. Voltage has been taken as the variable parameter rather than field because of inherent ambiguity in field determinations in field-emission experiments (YC66). In Fig. 27(b), the numerical values of the TED calculated as described above are shown treating F parametrically. The theoretical field F is calculated to be consistent with the slope of the experimental Fowler–Nordheim plot, the assumed work function, $E_F=8$ eV, and $T=$ 1570 K. A choice of work function $\varphi_e=4.8$ eV gives the best overall coincidence between theory and experiments.

As seen in Figs. 27(a) and (b), the similarity between experiment and theory is good. Three distinct regions in the TED are to be noted: (i) exponentially decaying tails at low energies with slope $1/d$; (ii) high

energies with slope $-1/kT$, displaying, respectively, the usual tunneling probability for electrons with energies near the Fermi energy and in the Boltzmann tail of the Fermi function; and (iii) the intermediate transition region in which the log slope is either positive or negative depending upon the values of field and temperature but always with a distinct change of log slope near the barrier top $\epsilon=E_m-E_F$, with E_m the maximum value of the barrier. The value of E_m-E_F marked by arrows in Fig. 24(b) seems to be experimentally significant. From image-potential theories, the barrier maximum occurs at a distance $z_m=(e/4F)^{1/2}=1.9/F^{1/2}$ Å from the surface where F is in units of V/Å and z_m in Å. Both E_m and z_m depend upon the accuracy of the image-type approximation, and since experimental values of E_m are consistent with the value of E_m obtained from an image-potential picture, the results presented here suggest that image-potential theories should be meaningful, even to distances $z_m\simeq$3–4 Å from metal surfaces. This is the order of electron–metal separation which Sachs and Dexter suggest may result in the breakdown of the image potential due to other quantum-mechanical effects (SaDe50). Studies of such effects as periodic Schottky deviations have also shown that the image potential is reasonable, but only for electron–metal separations at least an order of magnitude greater than the values in the present study (CGi58). Although the uniqueness of the image-potential approximation to the surface potential has not been proven, its utility for the TED has been displayed. To our knowledge, this is the most direct study demonstrating the implications of surface-potential shapes at such small distances from the metal surface and provides support for the use of the image potential at a metal surface.

The necessity of using the full analytic form of the tunneling probability including image force corrections and no expansions about the Fermi energy when interpreting TED ranging over several eV has also been established. From a theoretical point of view, the utility and general reasonableness of the Miller–Good WKB-like approximation for describing tunneling near the top of a barrier has also been displayed (GaP71).

4.4. Many-Body Effects

One of the major triumphs in junction tunneling work has occurred in the study of many-body effects in either the electrodes or the intermediate oxide layer (Bl69, Du69). Such effects as the BCS superconducting density of states (G60), phonon structure on the BCS density of states (McRo68), or phonon (MaDu66), and plasmon (DaDu69, EcNg71) self-energy effects depend upon extremely fine energy resolution relative to that obtainable with a field emission configuration. Since these effects are the conventional many-body effects studied in junctions, the many-body features obtainable in field emission studies would be expected to be quite different. In Sec. 4.4a we will discuss single quasiparticle processes in field emission. Multi-quasiparticle effects will be treated in Sec. 4.4b.

4.4a. Single-Particle Tunneling

In a normal interacting electron gas, the model for a metal conduction band, dynamic electron–electron interactions allow the possibility of energy transfer between scattering electrons. Consequently, the electron states which are eigenfunctions of a single-electron time-independent Schrödinger equation do not provide an adequate description of the interacting electron gas since now a bare electron state possesses a possibly complex self-energy and thus a finite lifetime with respect to decay in the solid. The good eigenstates of the many-body system are now quasiparticle states which include the effects of both a given electron state and the polarization cloud around the propagating electron or hole. The interested reader is referred to the excellent review by Hedin and Lundqvist (HeLu69) for a detailed discussion of the physics of the interacting electron gas. For present purposes the salient features relevant to field emission tunneling are the following: The electron–electron interactions, for energies less than the plasmon threshold, alter the form of the single-electron propagator or Green's function which is used in Eq. (2.24) for the TED; within the transfer Hamiltonian formalism, many-body processes result during tunneling. The transfer or tunneling term implies that for every bare physical electron created on the right (in vacuum), one electron must be removed from the left. Since the quasiparticles on the left are not bare electrons, the removal of the bare electron initiates a readjustment or response of the electron gas to this removal which could influence the tunneling characteristics. The inclusion of the electron spectral weight function Im $G(\mathbf{k}, E)$, in Eq. (2.24) allows for the types of many-body effects discussed here.

Mathematically, the "single-electron" many-body effects enter field emission theory as follows. The most general single-electron Green's function is

$$G_1(\mathbf{k}, \epsilon)=[\epsilon-\epsilon_k-\Sigma_r(\mathbf{k}, \epsilon)-i\Sigma_i(\mathbf{k}, \epsilon)]^{-1},$$

with $\epsilon_k=(\hbar^2k^2/2m)-E_F$ the noninteracting gas excitation energy and $\Sigma_r(\mathbf{k}, \epsilon)$ and $\Sigma_i(\mathbf{k}, \epsilon)$ the real and imaginary parts of the electron self-energy due to propagation in the many-body medium. The quasiparticle spectrum is given by poles of the Green's function, $\epsilon=\epsilon_k+\Sigma_r(\mathbf{k}, \epsilon)$ when $\Sigma_i(\mathbf{k}, \epsilon)\simeq 0$, which must be solved iteratively or graphically, since Σ_r which determines the value of ϵ is itself a complicated function of ϵ. On the other hand, if a physical electron tunnels from the solid, a bare hole with energy ϵ_k is left behind; this then propagates and inelastically scatters off the electron gas. Consequently, the particle energy is shifted by Σ_r and an energy uncertainty due to finite lifetime effects is acquired, as evidenced by a nonvanishing Σ_i. It would

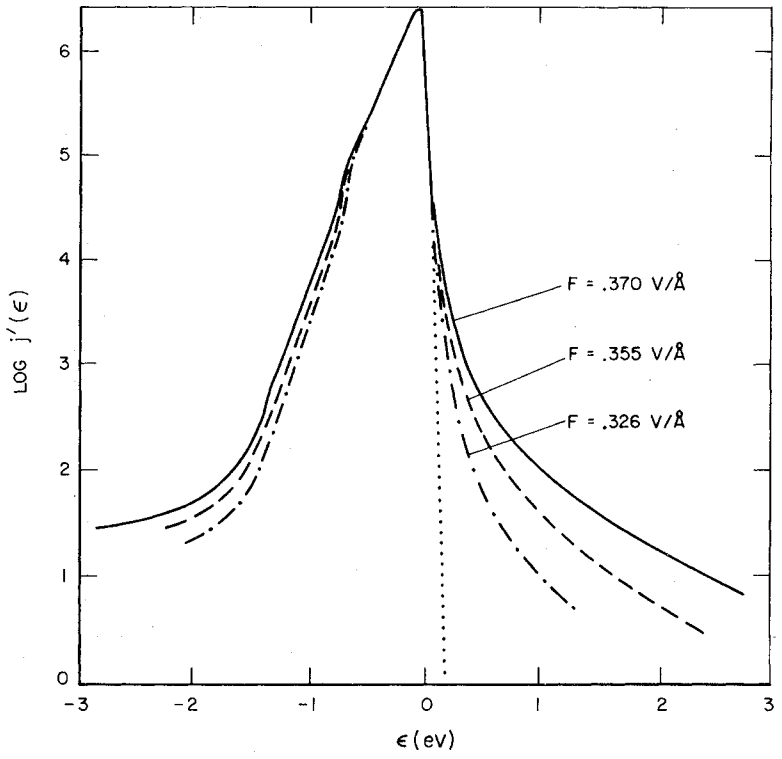

FIG. 28. TED from (111) W at 78 K. The curves are normalized properly with respect to one another although the units of j' are arbitrary on the drawing. (GaP71a.)

be hoped that since a field emitted electron whose energy is measured to be ϵ could come from states within $\sim\pm\Sigma_i$ of ϵ in the metal, these many-body effects might influence the TED in a detectable way. Some specific cases are now stated:

(1) Noninteracting electron gas: $\Sigma_r=\Sigma_i=0$,

$$\text{Im}\, G(\mathbf{k},\epsilon)=\pi\delta(\epsilon-\epsilon_k),$$

which is the standard result.

(2) Quasiparticle approximation: $\Sigma_i\simeq 0$,

$$\text{Im}\, G(\mathbf{k},\epsilon)=\pi Z(\mathbf{k},\epsilon)\delta[\epsilon-\epsilon_k-\Sigma_r(\mathbf{k},\epsilon)]$$

$$Z(\mathbf{k},\epsilon)\simeq\{1-[\partial\Sigma_r(\mathbf{k},\epsilon)/\partial\epsilon]\}^{-1}|_{k=k_F,\epsilon=\epsilon_f}\leq 1.$$

Since the quasiparticle renormalization $Z(\mathbf{k},\epsilon)$ (or the residue at the pole) is slowly varying with both $\mathbf{k}$ and ϵ, Z is taken out of the integrals in Eq. (2.24) and the resulting TED is the regular result multiplied by $\sim Z(k_F,\epsilon_f)$, which does not change the shape of the TED. Consequently, many-body effects which can be treated by the quasiparticle approximation will not be readily detectable in field emission studies.

(3) Interacting electron gas:

$$\text{Im}\, G(\mathbf{k},\epsilon)=\pi^{-1}\frac{\Sigma_i(\mathbf{k},\epsilon)}{[\epsilon-\epsilon_k-\Sigma_r(\mathbf{k},\epsilon)]^2+\Sigma_i(\mathbf{k},\epsilon)^2}. \quad (4.9)$$

This would be the ideal way to proceed, using the energy-dependent self-energies calculated by Lundqvist (BLu67, 68). Still Im G would have a peak at $\epsilon_k+\Sigma_r$ on top of the long-range Lorentzian-like wings. The important contribution to the field emission current probably comes from the quasiparticle peak.

Starting from the equation of motion method (AB63), Gadzuk (Ga69) has obtained a general equation which allows a treatment of many-body effects on either side of the barrier. The expression for the energy distribution, a specific application of Eq. (2.24) due to Appelbaum and Brinkman (ApBr69), is

$$j'(\epsilon_q)=(J_0/d)\int d\epsilon_k\, d\omega\pi^{-1}\,\text{Im}\, G_R(\mathbf{q},\omega)\pi^{-1}$$

$$\times\text{Im}\, G_L(\mathbf{k},\omega)f_L(\omega)\exp(\epsilon_{k/d}). \quad (4.10)$$

In Eq. (4.10), Im $G_{L(R)}(\mathbf{k}(\mathbf{q}),\omega)$ is the imaginary part of the Green's function on the left (right) side of the barrier for elementary excitations with energy spectrum $\omega=\epsilon_k(\omega=\epsilon_q)$ and f_L is the Fermi function for the unperturbed metal. Recently this result has been rederived by Leung (Le71) using a similar approach. Gadzuk evaluated Eq. (4.10) for several limiting cases; namely, the free-electron gas (which reproduced the standard results), a superconductor [which gave the not unexpected result that the TED is affected only within the energy range of order of the gap parameter, much smaller than the resolution of the instrument (GoKu67, Le68)], a resolution limited configuration [which effectively alters Im G_R to give the result of Eq. (2.22)], and an interacting electron gas. Since the quasiparticle peak of Eq. (4.9) was expected to be responsible for the emission current, the peak was

approximated with a Gaussian function and the integration performed assuming both Σ_r and Σ_i = constants. The result was that the standard TED was multiplied by a function of Σ_i which did not change the shape of the TED. If the correct energy dependence of Σ is used, then a slight change in the functional form of j' could result but it is doubtful that it would be sufficiently pronounced to make experimental identification convincing.

Osborne (Os71) has applied Eq. (4.10) to the problem of correlation effects (within the Hubbard model) in narrow band transition metals and to antiferromagnetic Cr. In the case of the transition metals, he concludes that the exchange splitting could alter the TED in the manner discussed by Politzer and Cutler (Po72, PoC72). For antiferromagnetic Cr, using the theory of Fedders and Martin (FeMa66) which amounts to using a spectral weight or Green's function which is functionally equivalent to that of a superconductor, he concludes that one might see the antiferromagnetic gap at the Fermi level since the gap is two orders of magnitude larger than that of a superconductor.

Lastly, Kormendi (Ko72) has applied Eq. (4.10) to the case of photofield emission (Ch66, Neu69, LuWi72). He evaluates the self-energy for the case of single photon emission and absorption and finds that electrons depleted beneath the Fermi energy appear above, due to virtual and real photon processes.

In summary, for excitation energies less than the plasmon threshold, it seems unlikely that many-body effects (other than those of magnetic origin) in the interacting electron gas should alter the *single-particle* tunneling characteristics in field emission in an important manner.

4.4b. Multiparticle Tunneling

Still another possible many-body effect in normal metal field emission pertains to multiparticle tunneling. Due to the fact that electrons, not quasiparticles, are strongly interacting within the metal it might seem reasonable to expect some sort of correlation between tunneling electrons. However, as Wilkins has pointed out with reference to junction tunneling (Wi69), the current goes as the small tunneling probability to the nth power for correlated n particle tunneling. Consequently, in junctions which are essentially retarding potential devices, any n particle tunneling would be superimposed on a much larger background current due to single electron tunneling and would be lost in the noise. (It is assumed that any Josephson effects can be neglected.) As we shall see, some unique features of the field emission configuration eliminate the cited problems of junctions and indeed allow for the observation and interpretation of some possible many-body effects in field emission tunneling.

The experimental observations (LeGo70, Pl70, GaPl71a) which motivated the inquiry into multiparticle tunneling are shown in Fig. 28. These observed TED's from the (111) plane of tungsten were obtained for various field strengths and thus current densities. For energies $-0.7 \lesssim \epsilon \lesssim 0$ eV, the behavior of the TED is what one expects from Eq. (2.18). At lower energies, band-structure and surface state effects give rise to the added structures as discussed in Sec. 4.2. The dotted line above the Fermi energy is the Boltzmann tail predicted at 78 K. The rather striking departure from the Boltzmann tail at high energies stimulated the possibility of a many-body interpretation. Lea and Gomer (LeGo70) demonstrated that the total current in the high-energy tail is proportional to the square of the total current integrated over all energies or, equivalently, to the square of the tunneling probability at the Fermi energy, as discussed in Sec. 2. That is

$$i^* \equiv \int_0^\infty j'(\epsilon)\, d\epsilon \propto \left(\int_{-\infty}^{\infty} j'(\epsilon)\, d\epsilon\right)^2 = J_0^2.$$

Their result is shown in Fig. 29 where it is noted that the log slope of i^* vs J_0 equals two over several orders of magnitude. This seemed to be quite convincing evidence for correlated two-particle tunneling. Lea and Gomer verified this for a maximum value of $\epsilon \approx 0.3$ eV, using a

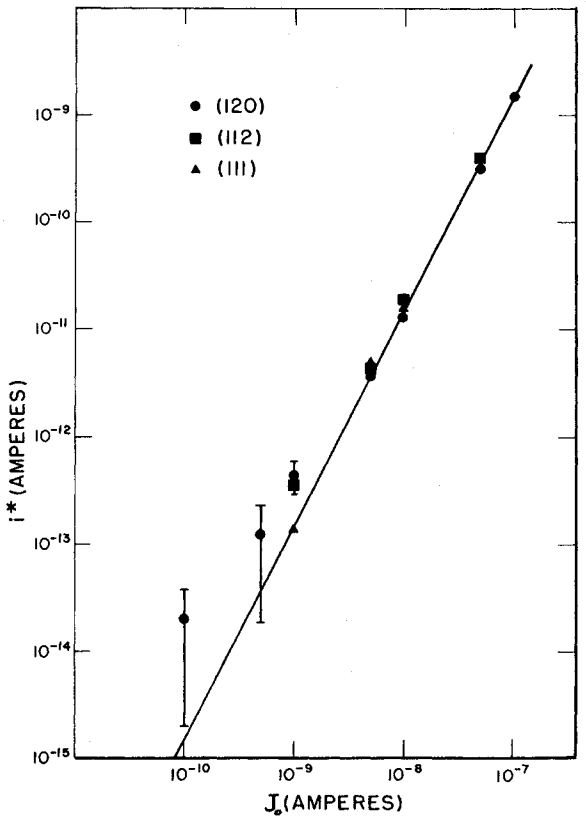

FIG. 29. Plot of i^*, probe hole current arising from electrons emitted with $\epsilon > 0$, versus J_0, total probe current at 20 K for various planes of W. (LeGo70.)

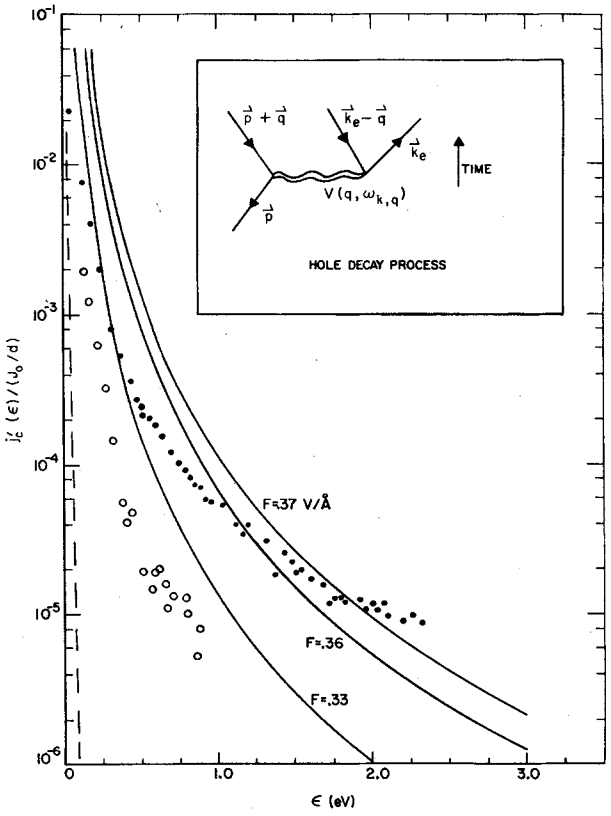

FIG. 30. Solid lines: theoretical calculations for the high-energy tail of the TED. These curves rise to $j_c'/(J_0/d)=1$ at $\epsilon=0$ and then decay exponentially for $\epsilon<0$ in the well-understood way. Dashed line: Usual Boltzmann tail for $T=78$ K. Closed circles: Experimental points for $F=0.37$ V/Å; open circles for 0.326 V/Å. Inset: Diagram illustrating the hole-damping mechanism in which a hole of energy-momentum E_p, p scatters from the electron gas exciting an electron–hole pair of energy-momentum ω_{pq}, p. The electron momentum is k_e. (GaP71a.)

retarding potential analyzer. Plummer (Pl70, GaPl71a) using the differential electrostatic analyzer described in Sec. 3 (KP72), has confirmed these results for ϵ_{max} up to 4.0 eV.

Gadzuk and Plummer have provided a quantitative theory of the high-energy tail (GaP71a). Following the suggestion of Fischer (Fi70) and Lea and Gomer (LeGo70) that two electron processes are involved, the following mechanism was envisioned. An electron with energy $E_p<E_F$ tunnels from the metal leaving behind a "hot hole". The hot hole, in analogy with hot-electron injection (Me62, CrSz67, Ka70), can then be scattered by the electron gas (electrons in the metal conduction band) producing a secondary hole and electron as shown in the inset in Fig. 30. The interaction occurs via a momentum- and frequency-dependent screened Coulomb interaction which involves the dielectric properties of the electron gas. The electron produced by the hole decay may then tunnel out of the metal with a considerably enhanced tunneling probability and be observed in the high-energy tail. This picture thus requires a knowledge of the quasiparticle decay modes in the interacting electron gas (QFe58, Ri59, Q62, DoLe69) or alternatively, can provide information on these lifetime effects. For electrons in the high-energy tail produced by the cascade process, G–P have postulated that the cascade distribution $j_c'\equiv dj_c/d\epsilon$ is

$$j_c'=\frac{J_0}{d}\exp(\epsilon/d)\int_{-\infty}^{-(\epsilon-E_F)}u(\epsilon;\epsilon_p)e^{-c}\times\exp(\epsilon_p/d)\,d\epsilon_p, \quad (4.11)$$

with $u(\epsilon;\epsilon_p)$ the decay "kernel" relating the number of secondary electrons at energy $\epsilon>0$ produced from the decay of a primary hole at energy $\epsilon_p<0$. Using an expression for u, derived by Ritchie (Ri66), G–P then have shown that Eq. (4.11) can be written in standard form in terms of E_n, the nth-order exponential integral (HMF65)

$$j_c'=J_0^2\left(\frac{3h^3}{10\pi med^3}\right)\frac{E_F(E_F+\epsilon)}{\epsilon^2}\left\{\frac{d^2}{\epsilon^2}+\frac{14}{9}\frac{d}{\epsilon}-e^{\epsilon/d}\left[E_4\left(\frac{\epsilon}{d}\right)+\tfrac{5}{9}E_3\left(\frac{\epsilon}{d}\right)\right]\right\}. \quad (4.12)$$

Equation (4.12) has been written in a form emphasizing the quadratic dependence on the total current J_0. It has been numerically evaluated for parameters $\varphi_e=4.45$ eV and $E_F=9$ eV which characterize (111) W. Taking various values of fields which are consistent with the experimental data shown in Fig. 28, $j_c'(\epsilon)/(J_0/d)$ vs ϵ for energies above the Fermi energy is shown in Fig. 30. Experimental points from Fig. 28 are also drawn to demonstrate the agreement. The major features of the data which the model explains are these: (i) Correct energy dependence of j_c', falling off as inverse powers of ϵ. Simple phase-space or density-of-states arguments do even worse in that they predict increasing j_c' with increasing ϵ (LeGo70). (ii) Correct field dependence of the theoretical j_c', rising relative to $j_0'(0)$ as the field does, and in fact varying quadratically with J_0. Here $j_0'(0)$ is the value of the usual TED at the Fermi level. (iii) Correct order of magnitude for the anomalous tail. Herring has also put forth a similar model (Her70). In order that Ritchie's calculation for $u(\epsilon;\epsilon_p)$ could be used, G–P had to assume that the injected hole remained localized within ~5 Å from the surface. That this is so is seen from a subtle surface effect. As discussed by Juretschke (Ju53), the image potential at a metal surface is a result of a surface screening-charge pileup which in the case of electron emission is the injected hot hole. As long as the emitted electron is interacting with the metal via the long-range potential, the charge deficiency or hot hole is localized near the surface within a few screening lengths, well within the 5 Å used by G–P.

Bari and Ngai (NgBa71) have used this concept of

the image localized hole to interpret the behavior of the high-energy tail as $\epsilon \to 0^+$ in terms of singularities due to the transient response of the electron gas to the sudden switching on of the potential caused by the hole. ("Sudden" is faster than several plasmon oscillations.) These singularities are familiar in x-ray spectra in solids (Ma67, NoDe69, DoSu70) and are to be expected for any process in which a "massive" or stationary hole is produced rapidly. Further work along these lines will certainly lead to enhanced understanding of electron gas response behavior.

Bari and Ngai have outlined a seemingly different approach to a theory of the high-energy tail in which they explicitly consider "simultaneous" two-particle tunneling. By formulating the theory in terms of two-particle Green's functions, any correlated tunneling between two electrons is automatically accounted for in the so-called bound part of the two-particle propagator defined through

$$G_2(1, 2; 1', 2') = G_1(1; 1')G_1(2; 2') + G_1(1; 2')G_1(2; 1') + G_2^B(1, 2; 1', 2').$$

Obviously G_2^B, the bound part of the propagator, contains all two-particle information other than the independent particle motion described by the direct and exchange single-particle propagation. This however only defines G_2^B, and does not give any hint as to how to make it computationally accessible. Unfortunately the equation of motion for G_2^B is coupled to the one and three particle equations of motions, etc. In order to reach a solution, a model which most likely would be similar to Ritchie's must be invoked.

Herring has suggested that point for point agreement between the theory and experiment will obtain if an energy dependence is given to the hole confinement length (Her70). From these initial studies some information about the quasiparticle lifetimes has been obtained. More detailed and careful analysis of the high-energy tails could ultimately provide considerable information pertaining to the low-energy excitations in interacting Fermi systems.

Gadzuk and Lucas (GaLu73) have provided another possible interpretation of both the high- and low-energy tails in terms of lifetime effects in quasistationary or decaying states. (RiGoo62, LiO'M70). In short, the idea is that the original bound energy eigenstate of the metal is transformed into a decaying state with complex energy $\epsilon = \epsilon' - i\Delta(\epsilon')$ upon application of the field. The level width is $\Delta(\epsilon') \simeq \hbar/\tau$, where τ is the "tunneling time" for a bound electron with energy ϵ' in the metal. Thornber, McGill, and Mead (ThMcMe67) suggest that the relevant tunneling time is the effective *RC* time constant of the capacitor modeled tunnel structure with R the resistance and C the capacitance. This results in a level width of the form

$$\Delta(\epsilon') = \Delta_0 \exp\left[(-c + \epsilon'/d)\right].$$

The consequence of this effect amounts to folding the zero-order energy distribution into a broadening function so that the observed high-energy distribution is

$$j'(\epsilon) = \int_{-\infty}^{+\infty} j_0'(\epsilon')\pi^{-1} \frac{\Delta(\epsilon')}{(\epsilon - \epsilon')^2 + \Delta(\epsilon')^2}\, d\epsilon',$$

which results in

$$j'(\epsilon) \simeq \frac{J_0^2}{d\Gamma_j} \frac{d\Delta_0}{2\pi\epsilon^2} \left\{1 - \frac{d}{\epsilon} + \frac{3d^2}{2\epsilon^2} - \cdots\right\}, \quad (4.13)$$

with $\Gamma_j \equiv J_0 e^{+c}$. Equation (4.13) possesses the characteristics of the observed tails, varying as the square of J_0 and falling off as inverse powers of ϵ away from the Fermi level. Using the *RC* time constant of the capacitor model of field emission to obtain an estimate of Δ_0 gives tails which are of the right magnitude to contribute to the current. It seems likely that both the many-body effects and the lifetimes are making nearly equal contributions which could complicate the extraction of many-body information. An interesting but unfortunate consequence of the lifetime tails is that the tails from the higher-energy electrons dominate the observed TED at lower energies. This places an inherent limit on the range of energies accessible in field emission energy distributions, no matter how perfect the analyzer is. It appears that for metals with work functions in the 4.5-eV range, studies from clean surfaces will be restricted to a depth of less than 2 eV beneath the Fermi level.

One final point is made here to further illustrate that information obtainable from junction and field emission tunneling can compliment each other. On the one hand, the many-body effects described in this section would be impossible to observe in a two-electrode junction. In field emission the application of the field allows tunneling of electrons from all occupied states in the metal. This tunneling then creates the high-energy component of electrons which although small can be observed and energy analyzed without being obscured by the lower energy electrons. This of course is accomplished by the third element in Fig. 1. On the other hand, in a tunnel diode, to generate higher-energy electrons by hole injection, a voltage is applied between the two electrodes causing a current flow and thus cascade produced electrons. However all the electrons, both primaries and cascade secondaries ($\sim 10^{-3}$ of primaries), go to the lower-energy electrode and thus the secondaries are lost in the noise. It is encouraging to see that many-body effects can be uniquely studied by FEED which are equally sophisticated to those observed in junction work.

5. ADSORPTION STUDIES

The use of FEED studies to provide detailed information on a microscopic level about adsorption phenomenon has been particularly successful and

interesting. It is nearly impossible to meaningfully cover all work in this field so we have chosen some representative research pertaining to a few subject areas to display the versatility of the FEED technique. From convenience, the chosen areas reflect the personal involvement of the authors. Section 5.1 concerns itself with classical studies in which adsorption is believed to affect a TED only through work function changes. Some results of the recent explosion of interest in field emission elastic resonance tunneling are considered in Sec. 5.2. Inelastic tunneling due to surface impurities is the subject of Sec. 5.3.

5.1. Work Function Changes

Unlike FN studies, energy distribution measurements have seldom been used to measure the changes in work function as the coverage of adsorbed atoms increases. There is a fundamental reason for this. The chemisorbed layer alters not only the barrier height but also its shape and width. This complicated situation cannot be characterized by a single parameter, the change in work function. This realization by Duke and Alferieff (DuAl67) opened the era of elastic resonance tunneling to be discussed in Sec. 5.2.

Swanson and Crouser (SCr69) measured work functions obtained from the slope of the energy distribution as a function of adlayer coverage. They studied Ba on (111) Mo and Cs on (100) and (110) W with a van Oostrom retarding-potential analyzer. In general they observed energy distributions which could be brought into agreement with the standard expression, Eq. (2.18), by adjusting the value of φ_e. By taking TED's at many different coverages θ, Swanson and Crouser obtained effective φ vs θ curves which demonstrated linearly decreasing φ_e at low increasing θ dipping to a minimum value of φ_e less than the work function for a solid of the adsorbate and then finally rising with increasing θ to the value of φ_e for the solid adsorbate (L71). However there were many problems regarding anomalous "effective emitting areas," pre-exponentials, and polarizabilities. Work function changes were not the whole story in spite of the superficial agreement with expected φ_e vs θ behavior which leads us to the resonance tunneling interpretations.

5.2. Elastic Resonance Tunneling

The phenomenon of chemisorption has been approached from many different points of view. The last section utilized what might be called the macroscopic approach in that chemisorption was characterized by its effects on material properties, such as work functions, as opposed to atomic properties, such as energy levels. In recent years theoretical studies of the chemisorbed state have concerned themselves with predicting or interpreting macroscopic quantities in terms of atomic properties (Gu35, An61, BeFa66, Ga67, Ne69, GaHaRh71, Gr71, Sc72). In order that these theories be put on a firm foundation, it is necessary to acquire independent information about the atomic states of chemisorbed objects (ions, atoms, molecules). We feel that field emission resonance tunneling is a significant tool for such studies, as we will attempt to demonstrate. The motivation for the resonance tunneling interpretation of field emission in the presence of chemisorbed atoms resulted largely from experimental "problems." As discussed in Sec. 5.1, for many studies of chemisorbed gases on field emitters, the electron emission effects could be characterized by a simple work function change presumably arising from an altered dipole layer at the surface. However there were sufficient inconsistencies in experimental data such as that of Delchar and Ehrlich (DeEh65) to inspire deeper thought on a microscopic level. In particular Delchar and Ehrlich observed that when nitrogen was adsorbed on the (100) plane of tungsten, both the slope of the FN [Eq. (2.19)] was reduced (implying a decrease in φ_e) and also the total current was reduced (implying an increase in φ_e). More dramatic was the study by Ermrich in which molecular nitrogen which has an excited state roughly 1 eV below the Fermi level was adsorbed and electron bombarded while on or near the (100) plane (Er65, ErvO67). In this experiment large FN-determined-work-function increases up to $\sim$4.5 eV were observed with a simultaneous increase in current of up to four orders of magnitude. Clearly some new ingredient to field emission theory was required to understand these unexpected results.

Duke and Alferieff (D–A) (DuAl67) began a new era of field emission work by pointing out the role of elastic resonance tunneling through virtual energy levels of atoms or molecules adsorbed on metal surfaces. Essentially they realized that adsorption of an atom can not only vary the surface barrier, resulting in a real work function change, but also can vary the shape or effective "thickness" of the barrier due to the presence of the attractive potential well of the adatom. Thus although the thermodynamically defined work function could remain constant, the field emission tunneling probability could drastically change, such that the experimental field emission characteristics, either FN or TED curves, would be nonsensical when work function is used as the only fitting parameter. In Fig. 31 a schematic potential diagram is shown in which the adatom potential is taken to be a square well. If the adatom has a virtual energy level near the Fermi energy, then an electron tunneling from a metal state Ψ_m to a vacuum state Ψ_f can go either via the direct channel or through the intermediate resonance atomic state Ψ_a. The latter case is particularly advantageous because the atomic potential cuts a hole in the potential barrier which should reduce the WKB phase integral of Eq. (2.11) and thus increase the transmission function.

In their landmark paper, D–A drew upon the substantial body of knowledge dealing with the problem of

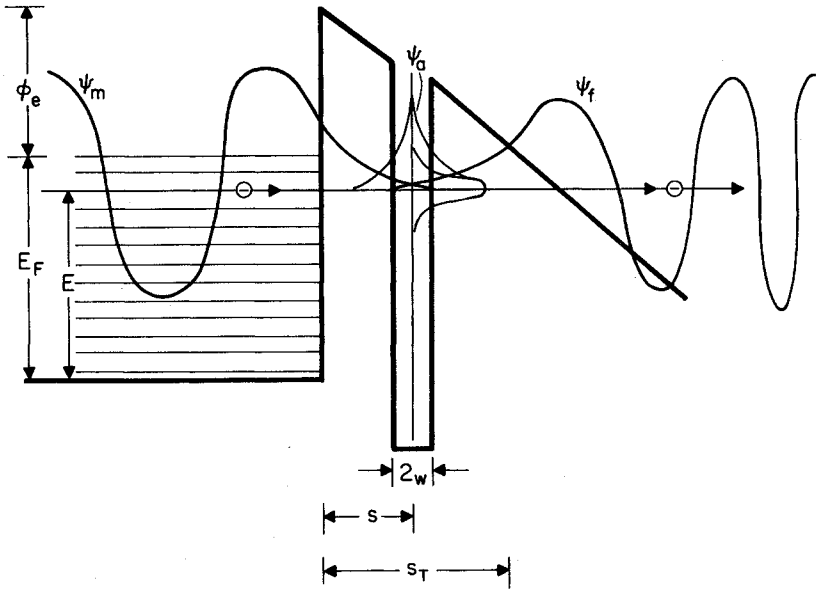

FIG 31. Schematic model showing the idealized potentials relevant in resonance tunneling. The electron wave functions are: Ψ_m, the unperturbed metal function; Ψ_a, the localized virtual impurity function; and Ψ_f; the emitted electron function. (Ga70.)

double barrier penetration (Bo51, Me61, Pe62, I63, I64, Sc66). Succinctly stated, if the energy of the tunneling electron is the same as the energy of a standing wave between the two potential hills (in our case the valley is the attractive atomic potential), then barrier penetration is much easier. One would hope that the energy of the standing waves in the case of adsorbed atoms would be related to the allowed energy states of the atom which might however be broadened and shifted due to the interaction of the atom with the solid (Gr71, Sc72). Then an energy distribution of electrons field emitted through the adatom would tend to display structure which could be related to the energy spectrum or local density of states of the adatom. D–A illustrated this point by performing an exact wave matching calculation (see Sec. 2.2a) for the triangle barrier with various combinations of square well and delta function model potentials representing the atom core. With their model calculations they also were able to show that neutral adsorbates with repulsive pseudopotentials could lead to reductions in total current with no change in work function. Due to the numerical nature of the D–A theory it was hard to interpret actual experimental field emission data in terms of the atomic parameters such as level positions and widths which are the basic ingredients of chemisorption theories (BeFa66, Ga67, Ne69, GaHarRh71, Gr71, Sc72).

From the D–A theory came the realization that an atomic spectroscopy of adsorbed atoms would be possible. In this pursuit Clark and Young, following the procedure of Holscher (Ho67), showed that single adatom chemisorption could be observed in a field emission microscope in their study of strontium on tungsten (ClY68). As outlined in Sec. 3, emission from ~30 surface atoms on the desired single-crystal face was directed through the probe hole in the fluorescent screen of the anode. Next the Sr source was turned on. When the first Sr atom arrived at the plane viewed by the probe hole, the total current took a step function jump by about a factor of five corresponding to an enhancement of ~100 in the tunneling current through the Sr atom since the effective emitting area covered is only ~3% of the total area as shown in Fig. 32. At this point the source was turned off and a TED which included emission through the Sr atom was then obtained. The key results of the Clark–Young study relevant to resonance tunneling were that the slope of the FN remained the same while the slope of the TED increased, in accord with the theory of D–A. This result could be understood if the electropositive adsorbate had a broad energy level whose center was above the substrate Fermi level, as expected for the surface perturbed $5s^2$ ground state configuration of Sr.

The first unambiguous observation of adatom energy levels was given by Plummer, Gadzuk, and Young (PGaY69) in their study of zirconium on tungsten. An alternate theory of resonance tunneling was also sketched which enabled closer identification of TED results with atomic spectra. The experimental and theoretical results were greatly extended when barium and calcium were studied (Ga70, PY70). The study of germanium atoms and films has also been completed and will be discussed (SoMi61, 63, 64, 64a, 66; GaPClY70; Cl71).

A fairly transparent theoretical picture of resonance tunneling has been formulated (PGaY69, PY70, Ga70, 71, GaPClY72, Gl71). In retrospect, the essence of the theory can be seen to be quite similar to Appelbaum's theory of *s–d* exchange tunneling in junctions doped with paramagnetic impurities near one of the interfaces (An66; Ap66, 67; WoLo70). Recently Penn, Gomer, and Cohen (PeGoCo72) have reformulated the

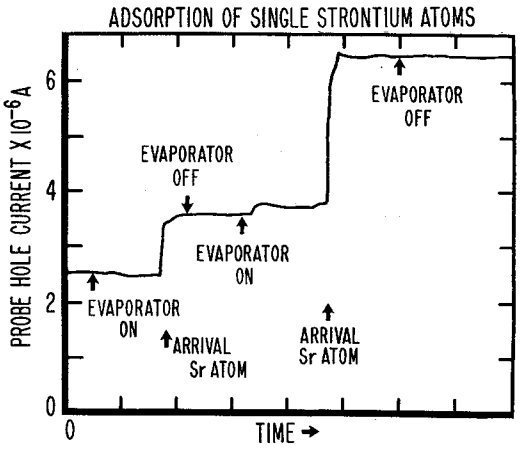

FIG. 32. Probe hole current versus time as the strontium source is switched on and off. The step increase in current occurs when a single Sr atom arrives upon the surface being viewed. (ClY68.)

problem in terms of Anderson model (An61) chemisorption and tunneling Hamiltonian field emission. In this section we will first consider resonance tunneling from a simple physical point of view and then make contact with the theory of Penn *et al.*

From Eq. (2.23), we take the illustrative example in which the TED is given simply by

$$j'(\epsilon)=cf(\epsilon)\mid\langle f\mid H_T\mid i\rangle\mid^2$$

with c a constant or slowly varying function of ϵ. In the case of an emitter with no adsorbed atoms, the initial state is simply the metal state and thus $\mid i\rangle=\eta\mid m(\epsilon)\rangle$. When no confusion arises, we will write $\mid m(\epsilon)\rangle=\mid m\rangle\cdot\eta$ is a normalization factor to be discussed shortly.

In order to describe the TED when chemisorbed atoms are present, we require a chemisorption theory. Such a theory can be constructed which is analogous to the Fano theory (Fa61) for the configuration interaction of a discrete state, the atomic state, with a continuum, the metal conduction band states. The Fano type of theory is a real space theory in terms of wavefunctions whereas the equivalent Anderson impurity theory (An61), used by Penn, Gomer, and Cohen (PeGoCo71, 72) in their resonance tunneling theory is an occupation number space theory.

When properly implemented, both theories give the same results since the physics considered must be representation independent. Here we will concentrate on the real space theory for expository purposes.

First one is interested in the initial state wave function, before tunneling, of the total system of metal plus hypothetical single level atom. This wave function, which is labeled $\mid i, a\rangle$, is similar to Fano's wave function for a discrete state mixing with a continuum. Adapting Fano's Eqs. (1), (2), (4), (9), and (13) to the present notation, we have that

$$\mid i,a\rangle=a(\epsilon)\mid a\rangle+\int d\epsilon'\rho_m^{1/2}(\epsilon')b_{\epsilon'}(\epsilon)\mid m(\epsilon')\rangle, \quad (5.1a)$$

with

$$a(\epsilon)=\rho_m^{1/2}(\epsilon)\langle m(\epsilon)\mid V_{a-m}\mid a\rangle/[\epsilon-\epsilon_\varphi-i\Delta_a(\epsilon)], \quad (5.1b)$$

$$b_{\epsilon'}(\epsilon)=[(\epsilon-\epsilon')^{-1}+Z(\epsilon)\delta(\epsilon-\epsilon')]\rho_m^{1/2}(\epsilon')\times\langle m(\epsilon')\mid V_{a-m}\mid a\rangle a(\epsilon), \quad (5.1c)$$

$$Z(\epsilon)=(\epsilon-\epsilon_\varphi)/\rho_m(\epsilon)\mid\langle m(\epsilon)\mid V_{a-m}\mid a\rangle\mid^2, \quad (5.1d)$$

and

$$\Delta_a(\epsilon)=\pi\rho_m(\epsilon)\mid\langle m(\epsilon)\mid V_{a-m}\mid a\rangle\mid^2. \quad (5.1e)$$

Here $\mid a\rangle$ is the unperturbed atomic state. The metal density of states $\rho_m(\epsilon)$ appears explicitly since our metal wave functions are normalized over the real space of the metal, whereas Fano normalized the continuum wavefunctions "per unit energy." Thus we have $\eta=\rho_m^{1/2}$ for the metal state normalization. The matrix element $\langle m\mid V_{a-m}\mid a\rangle$ is a measure of the strength of the coupling between metal and atomic states and V_{a-m} is the interaction providing the coupling. The real part of the energy denominator is determined through $\epsilon_\varphi=\epsilon_a+\Delta\epsilon-eFz$ with ϵ_a the isolated atom energy, $\Delta\epsilon$ the shift in energy due to interactions between atom and metal states, image potential corrections, and average intra-atomic Coulomb repulsion between electrons of different spins, and eFz the lowering of the energy due to the applied field. $\Delta_a(\epsilon)$ is the imaginary part of a "self-energy" due to the atom–metal interaction or, equivalently, the virtual level width. It is also understood that the $(\epsilon-\epsilon')^{-1}$ term in $b_{\epsilon'}(\epsilon)$ is to be evaluated only as a principle part integral in Eq. (5.1a). Now consider the terms multiplying the delta function in $b_{\epsilon'}$ which, with $Zva\equiv Z(\epsilon)\langle m(\epsilon')\mid V_{a-m}\mid a\rangle a(\epsilon)$, can be written in the form $Zva=1+Zva-1$. When represented in this way, it is a straightforward matter to show that the initial Fano state, Eq. (5.1a), for the chemisorption situation can be written as

$$\mid i,a\rangle=a(\epsilon)\mid a\rangle+\rho_m^{1/2}(\epsilon)\mid m(\epsilon)\rangle+a(\epsilon)\sum_{\epsilon'}[\mid m(\epsilon')\rangle\langle m(\epsilon')\mid V_{a-m}\mid a\rangle/(\epsilon-\epsilon')],$$

or more succintly, as

$$\mid i,a\rangle=a(\epsilon)\mid a'\rangle+\rho_m^{1/2}(\epsilon)\mid m(\epsilon)\rangle \quad (5.2)$$

with

$$\mid a'\rangle=\mid a\rangle+\sum_{\epsilon'}[\mid m(\epsilon')\rangle\langle m(\epsilon')\mid V_{a-m}\mid a\rangle/(\epsilon-\epsilon')],$$

where, following Penn (Pe72), we have written the perturbed atom state $\mid a'\rangle$ as a sum of the unperturbed state $\mid a\rangle$ plus a polarization correction due to the V_{a-m} mixing of atom and metal states. In tunneling events, the part of $\mid a'\rangle$ proportional to $\mid a\rangle$ gives a tunneling current from electrons coming directly from the adatom whereas the polarization part gives a current from electrons originally on the adatom which tunnel to the metal via V_{a-m} and then tunnel from the metal to the vacuum. Since the tunneling path is so much longer

for this process and consequently the tunneling probability so much smaller, it is expected that taking $|a'\rangle \simeq |a\rangle$ for field emission resonance tunneling would be a reasonable approximation. This is essentially the approximation used by Gadzuk (Ga70) and its neglect represents one of the major physical differences between his theory and that of Penn, Gomer, and Cohen (PeGoCo71, 72).

Now consider the TED from an adsorbate covered surface to be given by $j_a'(\epsilon) = cf(\epsilon)\,|\langle f|H_T|i,a\rangle|^2$. As suggested by D–A, it is convenient to consider the ratio of energy distributions

$$R(\epsilon) \equiv j_a'(\epsilon)/j_0'(\epsilon) = |\langle f|H_T|i,a\rangle|^2/|\langle f|H_T|m\rangle|^2 \quad (5.3)$$

for current emitted from the area in which the atom sits with j_0' the TED from the clean surface. As discussed in Sec. 3, this method of data analysis removes the strong exponential dependence from the data, thus emphasizing the structure due to the adatom energy levels. This is the form in which most experimental data have been presented. It is also possible to consider the quantity $\Delta j'(\epsilon)/j_0'(\epsilon) \equiv [j_a'(\epsilon) - j_0'(\epsilon)]/j_0'(\epsilon) = R(\epsilon) - 1$. Realizing that the adatom density of virtual states is $\rho_a(\epsilon) = \pi^{-1}\{\Delta_a/[(\epsilon-\epsilon_\varphi)^2+\Delta_a^2]\}$, we can combine Eqs. (5.1)–(5.3) to yield

$$\frac{\Delta j'(\epsilon)}{j_0'(\epsilon)} \simeq \frac{\rho_a(\epsilon)}{\rho_m(\epsilon)}\left|\frac{\langle f|H_T|a\rangle}{\langle f|H_T|m\rangle}\right|^2 \times\left\{1+2\pi\rho_m(\epsilon)\left[\frac{(\epsilon-\epsilon_\varphi)}{\Delta_a}\,\mathrm{Re}\,T(\epsilon)+\mathrm{Im}\,T(\epsilon)\right]\right\}, \quad (5.4)$$

with

$$T(\epsilon) \equiv \frac{\langle f|H_T|a\rangle\langle a|V_{a-m}|m\rangle\langle m|H_T|f\rangle}{|\langle f|H_T|a\rangle|^2}$$

and Re T(Im T) the real (imaginary) part of $T(\epsilon)$. Equation (5.4) shows the strong relationship between the current characteristics and the impurity density of states skewed by the energy-dependent matrix elements. In terms of adatom Green's functions, the resonance term is proportional to the imaginary part of the Green's function whereas the interference term is proportional to both the real and imaginary parts of the Green's function. This point has been considered at great length by Penn *et al.* (PeGoCo71, 72).

The ratio of tunneling matrix elements can be understood in the manner put forth by Parker and Mead (PaMe69). Consider the multistep tunneling process from metal to atom and then from atom to free space. The current flow from metal to atom is given by

$$j_{m-a} = \gamma_m(1-f)P_{m-a},$$

and from atom to vacuum by

$$j_{a-v} = \gamma_v f P_{a-v},$$

where $\gamma_{m(v)}$ are slowly varying functions of energy, f is the probability that an electron is in the atomic state during the tunneling process, P_{m-a} is the tunneling probability from metal to atom (essentially $\sim\exp-2ks$) and P_{a-v} is the tunneling probability from atom to vacuum [$\sim\exp-2k(s_T-s)$]. Conservation of charge requires $j_{m-a}=j_{a-v}$ which results in $f=\gamma_m P_{m-a}/(\gamma_m P_{m-a}+\gamma_v P_{a-v})$ and the current $j_a = j_{a-v} = j_{m-a} = \gamma_m\gamma_v P_{a-v}P_{m-a}/(\gamma_m P_{m-a}+\gamma_v P_{a-v})$. Without the atom, tunneling is via a one-step process in which $j_0 = \gamma_m P_{m-v}$ with $P_{m-v}\sim\exp-2ks_T$. The ratio is

$$j_a/j_0 = \gamma_v P_{m-a}P_{a-v}/(\gamma_m P_{m-a}+\gamma_v P_{a-v})P_{m-v} = |\langle f|H_T|a\rangle/\langle f|H_T|m\rangle|^2 \sim \exp(2ks) \quad (5.5)$$

when $s \ll s_T$ as it is in the field emission case. Furthermore, $2ks$ is $\simeq 2[(2m/\hbar^2)(\varphi_e-\epsilon)]^{1/2}s$ for the triangular barrier and presumably the same image force corrections and expansions given by Eqs. (2.14) can be used here. More detail could be put into this sort of calculation by explicitly choosing an operator H_T as the current density operator, the external field, or some other perturbation, and then doing a detailed calculation with atomic wave functions. The results would be similar to the d-band tunneling probabilities discussed in Sec. 3; that is, the ratio of resonance tunneling matrix elements from $(n-1)d$ states to ns states would be $\sim$0.1 due to the centrifugal barrier confinement. The virtue of the present approach is that we have arrived at the result of Eq. (5.5) without specifying the form of H_T or the wave functions. The only restriction has been that the impurity assists tunneling rather than backscattering electrons, a situation discussed by Hurrault (Hu71).

In the case of field emission, the quantity $T(\epsilon)$ is usually small relative to unity within the range $\epsilon \approx \epsilon_\varphi \pm \Delta_a$. Thus neglecting this interference term and combining Eqs. (5.4) and (5.5) yields the simple result that

$$\Delta j'/j_0' \simeq [\rho_a(\epsilon)/\rho_m(\epsilon)]\exp(+2ks), \quad (5.6)$$

essentially the result obtained by Gadzuk (Ga70). On the other hand, if the resonance level lies far from the energy region sampled in a TED, usually near the Fermi energy, then the interference term could be the dominate term in the enhancement factor. Under these circumstances, the sign of $\Delta j'$ could be either positive or negative depending upon the details of the particular system and thus an "antiresonance" behavior is possible (LeGo71). Thus from the straightforward physical model, the dominant features of resonance tunneling are obtainable. As will be seen, this type of result, with some added features, is obtained using the more detailed and quantitative approach to Penn *et al.* Connors has shown that similar behavior is to be expected in chemical physics when the potential energy barrier for a reactive collision contains a well or in nuclear physics

when the fission barrier for heavy nuclei possesses two two maxima (Con71).

Penn, Gomer, and Cohen (PeGoCo71, 72) begin their theory by adapting the generalized tunneling current expression of Appelbaum and Brinkman (ApBr69, 70) to a description of the field emission TED

$$j'(\epsilon)=[2f(\epsilon)/\hbar]\sum_{ii'f}\langle i'\mid\tau\mid f\rangle\langle f\mid\tau\mid i\rangle \times \mathrm{Im}\, G_{ii'}{}^{L}(\epsilon_f-i\delta)\delta(\epsilon-\epsilon_f), \quad (5.7)$$

where it is realized that the tunneling operator τ could give rise to emitted current resulting from off-diagonal terms in the Hamiltonian matrix. Consequently the sum on initial states is over both i and i'. Im $G_{ii'}{}^{L}$ is the imaginary part of the left-hand state Green's function. Final state energies are given by ϵ_f. The operator τ is $V_f{>}-eFs\mid a\rangle\langle a\mid$ with $V_f{>}=-eFz\theta(z)$. In the operator τ, the projection onto the adatom states shifts the zero of energy of the atom states due to the applied fields. By choosing the set of initial states $\{\mid i\rangle\}=\{\mid m\rangle,\mid a\rangle\}$, the manifold of metal and atom states, Eq. (5.7) is reduced to

$$j'(\epsilon)=j_0'(\epsilon)+[2f(\epsilon)/\hbar]\sum_f\delta(\epsilon-\epsilon_f) \times[(x^2-y^2)\ \mathrm{Im}\, G_{aa}(\epsilon_f)+2xy\ \mathrm{Re}\, G_{aa}(\epsilon_f)], \quad (5.8)$$

with $x=\langle f\mid\tau\mid a\rangle+\mathrm{Re}\,\sigma_f$,

$$y=\mathrm{Im}\,\sigma_f,$$

$$\sigma_f=\mathrm{Re}\,\sigma_f+i\ \mathrm{Im}\,\sigma_f =\sum_m[\langle f\mid V_f{>}\mid m\rangle/(\epsilon-\epsilon_m)]\langle m\mid V_{a-m}\mid a\rangle,$$

and $(\epsilon-\epsilon_m)^{-1}=P(\epsilon-\epsilon_m)^{-1}-i\pi\delta(\epsilon-\epsilon_m)$.

Here Re (Im)$G_{aa}(\epsilon)$ is the real (imaginary) part of the adatom Green's function. The new feature which this formalism emphasizes is some additional "interference" tunneling resulting from σ_f. This allows for processes in which an electron originally in the atom tunnels back to the metal due to the V_{a-m} coupling, propagates in the metal, and then tunnels directly to the vacuum through the eFz interaction. This is neglected in Eq. (5.4) when taking $\mid a'\rangle\approx\mid a\rangle$. For the same reasons that the $T(\epsilon)$ term in Eq. (5.4) was argued to be small, Penn *et al.* recognize that σ_f and, consequently, y are small in Eq. (5.8). This leads to the simple result

$$\Delta j'(\epsilon)/j_0'(\epsilon)\simeq u'^2\ \mathrm{Im}\, G_{aa}(\epsilon), \quad (5.9)$$

with

$$u'^2\simeq\lambda\exp\left(2\xi(\epsilon)s+\{(4/3eF)(\hbar^2/2m)\xi^3(\epsilon) \times[v(y)-1]\}\right),$$

$$\xi(\epsilon)=[(2m/\hbar^2)(\varphi_e-\epsilon)]^{1/2}$$

with $v(y)$ the tabulated function in Table I, and λ= slowly varying pre-exponential functions of ϵ. In Eq. (5.9), Penn *et al.* have included the image potential modification to the barrier. In fact they suggest that in order to obtain quantitative agreement between theory and experiment, the image potential reduction of the tunneling barrier is crucial. Finally note that in spite of the seemingly different approaches to the problem of resonance tunneling, after the second-order terms are neglected, the structure of the simple theory result, Eq. (5.6) bears a striking resemblance to the more formal theory result, Eq. (5.9) when image potential affects are neglected.

Still another formalism for treating field emission resonance tunneling has been devised in an extensive set of papers by Modinos and co-workers (MoNi69, 71; Mo70,a; MoTh71; NiMo71). They approach the problem from a two potential scattering theory point of view in which the forbidden barrier containing adatoms is described by a potential of the form

$$V(\mathbf{r})=U(z)+\sum_\alpha v_\alpha(\mathbf{r}-\mathbf{R}_\alpha),$$

with $U(z)$ the slowly varying surface potential plus applied field and v_α the atomic potential of the αth adatom situated at position $\mathbf{R}_\alpha$. It is assumed that the "first-stage scattering" by $U(z)$ of electrons incident upon the barrier from within the metal is treated to all orders in scattering. In practice this part of the problem is dealt with by using WKB wave functions for the electron in the barrier when $v_\alpha=0$. The adatoms scatter (possibly resonantly) the tunneling electrons, thus modifying the transmission amplitude

$$A_{\mathbf{k}}=A_0+\int\chi_{\mathbf{k}}^{(-)*}(\mathbf{r})t(\mathbf{r},\mathbf{r}')\chi_{\mathbf{k}}^{(+)}(\mathbf{r}')\,d^3r\,d^3r', \quad (5.10)$$

with A_0 the amplitude without atoms, $\chi_{\mathbf{k}}{}^{+(-)}$ the solution of the $v_\alpha=0$ Hamiltonian representing an outgoing (ingoing) wave with respect to the metal, and $t(\mathbf{r},\mathbf{r}')$ the exact T matrix for scattering from a single atom which is expanded as

$$t(\mathbf{r},\mathbf{r}')=v(\mathbf{r})\delta^{(3)}(\mathbf{r}-\mathbf{r}') +v(\mathbf{r})g(\mathbf{r},\mathbf{r}')v(\mathbf{r}')+\cdots. \quad (5.11)$$

In Eq. (5.11), the first term is simple potential scattering whereas the second term allows for scattering at $\mathbf{r}'$ followed by intermediate state propagation from $\mathbf{r}'$ to $\mathbf{r}$ and then scattering again at $\mathbf{r}$. If the energy of the incident electrons falls near the energy of a virtual adatom level, characterized by wave functions $\psi_a(\mathbf{r})$, Modinos *et al.* note that the intermediate state Green's function can be taken to be

$$g(\mathbf{r},\mathbf{r}')\simeq\psi_a(\mathbf{r})\psi_a{}^*(\mathbf{r}')/(\epsilon-\epsilon_\varphi+i\Delta_a) \quad (5.12)$$

similar to the mixing term in the Fano wave function of Eq. (5.1). Inserting Eqs. (5.11) and (5.12) into (5.10) and then evaluating $\mid t_{\mathbf{k}}\mid^2\alpha j'(\epsilon=\epsilon_{\mathbf{k}})$, we see that the structure of the end result is again similar to the results of the previously mentioned approaches, namely a direct and a resonance term plus an interference term between alternate channels. Furthermore the resonance term is proportional to a Lorentzian characterized by

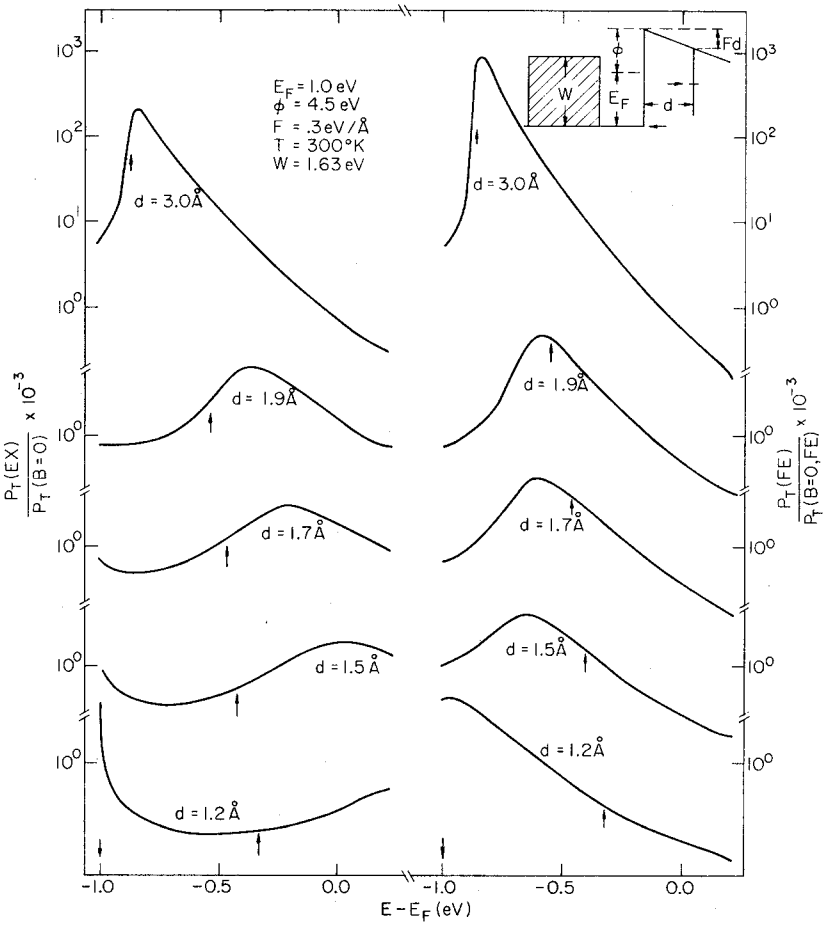

FIG. 33. Comparison of the exact (left) and the free-electron (right) adsorbate enhancement factors, for a variety of adsorbate–surface distances d. The model parameters are indicated in the figure. The arrows pointing up indicate the bound-state energies of the adsorbate, while those pointing down indicate the bottom of the band. Note the shift of the resonant peak from the arrow indicating that the bound-state energy is in the opposite direction in the free-electron enhancements than in the exact ones. (DuF72.)

the adatom level position and width. The additional feature of the Modinos model is that it more easily allows for three dimensional effects. In fact they find that when the adatom coverage becomes sufficiently high, significant interaction between adatoms occurs and the two-dimensional bands formed by the adatom layer become so wide that resonance structure is hard to see in a TED.

Duke and Fauchier (DuFa72) have calculated the TED for a Kronig–Penney solid with chemisorbed atoms described by point delta function potentials. By using the wave-matching technique which Duke and Alferieff (DuAl67) invoked in the first demonstration of field emission resonance tunneling, the TED and thus the enhancement factor can be exactly solved for their chosen model. Duke and Fauchier examined the affects of systematic variations of the relevant parameters characterising the total systems. In particular, special emphasis was given to the atom–metal separation (a measure of the coupling strength between the two components) and to the width of the metal conduction band (a measure of the localization or atomic-like behavior of the band states). In Fig. 33, their calculated enhancement factors are drawn for an extremely narrow band, treating the atom–metal separation (d in their notation) parametrically. The left-hand panel corresponds to a Kronig–Penney metal, whereas the right-hand panel corresponds to a free-electron metal. The bound state energy (E_B in their notation) of the delta function atom is marked by the arrow. Note the shift in E_B caused by the field; i.e., that $\Delta E_B = -eFd$. The features of these curves which Duke and Fauchier emphasize are that the peak in the enhancement factor does not fall at the same energy as E_B. Furthermore, the enhancement maximum lies lower in energy than E_B for a free-electron metal, whereas it can lie above E_B for a narrow band metal with a lattice, at least for their particular choice of parameters. Figure 34 shows the systematic variation of the enhancement factor as the band width in the Kronig–Penney metal varies. Note that the maximum moves from below E_B for wide bands to a double-humped structure with the resonance maximum above E_B for a narrow band.

These results are consistent with present understanding of both field emission resonance tunneling and chemisorption. First consider the free-electron results. As previously noted [Eq. (5.6)], the free-electron enhancement is basically a Lorentzian skewed

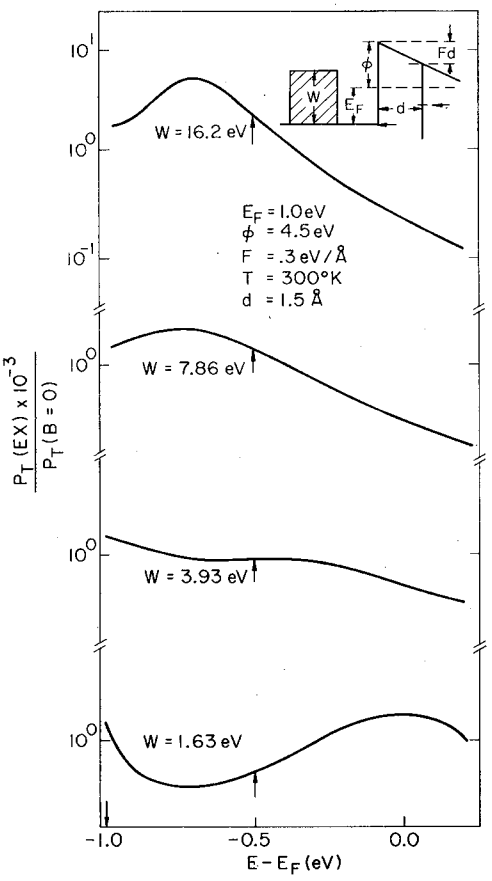

FIG. 34. Typical adsorbate enhancement factors for four values of the bandwidth W. (DuF72.)

by an exponential function of energy which increases with decreasing energy. This feature pushes the maximum of the enhancement below the maximum of the Lorentzian. As d decreases, the atom–metal interaction increases and the Lorentzian width thus increases. This increased broadening reduces the structure in the enhancement. Thus the previous theories discussed in this chapter predict the same qualitative behavior as given by the calculations of Duke and Fauchier shown in Fig. 33. Now consider the Kronig–Penney narrow band. For simplicity, assume that the atomic state interacts with all the occupied states distributed in energy between O and E_F as if they all possessed some average energy $\bar{E} \sim E_F/2$. In the narrow-band limit, it is now customary practice to treat chemisorption from a surface molecule point of view (Gr71, Sc72) in which a molecule is formed between the adatom and the substrate atoms upon which it sits. The molecular complex then interacts weakly with the indented solid. The wave functions of the Kronig–Penney narrow-band solid and the delta function atom before interacting are shown in the top panel of Fig. 35. Note that the narrow-band character is reflected in the degree of localization of the "atomic" part of the Bloch function. For narrow bands, the amplitude is small between lattice planes and it is this property which causes the reduced tunneling probability in narrow band solids when viewed from an atomic-like framework. The free-electron wave function envelope is shown as a dashed curve. From a molecular orbital point of view, the interaction between the localized functions on the last substrate atom and on the adatom results in new eigenvalues for the complex as shown in the second panel of Fig. 35. If $\bar{E} < E_B$, the low-energy binding orbital is mostly of substrate character, shown as the solid curve in the bottom panel, whereas the high-energy antibonding orbital is mostly of adatom character. It is this state, with energy E_R, which would be responsible for the resonance peak in the enhancement factor. Note that $E_R > E_B$, as predicted

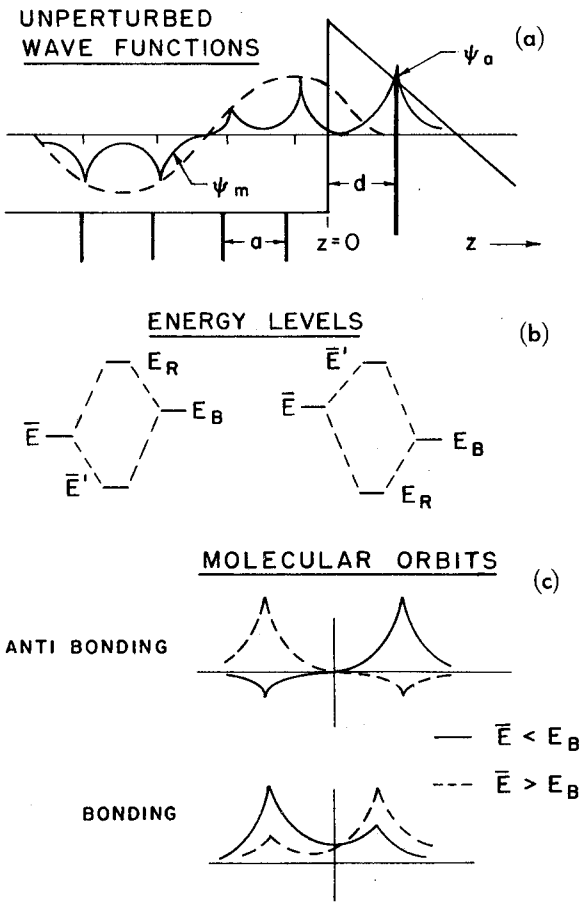

FIG. 35. (a) Potentials for Kronig–Penney solid with an adsorbed atom represented by a delta function potential, under the influence of an applied field. Also shown are Ψ_m, the unperturbed metal wavefunction, Ψ_a, the unperturbed adatom wave function, and the free-electron metal wave function (dashed line). The lattice constant is a and the atom–metal separation is d. (b) Molecular orbital energy level spectrum formed from a metal tight-binding band centered at energy $\bar{E}$ and an adatom level at E_B. The resonance tunneling maximum appears at E_R. (c) Molecular orbital wave functions formed under the conditions stated in (b). The resonance tunneling maximum results from tunneling from the orbital with maximum charge density centered on the adatom.

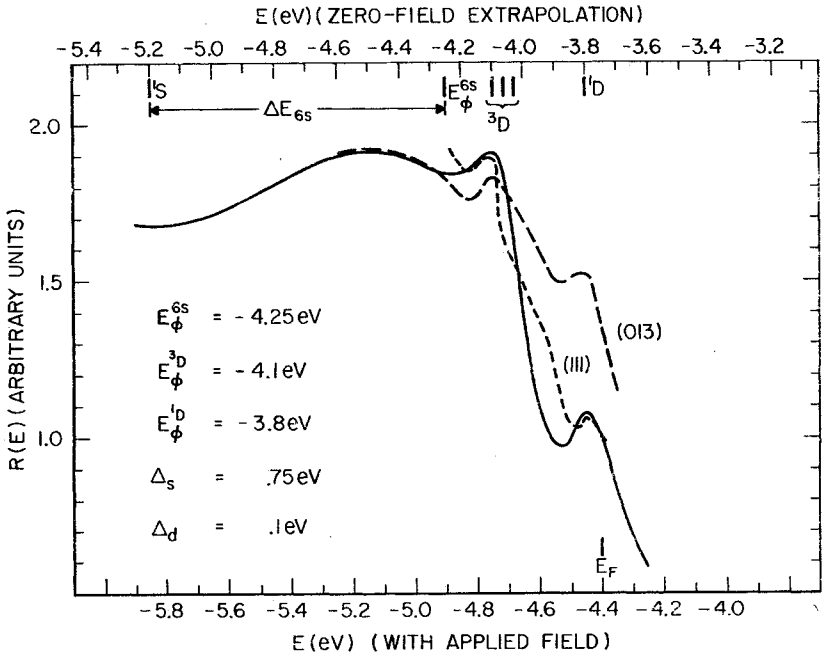

FIG. 36. Calculated (solid) and experimentally obtained (dashed) values of the enhancement factor and thus skewed virtual-energy-level spectrum for Ba on (111) and (013) W. The magnitude of R is left arbitrary. The scale on the bottom is that of the experiment. The scale on the top is that one resulting from an extrapolation to the zero field limit. Note the positions of the unperturbed atomic levels and the relative shift of the $6s$ state. (Ga70.)

by Duke and Fauchier. The difference $E_R - E_B$ varies as the strength of the atom–metal coupling. From Duke and Fauchier's point of view, as d decreases (implying a stronger interaction), E_R increases relative to E_B. This is seen in their results on the left-hand panel of Fig. 33. Furthermore, as d decreases the orbital level width increases and this broadens the resonance structure. A similar situation prevails when $\bar{E} > E_B$ except that $E_R < E_B$.

The trends shown in Fig. 34 in which E_R moves from below E_B to above it as the bandwidth decreases illustrate the continuous transition in the character of the enhancement curve as the nature of the conduction band goes from nearly free electron like ($W = 16.2$ eV) to atomic-like ($W = 1.63$ eV). It should also be pointed out that these results are quite consistent with the resonance tunneling results of the previously mentioned theories although these theories were not applied to specific cases in which the solid was treated in the narrow-band limit. Consider the system wave function given by Eq. (5.1). For a narrow-band solid, $|m\rangle$ would be made up of localized functions centered on each substrate lattice site. In addition, $\Delta\epsilon$ would contain a large term due to the interaction between the localized function $|m\rangle$ and the adatom wave function ($\Delta\epsilon \sim P\int d\epsilon_m [|\langle a|V_{a-m}|m\rangle|^2/(\epsilon-\epsilon_m)]$ in the Anderson model). In the extreme molecular limit, the Anderson model gives two eigenvalues (with ϵ_m replaced by $\bar{\epsilon}$)

$$\epsilon_\pm = \tfrac{1}{2}(\bar{\epsilon}+\epsilon_a) \pm [|\langle a|V_{am}|m\rangle|^2 + 4(\bar{\epsilon}-\epsilon_a)]^{1/2},$$

in agreement with the molecular theory just discussed. The shift in ϵ_a would cause ϵ_φ [in (Eq. 5.1)] or E_R in the Duke and Fauchier notation to have exactly the same behavior that as illustrated in Fig. 33.

5.2a. Alkaline Earths

The first major experimental verification of field emission resonance tunneling came in the alkaline earth studies of Plummer and Young (PY70) using the retarding potential analyzer shown in Fig. 13(b). TED measurements with a Ba atom on W revealed several pieces of structure in the enhancement curve which were interpreted in terms of the gas-phase excitation spectrum of Ba. Using a formula similar to Eq. (5.4) suitably adapted for the electron levels of Ba, a Ba enhancement curve was theoretically determined. Both experimental and theoretical curves are shown in Fig. 36. The broad structure at ~ -4.5 eV is a manifestation of the $6s^2$ ground state of a Ba atom perturbed and broadened by its interaction with the substrate. The two narrow structures at ~ -4.1 and ~ -3.8 eV are interpreted to be the first two excited $6s5d$ states of Ba achieved by "promoting" a $6s$ electron into a geometrically more confining $5d$ orbital. The width of the $6s5d$ states relative to the $6s^2$ is $\sim 1/8$ for the same reasons that the width of the $5d$ bands in Au are about 10–15% of the widths of the $6s$ band, namely the confinement by the centrifugal barrier. Similar results were obtained with Ca adsorption. Thus a spectroscopy of the adatom density of states which is characterized by the level width and position was truly possible. The general findings seemed to indicate that ns levels take on a natural width ~ 1 eV whereas the corresponding $(n-1)$ d levels are down by an order of magnitude.

In this study of barium on different faces of tungsten it appeared that the levels of barium on the surfaces shifted from one face to the next as one would expect from only a work function change (PY70). As the

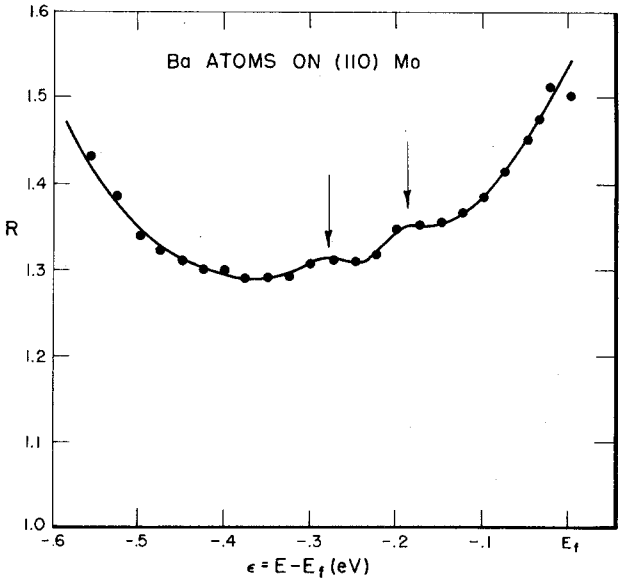

FIG. 37. Enhancement factor curve for single barium atoms on (110) Mo. The enhancement factor R in this curve is an average of nearly ten independent curves and is calculated by dividing the energy distribution after adsorption by the energy distribution before adsorption. (PY70.)

work function increased, more of the structure shown in Fig. 36 disappeared above the Fermi energy. If the observed levels did not depend on the details of the electron properties of each crystal face of one metal, would they vary if the work function was constant but the metal changed? Figure 37 shows the enhancement curves for single barium atoms on the (110) plane of molybdenum. The work function of the (110) plane of molybdenum is ~5.00 eV, nearly equal to (110) tungsten. It is quite obvious that the R curves are not the same; in fact there now seems to be two sharp peaks separated by approximately 0.1 eV instead of 0.3 eV as in the case of barium on tungsten (PY70). The adsorption depends on the substrate. The two peaks which appeared in adsorption on tungsten separated by 0.3 eV are not present. This could mean that the interpretation of the barium on tungsten curves (Ga70, PY70) is incorrect or that there is structure in the clean (110) Mo curve which is not present on the tungsten (110) plane. These R curves were obtained by dividing the TED from the surface with adsorbed atoms by the clean surface TED. As pointed out in Sec. 4, this can be misleading because of surface sensitive structure in the clean energy distributions. There is also a possibility that the fine structure in both cases is due to inelastic tunneling, a subject covered in Sec. 5.3.

5.2b. Hydrogen on (100) Tungsten

Hydrogen is the simplest chemisorbed species. For this reason the chemisorption of hydrogen on the cube face of tungsten is an extremely well-studied system. The experimental measurements on this system seem to be very reproducible, but unfortunately they do not portray a consistent picture of the hydrogen–tungsten bond. For example, the basic question of whether an observed binding state is atomic or molecular has not been definitely resolved. It is even debatable whether multiple peaks in a flash desorption spectrum indicate multiple binding states upon adsorption or reflect some other mechanism inherent in the flash-off, such as a density-dependent phase transition. This is the type of problem that can be solved using the spectroscopic information produced from the field emission energy distribution. A detailed study of energy distributions or specifically of the enhancement factor $R(E)$, as a function of hydrogen or deuterium coverage on the (100) plane of tungsten has been performed (PBe72) utilizing the spherical deflector analyzer (KP72) described in Sec. 3.

Figure 38 displays the enhancement factor $R(E)$ calculated from the measured energy distributions for deuterium and hydrogen on (100) tungsten at 300 K as a function of the density of adsorbed atoms. The characteristic low-energy electron diffraction patterns observed by others are indicated along the density axis (EAn66, AdGe70, YSc71). The free-electron energy distributions $j_0'(\epsilon, \varphi_e, F)$ were calculated from the data using an initial work function of 4.64 eV for the (100) plane and determining the change in work function ($\Delta\varphi$) from the slope of the Fowler–Nordheim plots (PBe72). The density of atoms was obtained using Madey and Yates' (MaYa70) work function vs coverage data and Tamm and Schmidt's (TaSc69, 70) absolute coverage.

The β_2 state saturates at $\sim 5\times10^{14}$ atoms/cm^2 and the β_1 state at $\sim 15\times10^{14}$ atoms/cm^2 (EAn66; TaSc69, 70; AdGe70; MaYa70; YSc71). It is clear from Fig. 39 that the energy distribution characteristic of β_2 develops with density n from $0<n<\sim 5\times10^{14}$ atoms/cm^2, while the structure characteristic of the clean surface disappears with coverage [see Sec. 4.1]. The spectrum near $n\sim 5\times10^{14}$ atoms/cm^2 is a nearly ideal example of resonance tunneling [Eq. (5.4)] through a level positioned 0.9 eV below the Fermi energy or 5.54 eV below the vacuum. The full width at half-maximum is approximately 0.6 eV. There are additional features in the enhancement curve for the β_2 state. There is a gradual increase in the curve with decreasing energy. This is just the energy-dependent background previously discussed [Eq. (5.4)]. Also there is a shoulder approximately 1.1 eV below the Fermi energy. This structure could originate from another state, indicating that the energy level in the β_2 is a composite of two levels. In light of the calculations of Newns (Ne69) for hydrogen adsorption and the formalism espoused by Grimley (Gr71), it is tempting to interpret this level as indicating that hydrogen is adsorbed in a nonmagnetic state; that is, that the ground state and affinity level come together to form a single, doubly-occupied state. This interpretation must be considered premature at

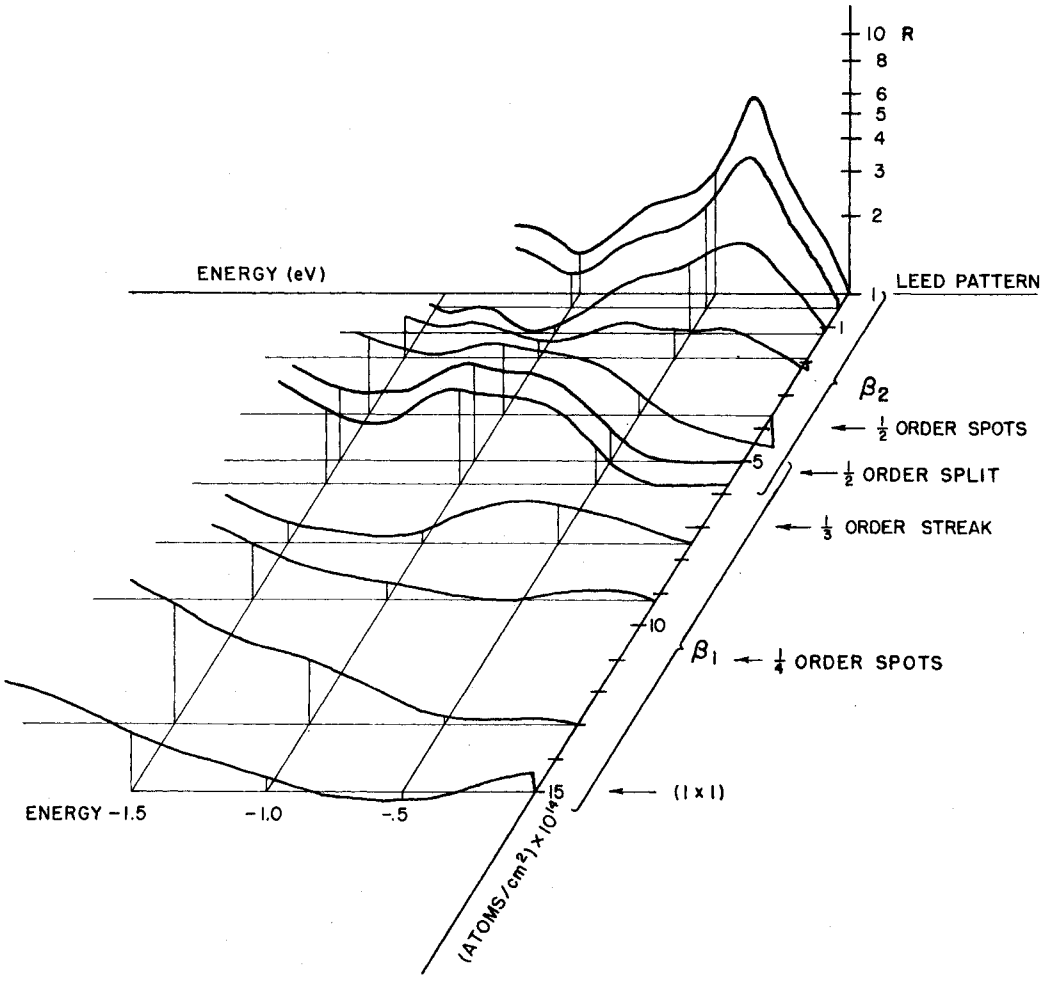

FIG. 38. Enhancement factor $R(\epsilon)$ for hydrogen and deuterium on (100) W at 300 K as a function of the atom density on the surface. The corresponding binding states (β_1 and β_2) and LEED patterns are indicated on the density axis. There are 10^{15} atoms/cm^2 of tungsten in the (100) plane. (PBe72.)

present for several reasons: (1) A doubly-occupied level at this position would require hydrogen existing on the surface as a negative ion; (2) There could be additional structure at lower energies that we cannot see; (3) The level width is narrower than one would expect; and (4) There is hydrogen–hydrogen interaction.

As the coverage increases beyond 5×10^{14} atoms/cm^2 the LEED 1/2 order spots characteristic of the β_2 state begin to split; eventually 1/3 order streaks and 1/4 order spots appear before the β_1 state is saturated at 15×10^{14} atoms/cm^2 and a simple (1×1) structure results. The relative position of these events have been indicated in Fig. 38. The energy distribution characteristic of the β_2 state shifts and converts to the energy level spectrum characteristic of the β_1 state. These distributions indicate that the β_2 does not exist on the surface in the presence of the β_1 in the same electronic configuration as it has when the coverage is low. These observations would indicate that the multiple peaks in the flash desorption spectrum originate from a density-dependent interaction, specifically a sharp transition near $5\text{–}6\times10^{14}$ atoms/cm^2. We will discuss the problem of atomic or molecular adsorption in the section on inelastic tunneling (Sec. 5.3).

5.2c. Oxygen on Tungsten

The chemisorption of oxygen is much more complicated than hydrogen adsorption on tungsten. In both systems rapid adsorption occurs up to near monolayer coverage. There hydrogen adsorption seems to stop while the rapid absorption of oxygen is followed by a slow, apparently activated adsorption. Since tungsten oxidizes it is apparent that at some coverage and temperature the surface must rearrange or "reconstruct."

The energy distribution of hydrogen on (100) tungsten at a given temperature depends solely upon

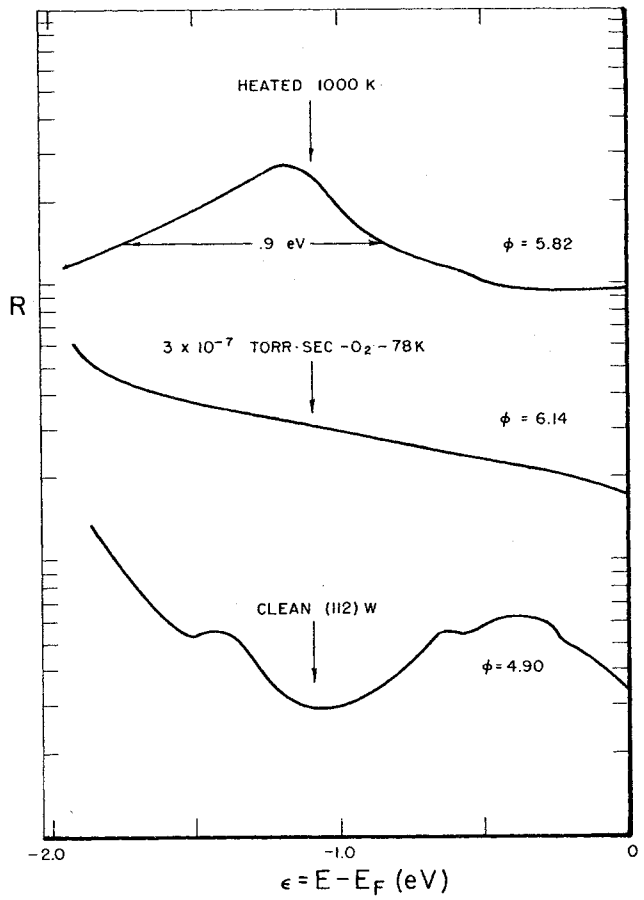

FIG. 39. Enhancement factor curves R for clean (112) W; 3×10^{-7} Torr•sec exposure of oxygen at 78 K; and after the surface had been heated to ~1000 K. Heating to near 300 K produced the same result.

the density of adatoms, at least for temperatures down to 78 K and most likely to much lower temperatures. All that changes upon adsorption is the sticking coefficient. In contrast, oxygen adsorption at 78 K produces a considerably different energy distribution than adsorption at room temperature, at least for the (110), (112), and (111) planes. So the enhancement factor curves as a function of coverage would look considerably different at 78 K than at 300 K. Figures 15 and 17 have already shown what the enhancement curves $R(\epsilon)$ look like for clean (112) tungsten and with 3×10^{-7} Torr•sec oxygen exposure at 78 K. Figure 39 shows what happens when the substrate is warmed to greater than 200–300 K for 30 sec (P71). In this figure the sample was heated to 1000 K but 300 K is sufficient to produce this irreversible change.

The low-energy electron diffraction data show that oxygen is ordered on the (112) plane at room temperature (TrBl69, AdGeMa70), and may be disordered at 78 K (Mc71). This irreversible change on heating to room temperature could be just a disorder–order transition of the adsorbate. The activation energy for diffusion might be too large for ordering to occur at 78 K (EnGo70) but the same kind of irreversible transition occurs on the (111) plane slightly below room temperature. Figure 40 shows the measured total energy distributions for clean (111) tungsten and for the same face treated with an activation exposure of oxygen at 78 K and also above 200 K (KP72). There is no evidence that the (111) surface orders with oxygen exposure (Ta64), and there does not appear to be any long-range order. This might indicate that the transition we see is the adsorbate to surface molecule; i.e. surface reconstruction, which would not necessarily produce ordered low-energy electron diffraction patterns.

We also have included the enhancement curves as a function of exposure from 2×10^{-8} Torr•sec to 3×10^{-4} Torr•sec of oxygen on the (112) plane of tungsten at room temperature (P71) [Fig. 41(a), (b)]. The point here is that changes still occur after monolayer coverage (~5×10^{-6} Torr•sec). Figure 41(a) shows the submonolayer region where one characteristic peak approximately 1.2 eV below the Fermi energy builds in with coverage up to about 1×10^{-6} Torr•sec exposure. Above this, two peaks start to build in closer to the Fermi energy. A more detailed study must be made to relate these structures to the LEED patterns and the two peaks observed in the flash desorption spectrum (TrBl69). The peak at -1.2 eV saturates at about the correct work function to be related to the $P(2\times1)$ structure and the first adsorption state.

Above 1×10^{-6} Torr•sec exposure of oxygen [Fig. 41(b)] the enhancement curves change gradually until at $>10^{-4}$ Torr•sec there does not appear to be much structure at all. If the substrate is warmed to ~1600 K for 30 sec the enhancement factor curve R reverts to one resembling a high 10^{-6} Torr•sec exposure (see Fig. 42). Finally, if the sample is heated to ~2000 K the energy distribution returns to that of the submonolayer oxygen coverage (Fig. 42). These observations can tentatively be said to agree with the mass spectrometry flash desorption data of King, Madey, and Yates (KMaYa71) on polycrystalline tungsten. They show that for exposures above 10^{-5} Torr•sec, tungsten oxides with flash desorption temperatures below 1600 K are adsorbed. Starting at about ~5×10^{-6} Torr•sec, more tightly bound (1700 K) oxides are formed. A much more detailed study of oxygen needs to be undertaken, but these curves serve to illustrate the possibilities.

5.2d. Krypton

Lea and Gomer performed a series of energy distribution measurements from surfaces in which krypton was adsorbed on the W(100), (110), (111), and (112) planes using the analyzer shown in Fig. 13(d) (LeGo71). Krypton was chosen since in the gas phase it possesses excited states at an energy near the Fermi level of W. Since the perturbation H_T can mix all the

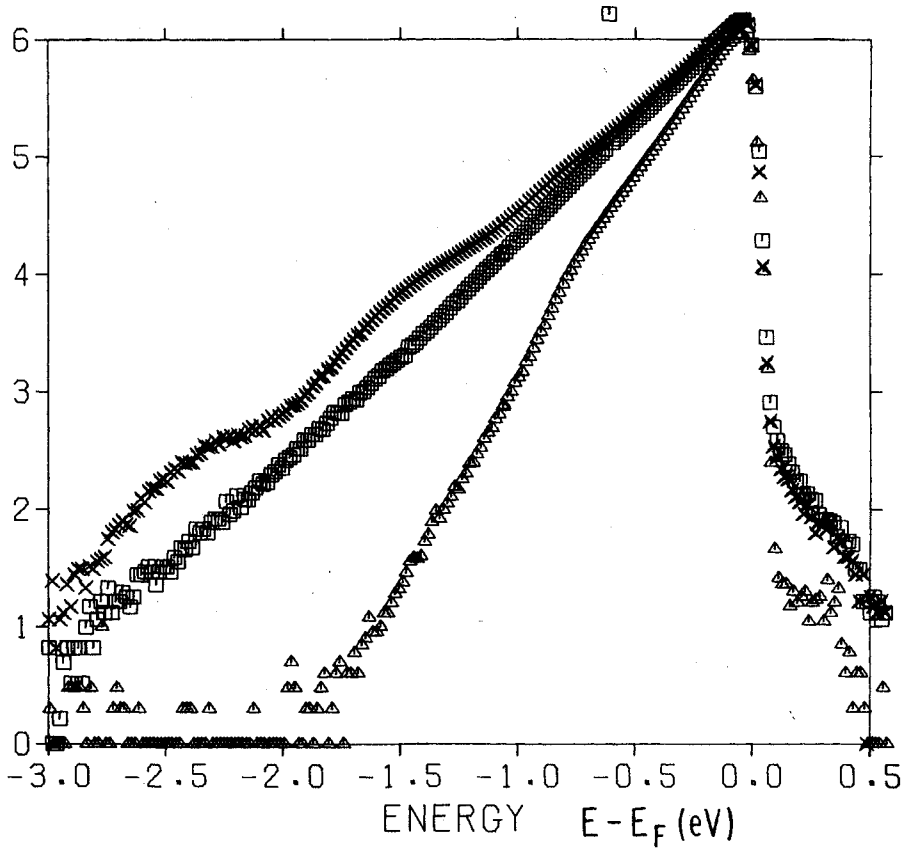

FIG. 40. Total energy distribution from (111) W at 78 K. The first energy distribution [△] is for clean (111) W; the second [□] is after saturation exposure of oxygen at 78 K and the third [×] is after heating to 250 K for 120 sec.

states of the atom, the ground state of the adsorbed atom might have structure in its density of state and thus in the enhancement factor which is near the excited state energies. The experiments of Lea and Gomer, in which partial monolayers as well as multilayers of Kr were adsorbed, revealed no pronounced structure in the TED. In most cases it was found that all changes in emission characteristics, both FN and TED curves, could be interpreted in terms of field-induced work function decreases. It was found that Kr adsorption on the (100) plane reduced emission from the Swanson hump discussed in Sec. 4.2c, further confirming the notion that the structure is due to surface states. Finally the role of "antiresonances" for Kr on (110) W was noted. As pointed out by D–A (DuAl67) and discussed earlier in this section, adsorbates can hinder as well as aid tunneling. In some cases in which energy levels lie above or far below the Fermi energy, the interference term [the second term in brackets in Eq. (5.4)] can dominate and the sign of $\Delta j'$ could be negative corresponding to an antiresonance. Similar behavior is observed in asymmetric line shapes in atomic resonance phenomenon (Fa61). Lea and Gomer observed strong decreases in the pre-exponential term in the TED which they feel could not be accounted for by depolarization effects or work function increases. They thus suggest that an antiresonance effect may be the cause of the decrease.

5.2e. Germanium on W

Some of the earliest work on electron energy distributions in field emission was the Ge on W studies of Sokolskaya and Mileshkina (SoMi61, 63, 64, 64a, 66). The general characteristics they observed were the following. Upon adsorbing <1 layer of Ge on the surface, the total field emission current was reduced by a factor of $\sim$30–40 (implying an increase in φ_e), the slope of the FN remained constant (implying constant φ_e), and additional peaks in the TED appeared as the dosage of Ge was increased. With these characteristics, the system Ge on W is a good candidate for elastic resonance tunneling (Do67).

In a more recent extensive study of this system, Clark has confirmed many of the MS results by depositing single Ge atoms and increasing the deposition to several layers (Cl71). His results are described quite well by the theoretical model due to Nicolaou and Modinos

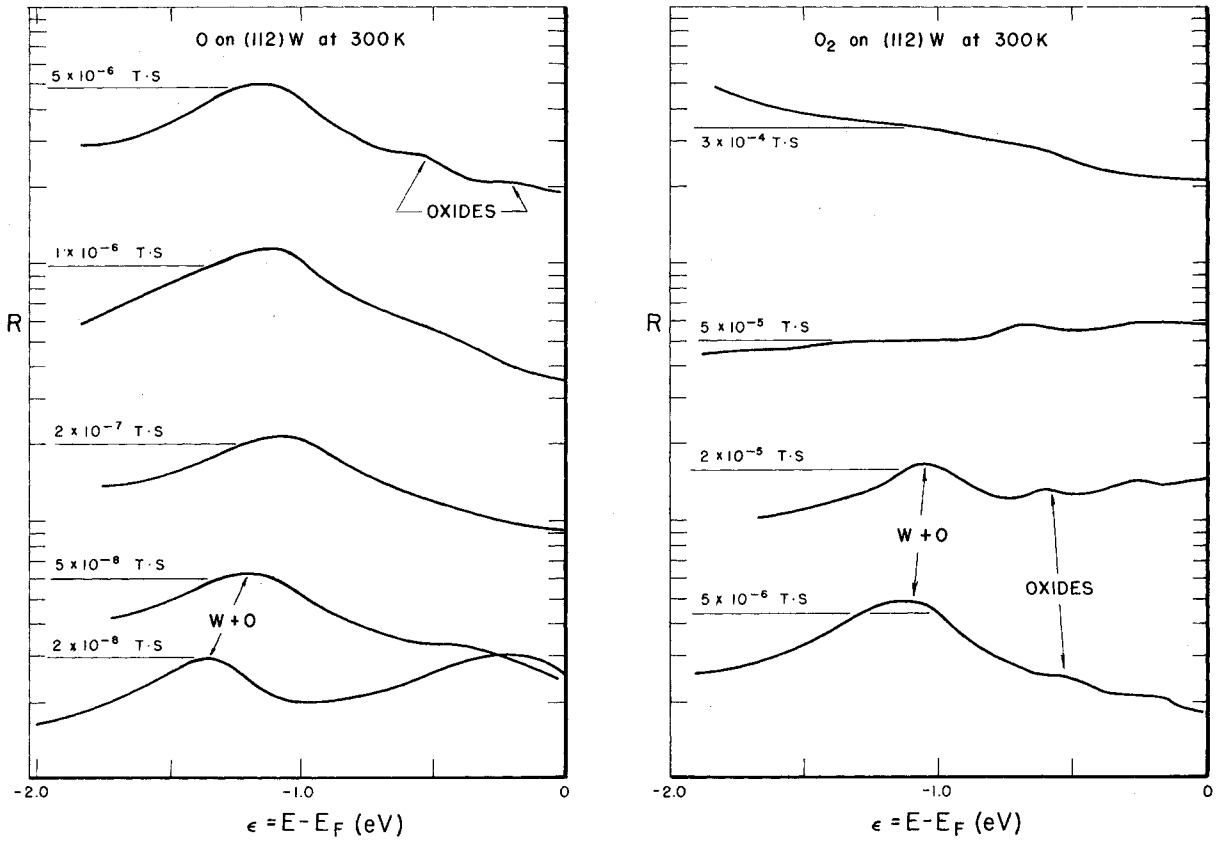

FIG. 41. Enhancement factor curves $R(\epsilon)$ for (112) W at 300 K for various exposures of oxygen. The multiplicative constant for each curve is arbitrary.

(NiMo71) in which resonance tunneling is the mechanism for changes in emission. A summary of Clark's results is shown in Fig. 43 for various coverages θ in the range $0 \lesssim \theta \lesssim 2$. Energy distributions taken with the retarding analyzer in Fig. 13(b) are shown in the top section. As depicted, additional structure does not appear until deposition is well into the second layer. Throughout first-layer formation, the pre-exponential in the FN equation increases but the work function increases more strongly and an overall decrease in current is observed. Not until the second layer forms does Ge deposition enhance the emission.

These results have been interpreted by Clark in the following way: As the first layer is deposited, the $4s^24p^2\,{}^1S$ ground state of Ge becomes so broad due to its interaction with the W substrate that the level is not distinguishable in the TED. Furthermore, the Ge layer possesses an overall negative charge so the work function increases. For second-layer formation, the Ge is further from the W so the Ge–W interaction (much stronger than Ge–Ge interactions) is reduced and the linewidth of the $4p5s$ derived state is much narrower and appears as structure in the $\theta = 2$ TED in Fig. 43. Clark noted that the first layer is characterized by a broad ($\Delta_{\text{FWHM}} \sim 1$ eV) level centered ~ 1.6 eV below the Fermi energy. Not until the second layer is formed does one see evidence for a narrow (Δ FWHM$\sim$0.4 eV) level centered ~ 0.5 eV below the Fermi energy. This level is interpreted to be evidence for the $5s$ first excited state of Ge, somewhat analogous to the $6s5d$ states seen in the Ba on W experiment (Ga70, PY70). The broad $4s^24p^2$ level is the rudimentary valence band whereas the $4p5s$ configuration is probably the first stage of conduction band formation.

5.3. Inelastic Tunneling

The importance of impurity assisted inelastic tunneling has been demonstrated in the junction tunneling experiments of Lambe and Jaklevic (JLa66, LaJ68). L–J deposited various molecules such as H_2O, CO, and C_2H_2 at one interface of a metal–insulator–metal junction. Measurements of the current–voltage characteristics (I–V) revealed sharp line structure in the second derivative curves (d^2I/dV^2). The voltage at which this structure appeared was quite close to the energies of the infrared active vibrational modes of the molecules or hydroxyl groups. Based upon the L–J results and suggestions, Scalapino and Marcus developed a simple theory to explain these structures in terms of inelastic tunneling (ScMa67) in which the

tunneling electron excites a vibrational mode of the molecule. With these experiments and theory, a new form of infrared-like spectroscopy was possible.

The corresponding inelastic processes are also possible in a field emission situation. In fact, Flood (Fl69, 70) presented an adaptation of the Scalapino and Marcus theory to the field emission configuration. As will be shown, the principal result states that if a localized vibrational mode of energy $\hbar\omega_p$ exists in a molecule adsorbed on the emitter surface, then the resulting TED could be qualitatively expressed as

$$j_{\text{in}}'(\epsilon)=j'(\epsilon)+\sum_{n,p} j'(\epsilon+n\hbar\omega_p)f(\epsilon+n\hbar\omega_p)T_{\text{in}}^{(p)}, \quad (5.13)$$

with j' the standard TED given by Eq. (2.18), $T_{\text{in}}^{(p)}\sim|\Lambda^{(\text{inel})}(p)|^2$ the inelastic tunneling vertex similar to Eq. (2.25), and the sum performed over all modes p and multiples n of these modes. This simple result says that replicas of the elastic TED will appear displaced downwards in energy by $n\hbar\omega_p$. The relative strength of the inelastic to elastic TED is governed by the electron–phonon coupling which is proportional to the dipole matrix element of the localized vibrator. When this ratio is $\sim 1\%$ as in the case of the L–J experiments and the Plummer–Bell (PBe72) field emission results then some means for extracting the small inelastic signal such as second derivative or computer processing of data is required. On the other hand, in the case of the organic molecules studied by Swanson and Crouser (SwCr70), the relative strength of inelastic to elastic channels is of order unity or more (which does not exclude 1% peaks not reported) so the results are much more dramatic.

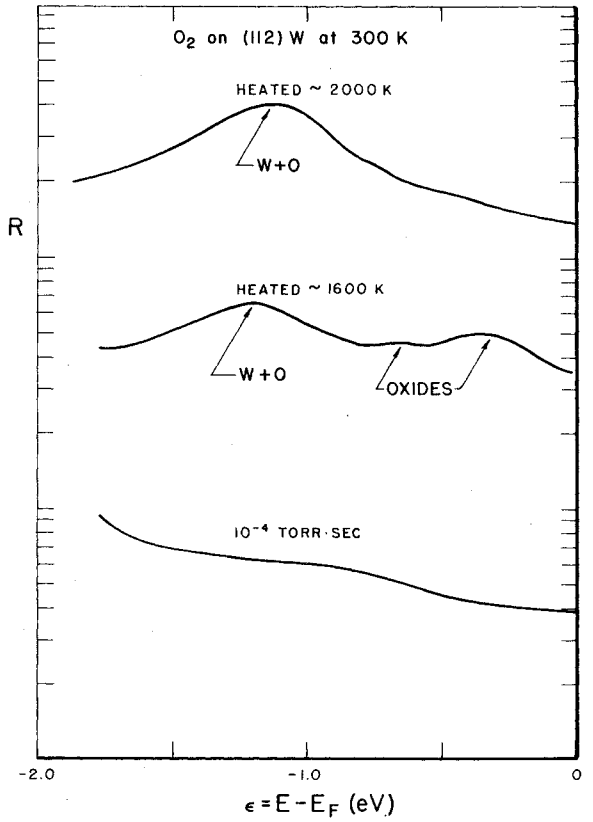

FIG. 42. Enhancement factor curve $R(\epsilon)$ for oxygen covered (112) tungsten at 300 K. The lower curve is after 10^{-4} Torr·sec exposure of oxygen at 300 K. The middle curve is after a 30 sec heat to 1600 K. The top curve is after 30 sec at 2000 K.

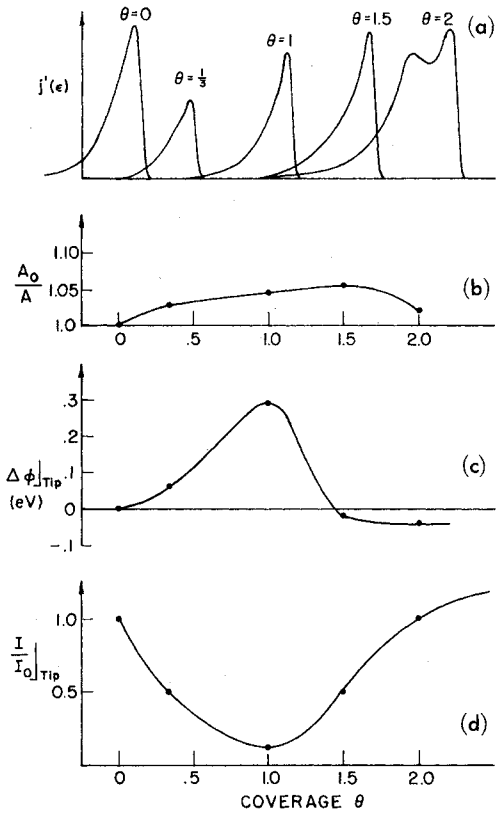

FIG. 43. Summary of the Ge on W studies (Cl71). (a) TED's for various coverages (θ). (b) FN pre-exponential vs θ. (c) Change of work function vs θ. (d) Normalized probe hole current vs θ.

The Flood treatment of inelastic field emission starts by assuming a dipole interaction potential between the tunneling electron and the localized vibrator which is

$$V_d(\mathbf{r})=-\mu_z z/(z^2+r_T^2)^{3/2}, \quad (5.14)$$

with μ_z the component of the dipole moment of the vibrator normal to the surface and r_T the transverse position of the electron. A good deal of effort is then expended to include the interaction term V_d in the WKB phase integral of Eq. (2.11). If we call $\bar{\varphi}_m\equiv\langle\varphi_e+E_F-e^2/4z-eFz-W\rangle$ (the average value in the barrier) and perform the usual tunneling expansions discussed in Sec. 2, the phase integral is

$$A(W)=a\int_{z_1}^{z_2(\hbar\omega_p)}\left\{\frac{2m}{\hbar^2}[\varphi_m+V_d(\mathbf{r})]\right\}^{1/2}dz$$

$$\simeq 2\int_{z_1}^{z_2}\left(\frac{2m}{\hbar^2}\varphi_m\right)^{1/2}\left(1+\frac{V_d(\mathbf{r})}{2\varphi_m}\right)dz. \quad (5.15)$$

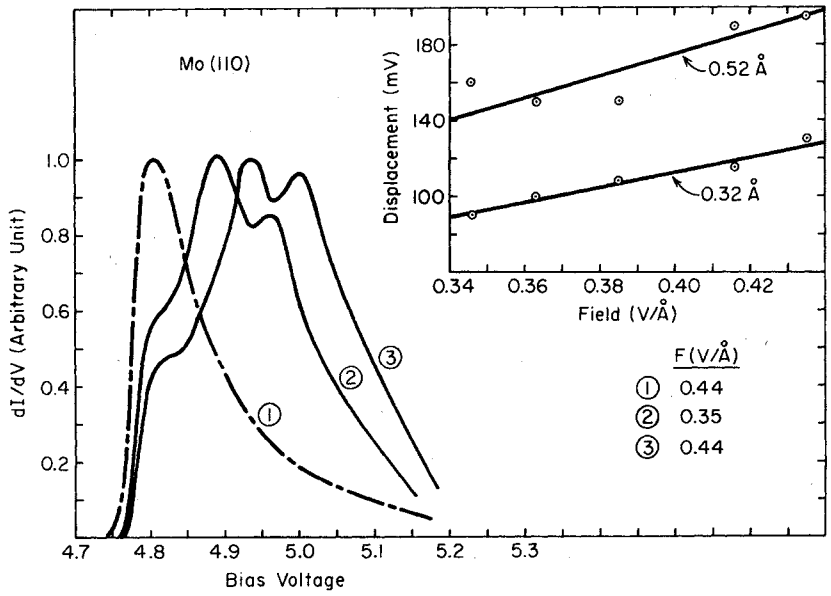

FIG. 44. TED spectra for phthalocyanine on Mo (110); curve 1 is clean. Inset shows small displacement of peaks with field, indicative of an inelastic loss mechanism. (SwCr70.)

Here we note that the classical turning point at z_2 where the electron enters the allowed region in the vacuum is a function of the energy loss. For energy losses in the infrared this is not too serious but for losses in the visible, this correction is important and will make the shape of the inelastic portion of the TED different from that of the elastic part. The first term in the integrand of Eq. (5.15) is just the usual WKB result. Thus the exponential part of the WKB tunneling matrix element squared, can be written

$$D_{\mathrm{WKB}}^{(\mathrm{inel})}(W)=\exp\left(-c+\frac{W}{d}\right)\times\left|\langle\varphi_p\mid\exp\left[-\left(\frac{2m}{\hbar^2}\right)^{1/2}(2\bar{\varphi}_m)^{-1/2}\times\int_{z_1}^{z_2}V_d(\mathbf{r})\,dz\right]\mid\varphi_0\rangle\right|^2,$$

where $\bar{\varphi}_m$ is taken to be a constant of order a "few eV's" in the region in which V_d is important and thus is removed from the integral. Since $V_d\ll\bar{\varphi}$ in the "important" region, the exponential in the molecular matrix element is expanded and only the first nonvanishing term is retained. The resulting matrix element becomes

$$D_{\mathrm{WKB}}^{(\mathrm{inel})}\simeq\exp\left[-c+(W/d)\right]\mid(2m/\hbar^2)^{1/2}\times[\xi(\mathbf{r}_T)/\bar{\varphi}_m^{1/2}]\langle\varphi_p\mid\mu_z\mid\varphi_0\rangle\mid^2,$$

with $\xi(\mathbf{r}_T)=(z_1^2+r_T^2)^{-1/2}-(z_2^2+r_T^2)^{1/2}$. The resulting TED including both elastic and single inelastic tunneling is

$$j'(\epsilon)=(J_0/d)e^{\epsilon/d}\{f(\epsilon)+\sum_p f(\epsilon+\hbar\omega_p)\mid(2m/\hbar^2)^{1/2}\times(2\pi\ln\beta/\bar{\varphi}_m^{1/2})\langle\varphi_p\mid\mu_z\mid\varphi_0\rangle\mid^2\},\quad(5.16)$$

with $2\pi\ln\beta$ the value of $\xi(\mathbf{r}_T)$ averaged over the emitting area and $\ln\beta\sim O(1)$. The structure of this final result which follows from the theory of Scalapino and Marcus (ScMa67) and of Flood (Fl70) shows that the TED is the sum of the usual elastic part plus an inelastic replica of the TED at energy $\epsilon+\hbar\omega_p$. The strength of the inelastic part is directly proportional to the square of the dipole matrix element of the localized oscillator and it is through this fact that gas phase results could be of use in the interpretation of inelastic FEED. One point of caution concerns the assumptions leading to Eq. (5.16). The energy dependence of z_2 must be included for large values of $\hbar\omega_p$ (BrDa70). Also, modifications to the WKB tunneling probability as discussed in Sec. 3 must be included when $\hbar\omega_p\sim\epsilon\mid\gtrsim 0.5$ eV. These can lead to nontrivial changes in the shape of the TED.

5.3a. Organic Molecules

Swanson and Crouser have reported extensive results for the organic molecules phthalocyanine, pentacene, and anthracene deposited on various faces of W and Mo (SwCr70). Their hope was to see and interpret structure in the TED as being due to either resonance tunneling, inelastic vibrational excitation, or inelastic electron excitation within the molecule. The criteria for placing a given peak in one of these categories was taken to be the degree of field dependence of the peak position. Since electron levels at energy E_φ shift with field as $E_\varphi=E_0-eFz$, $dE_\varphi/d(-eF)=z$ should be of the order of the molecule–solid separation if resonance tunneling is the mechanism. On the other hand, vibrational levels shift very little with field. No *a priori* rule can be given for electron excitation in the molecule. A typical set of TED curves by S–C is shown in Fig. 44 for phthalo-

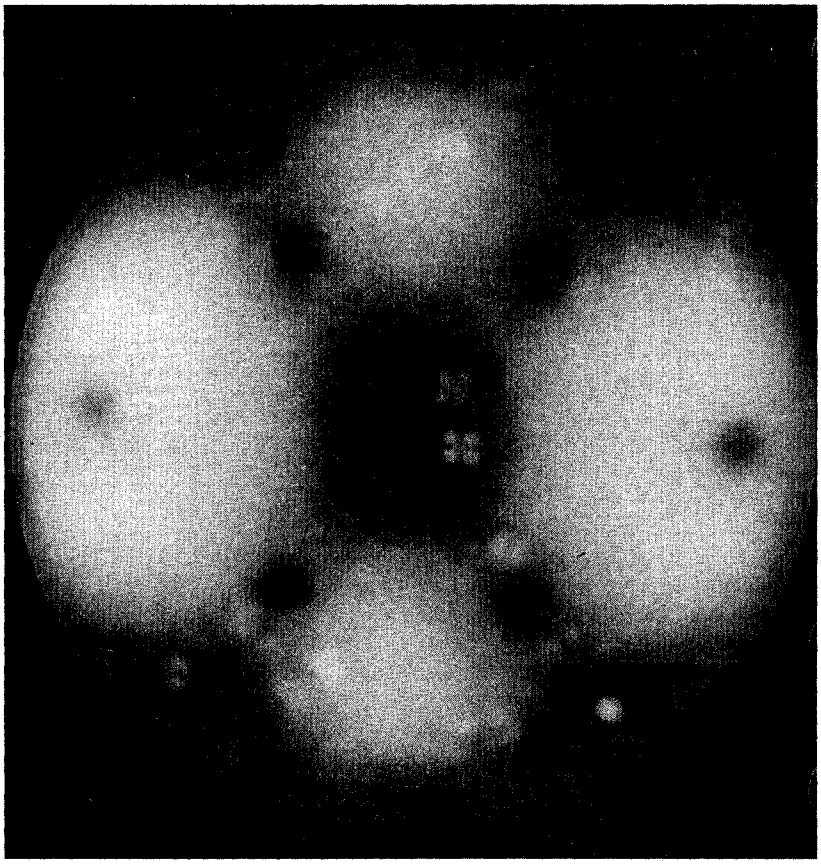

FIG. 45. Field electron micrograph of copper phthalocyanine molecules adsorbed on tungsten at 78 K (compliments of A. J. Melmed).

cyanine on the (110) plane of Mo. Plotted in the inset are the shifts of the low-lying peaks as the field is varied. The slopes of these lines are too small to be elastic resonance tunneling so inelastic tunneling seems to be the mechanism. Although not too much can be said about the shape of the inelastic peaks, they are not inconsistent with a replication of the Fermi level peak shifted down in energy by the characteristic vibrational frequency. S–C offer many more such TED's which are reproducible in the sense that they all have dramatic structure, but are not reproducible in the sense that the position, relative peak heights, and field shifts bear little resemblance to each other from run to run. As S–C point out this is probably due to a multitude of experimental problems. The current of the probe hole (in their retarding potential analyzer) was occasionally very noisy and erratic due to thermally or field induced random steric changes in the adsorbate–substrate configuration which altered the TED structure. Furthermore it was difficult to position the probe hole over a single molecular spot; thus two or more molecules with different steric configurations may have been contributing to the total TED. Also, the large combination of inelastic and elastic tunneling channels could interfere and couple in manners not understood at this time to produce such results. In any event, these experiments have shown that inelastic FEED is a possible tool for investigating vibrational modes of adsorbed molecules and has pointed the direction for systematic studies of simpler systems.

The imaging process, in the field electron emission microscope, for large molecules has continuously been a topic of debate (DD56). There is not a convincing single argument which explains both the cause of the large magnification ($\sim$15) and the shape of the image. With the total energy distribution data of Swanson and Crouser in hand we can finally settle some of the questions. In most of their energy distributions from phthalocyanine, pentacene, and anthracene on both tungsten and molybdenum the major portion of the total current does not originate at the Fermi energy. Therefore the imaging process is not simply a field enhancement effect. The pattern observed on the screen is a scattering pattern, composed of different combinations of elastically or inelastically scattered electrons. The large magnification and image shape reflect the angular dependence of the scattering.

It is appropriate to end this section with the quotation

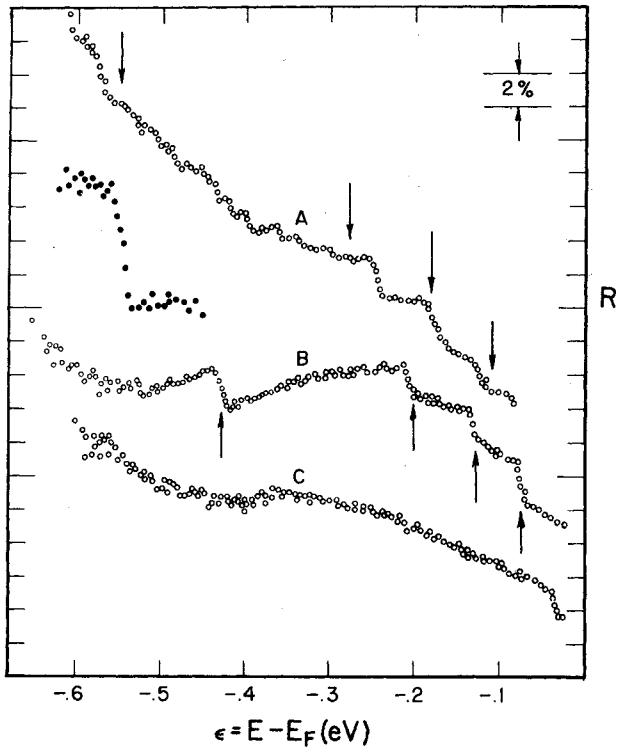

FIG. 46. Enhancement factor $R(\epsilon)$ for hydrogen and deuterium adsorption. Curve A is for saturation adsorption of hydrogen on (111) W at 78 K, after the γ state was removed. The segment of a curve indicated by the dark circles is the signal from the molecular γ state of hydrogen. Curve B is for the saturation of deuterium on the (111) plane at 78 K. The molecular vibrational modes are at ~0.4 eV for deuterium and ~0.55 eV for hydrogen on the (100) plane of tungsten at 300 K, indicating no molecular vibrational modes. (PBe72.)

of a statement made by Müller in 1953 (DD56) which rather well described the process we have outlined above. The reference to a doublet or quadruplet refers to the symmetry of the molecular image. We have included in Fig. 45 an image of phthalocyanine on tungsten.

> "An important observation is that the two parts of a doublet or the four of a quadruplet always have exactly the same intensity. This could not be expected if the pattern were mainly determined by the exterior electrostatic field close to the molecule. The adsorption takes place at the edge of a lattice step, which causes an asymmetric shielding. However, this local field distortion would be less disturbing if we consider the image as a scattering pattern. Then the electron wave is primarily scattered inside the large molecule and is divided into two or four beams. Slow electron scattering on gases has not yet been extensively investigated, but we know that scattering angles of 90 degrees can occur....
>
> The high intensity of the molecule images requires a special mechanism for the emission process. Since the large erected molecule does not approach the metal surface very closely, the energy levels inside the molecule are not widened to a large extent. With ionization potentials higher than the work function of the substrate metal, the occupied zone lies below the Fermi level in the one-dimensional box model. In this level we have a forbidden zone inside the molecule. The application of the electric field causes the levels to be tilted in such a manner that the next originally unoccupied band lies partly below the Fermi level and is being filled up by substrate electrons tunneling through the forbidden zone. From this reservoir, electrons can easily tunnel through the small potential hump in front of the molecule to give the observed large current density."

5.3b. Hydrogen

The work of Lamb and Jaklevic (JLa66, LaJ68) demonstrated that polyatomic molecules in the tunneling barrier are capable of inelastically scattering tunneling electrons in a metal–oxide–metal junction. Swanson and Crouser (SwCr70) demonstrated (previous section) that this mechanism of inelastic tunneling is important when polyatomic molecules are adsorbed on a field emitter. Another application of this concept is to simple molecules chemisorbed on specific faces of a field emitter. The problem will now be one of sensitivity since the cross sections will be small, but the obvious advantages of this type of surface molecular spectrometry, spanning a wide range of wavelengths from the microwave to the visible, is surely worth some effort in signal processing. The work of Plummer and Bell (PBe72) was the first to show vibrational spectra of simple adsorbed molecules at the metal vacuum interface. The success in this experiment was due solely to the much improved signal-to-noise ratio of the electrostatic deflection analyzer (KP72).

P–B attempted to determine from the inelastic tunneling spectrum if hydrogen (deuterium) was molecularly adsorbed in the β_1 state on the (100) face of tungsten (see Fig. 38). If hydrogen (deuterium) was adsorbed as a molecule one would expect to see a step in the $R(E)$ curve at $\epsilon = -\hbar\omega$, where $\hbar\omega$ is the excitation energy of the first vibration mode (~0.55 eV for H_2 and ~0.4 for D_2). Since the threshold effect in the $R(E)$ curve predicted by Eq. (5.13) will be very small these curves must be amplified by at least a factor of one hundred from those emphasizing resonance tunneling effects such as in Fig. 38. Figure 46 shows several enhancement factor curves $R(\epsilon)$ for hydrogen and deuterium adsorption on both the (111) and (100) faces of tungsten.

Curve C of Fig. 46 was obtained after saturating the (100) plane with deuterium at 300 K and then cooling to 78 K to reduce the noise. There is no sign of an inelastic loss at ~0.4 eV. If the β_1 state is molecular, then

for the experimental signal-to-noise ratio and for the coverage given by Tamm and Schmidt (TaSc69, 70), the maximum cross section would be $\sim 5\times 10^{-19}$ cm^{-2}. In order to determine whether the cross section is small or the β_1 state is atomic, another state which should be molecular was checked. The γ state on the (111) plane, which builds in below room temperature, should definitely be molecular (TaSc69, 70, Ma72). Curve B of Fig. 46 shows the enhancement factor R for deuterium saturation on the (111) plane of tungsten at 78 K. There are at least four losses indicated by the arrows. If the tip is warmed to approximately 200 K the energy loss at 0.4 eV, which is the vibration mode of the molecule, disappears, leaving the other modes relatively unchanged. These modes are the deuterium–tungsten modes. The equivalent experiment for the γ state of hydrogen is shown by the segment of the curve in dark circles near 0.55 eV. Curve A is the hydrogen case when nearly all the γ state is removed. The arrows indicate where the hydrogen-tungsten modes should be if they were shifted by $\sqrt{2}$ from the deuterium case (Curve B). The differences between the positions of the arrows and the losses in Curve A might result from the fact that the surface density of hydrogen in Curve A is not the same as the density of deuterium in Curve B.

Excitation of molecularly adsorbed hydrogen and deuterium can be seen and the calculated cross section using Tamm and Schmidt's coverage data is $\sim 4\times 10^{-18}$ cm^2. If the cross section is the same on the (100) plane, then there is less than 2% molecular hydrogen on the (100) plane at saturation coverage and 300 K. The data in Fig. 46 proves that it is possible to measure vibrational energy level spectra for small chemisorbed molecules or atoms if small contrast signals can be detected. This technique appears promising for the resolution of many questions concerning the chemical nature of species in a given binding state.

6. ADDENDA

Since completion of this manuscript, several new works pertaining to FEED have appeared in the literature. Here we make brief mention of the major messages as they relate to the content of the review.

Caroli, Lederer, and Saint James (CLS72) have presented a theory of resonance tunneling through chemisorbed atoms based upon a new approach to tunneling theory within a tightbinding framework. Their theory includes the effects of the applied field on the chemisorption system being studied.

Ngai (Ng72) has published the details of his theory of the field emission tails discussed in Sec. 4.4b.

Czyzewski (Cz72) studied the effects of temperature on the energy distribution from (012) W and offered a qualitative interpretation of the results in terms of electron–phonon scattering.

Photo-field emission experiments using laser light have been performed by Vorburger, Waclawski, and Plummer (VWP73) who observed mainly thermal heating effects and by Lee (L73) who observed photoemission near the top of the field emission barrier.

Theophilou and Modinos (TM 72) have considered the effects of the screening charge induced on the emitter surface by the applied field and have calculated changes in the tunneling barrier. They found that at the field strengths typically used in FEED, the corrections are very small.

Gadzuk and Plummer (GaP73) have presented elsewhere, a review of FEED adsorption studies which follows closely the experimental sections of Sec. 5 of this review.

ACKNOWLEDGMENTS

We wish to express our sincere appreciation to the two people at the National Bureau of Standards without whom the field emission energy distribution work would have been impossible; firstly, Dr. R. D. Young who gave birth to it all and who formed the critical nucleus of one which brought us together; secondly, Dr. C. E. Kuyatt who provided both a Mr. Wizard type of inquisitiveness which spurred us onward and also a superb electron energy analyzer.

To our many other colleagues who offered stimulation, ideas, and challenges, we thank them collectively.

REFERENCES

AB63 V. Ambegaokar and A. Baratoff, Phys. Rev. Lett. **10**, 486 (1963); (E) **11**, 104 (1963)

AdGe70 D. L. Adams and L. H. Germer, Surf. Sci. **23**, 419 (1970).

AdGeMa70 D. L. Adams, L. H. Germer, and J. W. May, Surf. Sci. **22**, 45 (1970).

An61 P. W. Anderson, Phys. Rev. **124**, 41 (1961); and in *Many-Body Physics*, edited by C. DeWitt and R. Balian (Gordon and Breach, New York, 1969).

An66 P. W. Anderson, Phys. Rev. Lett. **17**, 95 (1966).

Ap66, 67 J. Appelbaum, Phys. Rev. Lett. **17**, 91 (1966); Phys. Rev. **154**, 633 (1967).

ApBr69 J. Appelbaum and W. F. Brinkman, Phys. Rev. **186**, 464 (1969).

ApBr70 J. A. Appelbaum and W. F. Brinkman, Phys. Rev. B **2**, 907 (1970).

B36, 40 J. Bardeen, Phys. Rev. **49**, 653 (1936); **58**, 727 (1940).

B61 J. Bardeen, Phys. Rev. Lett. **6**, 502 (1961).

B63 G. A. Burdick, Phys. Rev. **129**, 138 (1963).

BaBuCaSi70 U. Banninger, G. Busch, M. Campagna, and H. C. Siegmann, Phys. Rev. Lett. **25**, 585 (1970).

BeDu69 A. J. Bennett and C. B. Duke, Phys. Rev. **188**, 1060 (1969).

BeFa66 A. J. Bennett and L. M. Falicov, Phys. Rev. **151**, 512 (1966).

BKH53 R. F. Burgess, H. Kroemer, and J. M. Houston, Phys. Rev. **90**, 515 (1953).

Bl69 *Tunneling Phenomena in Solids*, edited by E. Burstein and S. Lundqvist (Plenum Press, New York, 1969).

Bo51 D. Bohm, *Quantum Theory* (Prentice-Hall, Englewood Cliffs, N. J., 1951), pp. 242–295.

BrDa70 A. D. Brailsford and L. C. Davis, Phys. Rev. B **2**, 1708 (1970).

BuCaSi71 G. Busch, M. Campagna, and H. C. Siegmann, Phys. Rev. B **4**, 746 (1971).

CDa64 P. H. Cutler and J. C. Davis, Surf. Sci. **1**, 194 (1964).

CFP62 M. M. Cohen, L. M. Falicov, and J. C. Phillips, Phys. Rev. Lett. **8**, 316 (1962).

CGi58 P. H. Cutler and J. J. Gibbons, Phys. Rev. **111**, 394 (1958).

Ch66 S. G. Christov, Phys. Stat. Sol. **17**, 11 (1966).

ChStSM64 F. M. Charbonnier, R. W. Strayer, L. W. Swanson, and E. E. Martin, Phys. Rev. Lett. **13**, 397 (1964).

Cl71 H. E. Clark, Ph.D. thesis, American University, Washington, D.C. (August 1971).

CLS72 C. Caroli, D. Lederer, and D. Saint James, Surf. Sci. **33**, 228 (1972).

ClY68 H. E. Clark and R. D. Young, Surf. Sci. **12**, 385 (1968).

CNa65 P. H. Cutler and D. Nagy, Surf. Sci. **3**, 71 (1965).

Co67 J. W. D. Connolly, Phys. Rev. **154**, 415 (1967).

Con71 J. N. L. Connor, Phys. Rev. B **3**, 1050 (1971).

CrSz67 C. R. Crowell and S. M. Sze, Phys. Thin Films **4**, 325 (1967).

Cz72 J. J. Czyzewski, Surf. Sci. **33**, 589 (1972).

DaDu69 L. C. Davis and C. B. Duke, Phys. Rev. **184**, 764 (1969).

DCoo66 I. J. D'Haenens and E. A. Coomes, Phys. Rev. Lett. **17**, 516 (1966).

DD56 W. P. Dyke and W. W. Dolan, Adv. Electron. Electron Phys. **8**, 89 (1956).

DeEh65 T. A. Delchar and G. Ehrlich, J. Chem. Phys. **42**, 2686 (1965).

DMH35 R. K. Dahlstrom, K. V. Mackenzie, and J. E. Henderson, Phys. Rev. **48**, 484 (1935).

Do67 L. N. Dobretsov, Fiz. Tverd. Tela **9**, 2769 (1967) [English transl.: Sov. Phys.—Solid State **9**, 2177 (1968)].

DoDy54 W. W. Dolan and W. P. Dyke, Phys. Rev. **95**, 327 (1954).

DoLe69 C. B. Dover and R. H. Lemmer, Phys. Rev. **183**, 908 (1969).

DoSu70 S. Doniach and M. Sunjic, J. Phys. C. Solid State Phys. **3**, 285 (1970).

Du69 C. B. Duke, *Tunneling in Solids* (Academic, New York, 1969).

Du69a C. B. Duke, J. Vac. Sci. Technol. **6**, 152 (1969).

DuAl67 C. B. Duke and M. E. Alferieff, J. Chem. Phys. **46**, 923 (1967).

DuF72 C. B. Duke and J. Fauchier, Surf. Sci. **32**, 175 (1972).

E66 G. Ehrlich, Ann. Rev. Phys. Chem. **17**, 295 (1966).

EAn66 P. J. Estrup and J. Anderson, J. Chem. Phys. **45**, 2254 (1966).

EcNg71 E. N. Economou and K. L. Ngai, Phys. Rev. B **4**, 4105 (1971).

EDK61 M. I. Elinson, F. F. Dobriakova, and F. F. Krapivin, Radiotekhn. i Elektron. **6**, 1342 (1961) [Radio Eng. Electron Phys. USSR **6**, 1191 (1961)].

EnC67 I. Engle and P. H. Cutler, Surf. Sci. **8**, 288 (1967).

EnGo70 T. Engel and R. Gomer, J. Chem. Phys. **52**, 1832 (1970).

Er65 W. Ermrich, Philips Res. Rep. **20**, 94 (1965).

ErOo67 W. Ermrich and A. van Oostrom, Solid-State Commun. **5**, 471 (1967).

Ev67 T. E. Everhart, J. Appl. Phys. **38**, 4944 (1967).

Fa61 U. Fano, Phys. Rev. **124**, 1866 (1961).

FeMa66 P. A. Fedders and P. C. Martin, Phys. Rev. **143**, 245 (1966).

Fi70 T. E. Fischer, 30th Annual Physical Electronics Conference, Milwaukee, Wisc. (March 1970).

Fl51 G. C. Fletcher, Proc. Phys. Soc. (London) **65**, 192 (1951).

Fl69, 70 D. J. Flood, Phys. Lett. **A29**, 100 (1969); J. Chem. Phys. **52**, 1355 (1970).

FN28 R. H. Fowler and L. W. Nordheim, Proc. Roy. Soc. Lond. **A119**, 173 (1928).

Fo70 F. Forstmann, Z. Phys. **235**, 69 (1970).

FoHe70 F. Forstmann and V. Heine, Phys. Rev. Lett. **24**, 1419 (1970).

FoPe70 F. Forstmann and J. B. Pendry, Z. Phys. **235**, 75 (1970).

FrFr65 N. Fröman and P. O. Fröman, *JWKB Approximation: Contributions to the Theory* (North-Holland, Amsterdam, 1965).

Ga67 J. W. Gadzuk, Surf. Sci. **6**, 133 (1967); **6**, 159 (1967).

Ga69 J. W. Gadzuk, Surf. Sci. **15**, 466 (1969).

Ga69a J. W. Gadzuk, Phys. Rev. **182**, 416 (1969).

Ga70 J. W. Gadzuk, Phys. Rev. B **1**, 2110 (1970).

Ga70a J. W. Gadzuk, J. Appl. Phys. **41**, 286 (1970).

Ga70b J. W. Gadzuk, Surf. Sci. **23**, 58 (1970).

Ga71 J. W. Gadzuk, Phys. Rev. B **3**, 1772 (1971).

Ga72 J. W. Gadzuk, J. Vac. Sci. Technol. **9**, 591 (1972).

GaHaRh71 J. W. Gadzuk, J. K. Hartman, and T. N. Rhodin, Phys. Rev. B **4**, 241 (1971).

GaLu73 J. W. Gadzuk and A. A. Lucas, Phys. Rev. (to be published).

GaP71 J. W. Gadzuk and E. W. Plummer, Phys. Rev. B **3**, 2125 (1971).

GaP71a J. W. Gadzuk and E. W. Plummer, Phys. Rev. Lett. **26**, 92 (1971).

GaP73 J. W. Gadzuk and E. W. Plummer in *Solid State Surface Science*, edited by M. Green (Marcel Dekker, New York, 1973), Vol. 3.

GaPClY69 J. W. Gadzuk, E. W. Plummer, H. E. Clark, and R. D. Young, in *Proceedings of the 3rd Materials Research Symposium, Electronic Density of States*, edited by L. H. Bennett, NBS Special Report 323.

Gi60 I. Giaever, Phys. Rev. Lett. **5**, 147 (1960); **5**, 464 (1960).

Gl71 M. L. Glasser, Phys. Rev. B **3**, 1772 (1971).

GlReSi71 W. Gleich, G. Regenfus, and R. Sizman, Phys. Rev. Lett. **27**, 1066 (1971).

GM56 R. H. Good and E. W. Müller in *Handbuch der Physik*, edited by S. Flügge (Springer–Verlag, Berlin, 1956), Vol. 21, p. 176.

Go61 R. Gomer, *Field Emission and Field Ionization* (Harvard U. P., Cambridge, Mass., 1961).

Gl70 R. Gomer, Surf. Sci. **22**, 445 (1970).

GoKul67 G. A. Gogadze and J. O. Kulik, Fiz. Metal. Metalloved. **23**, 606 (1967).

Gr70 H. F. Gray, Phys. Rev. B **1**, 2842 (1970).

Gr71 T. B. Grimley, J. Vac. Sci. Technol. **8**, 21 (1971).

Gu35 R. W. Gurney, Phys. Rev. **47**, 479 (1935).

GuMu40 E. Guth and C. J. Mullin, Phys. Rev. **59**, 575 (1940).

H61 W. A. Harrison, Phys. Rev. **123**, 85 (1961).

Ha66 H. D. Hagstrum, Phys. Rev. **150**, 495 (1966).

HB31 J. E. Henderson and R. E. Badgley, Phys. Rev. **38**, 540 (1931).

He70 V. Heine, in *Proceedings of Tenth International Conference on the Physics of Semiconductors*, U.S.A.E.C. CONF-700801 (Aug. 1970).

Hee69 A. J. Heeger, Solid State Phys. **23**, 283 (1969).

HeLu69 L. Hedin and S. Lundqvist, Solid State Phys. **23**, 1 (1969).

HeN49 C. Herring and M. H. Nichols, Rev. Mod. Phys. **21**, 185 (1969).

Her70 C. Herring (private communication) (1970).

HMF65 *Handbook of Mathematical Functions*, Natl. Bur. Std., Appl. Math. Series 55 (U. S. GPO, Washington, D. C., 1965), p. 437.

Ho67 A. A. Holscher, Ph.D. thesis, Univ. of Leiden (1967).

HoEL66 L. Hodges, H. Ehrenreich, and N. D. Lang, Phys. Rev. **152**, 505 (1966).

Hu71 J. P. Hurrault, J. Phys. (Paris) **32**, 421 (1971).

I63, 64 L. V. Iogansen, Zh. Eksp. Teor. Fiz. **45,** 207 (1963); **47,** 270 (1964) [English transls.: Sov. Phys.—JETP **18,** 146 (1969); **20,** 180 (1965)].

I66, 67 F. I. Itskovich, Zh. Eksp. Teor. Fiz. **50,** 1425 (1966); **52,** 1720 (1967 [English transl.: Sov. Phys.—JETP **23,** 945 (1966); **25,** 1143 (1967)].

JLa66 R. C. Jaklevic and J. Lambe, Phys. Rev. Lett. **17,** 1138 (1966).

Ju53 H. J. Juretschke, Phys. Rev. **92,** 1140 (1953).

JK68 R. Klein, Surf. Sci. **11,** 227 (1968); **11,** 430 (1968).

Ka61 E. O. Kane, J. Appl. Phys. **32,** 83 (1961).

Ka70 H. Kanter, Phys. Rev. B **1,** 522 (1970).

Ke37 E. C. Kemble, *The Fundamental Principles of Quantum Mechanics* (McGraw-Hill, New York, 1937), p. 100.

KMaYa71 D. A. King, T. E. Madey, and J. T. Yates, J. Chem. Phys. **55,** 3236 (1971).

Ko69 J. Kondo, Solid State Phys. **23,** 183 (1969).

Ko72 F. Kormendi, J. Phys. Chem. Solids **33,** 157 (1972).

KP72 C. E. Kuyatt and E. W. Plummer, Rev. Sci. Instrum. **43,** 108 (1972).

KSi66, 67 C. E. Kuyatt and J. A. Simpson, J. Appl. Phys. **37,** 3805 (1966); Rev. Sci. Instrum. **38,** 103 (1967).

L71 N. D. Lang, Solid State Commun. **9,** 1015 (1971).

L71a M. J. G. Lee, CRC Crit. Rev. Solid State Sci. **2,** 85 (1971).

L73 M. J. G. Lee (to be published).

LaJ68 J. Lambe and R. C. Jaklevic, Phys. Rev. **165,** 821 (1968).

Le71 M. C. Leung, Phys. Lett. **35A,** 126 (1971).

Leg68 A. Leger, J. Phys. (Paris) **29,** 646 (1968).

LeGo70 C. Lea and R. Gomer, Phys. Rev. Lett. **25,** 804 (1970).

LeGo71 C. Lea and R. Gomer, J. Chem. Phys. **54,** 3349 (1971).

LK70, 71 N. Lang and W. Kohn, Phys. Rev. B **1,** 4555 (1970); **3,** 1215 (1971).

LL60 L. D. Landau and E. M. Lifshitz, *Mechanics* (Addison-Wesley, Reading, Mass., 1960).

LiO'M70 B. A. Lippman and T. F. O'Malley, Phys. Rev. A **2,** 2115 (1970).

Lo65 T. L. Loucks, Phys. Rev. Lett. **14,** 693 (1965).

Lu67, 68 B. I. Lundqvist, Physik Kon. Mat. **6,** 206 (1967); **7,** 117 (1968).

LuWi72 B. Lundqvist, K. Mountfried, and J. W. Wilkins, Sol. State Commun. **10,** 383 (1972).

M36 E. W. Müller, Z. Phys. **102,** 734 (1936).

M37 E. W. Müller, Z. Phys. **106,** 541 (1937).

M56 E. W. Müller, Z. Naturforsch. **11a,** 88 (1956).

M60 E. W. Müller, Adv. Electron. Electron Phys. **13,** 83 (1960).

M67 E. W. Müller, Ann. Rev. Phys. Chem. **18,** 35 (1967).

Ma65 L. F. Mattheiss, Phys. Rev. **139,** A1893 (1965).

Ma67 G. D. Mahan, Phys. Rev. **163,** 612 (1967).

Ma72 T. E. Madey, Surf. Sci. **29,** 571 (1972).

MaDu66 G. D. Mahan and C. B. Duke, Phys. Rev. **149,** 705 (1966).

MaYa70 T. E. Madey and J. T. Yates, Jr., in *Structure et Properties des Surface des Solids* (Editions du Centre National de la Recherche Scientifique, Paris, 1970), No. 187, p. 155.

Mc71 J. T. McKinney (private communications).

McRo68 W. L. McMillen and J. M. Rowell, in *Treatise on Superconductivity,* edited by R. D. Parks (Marcel Dekker, New York, 1968).

Me61 E. Merzbacher, *Quantum Mechanics* (Wiley, New York, 1961), pp. 121–130.

Me62 C. A. Mead, Phys. Rev. Lett. **8,** 56 (1962); **9,** 46 (1962).

MG53 S. C. Miller and R. H. Good, Jr., Phys. Rev. **91,** 174 (1953).

Mo70, 70a A. Modinos, Surf. Sci. **20,** 55 (1970); **22,** 473 (1970).

MoNi69, 71 A. Modinos and N. Nicolaou, Surf. Sci. **17,** 359 (1969); J. Phys. C **4,** 2875 (1971).

MoTh71 A. Modinos and A. Theophilou, J. Phys. C **4,** 338 (1971).

MurG56 E. L. Murphy and R. H. Good, Jr., Phys. Rev. **102,** 1464 (1956).

N28 L. W. Nordheim, Proc. Roy. Soc. Lond. **A121,** 626 (1928).

NaC69 D. Nagy and P. H. Cutler, Phys. Rev. **186,** 651 (1969).

Neu69 H. Neumann, Physica **44,** 587 (1969).

Ne69 D. M. Newns, Phys. Rev. **178,** 1123 (1969).

Ne69a D. M. Newns, J. Chem. Phys. **50,** 4572 (1969).

Ng72 K. L. Ngai, Phys. Stat. Sol. (b) **53,** 309 (1972).

NgBa71 K. L. Ngai and R. A. Bari, Bull. Am. Phys. Soc. **16,** 431 (1971).

NiMo71 N. Nicolaou and A. Modinos, J. Phys. C **4,** 2859 (1971).

NoDe69 P. Nozieres and C. T. DeDominicis, Phys. Rev. **178,** 1097 (1969).

Ob68 G. Obermair, Z. Phys. **217,** 91 (1968).

Oo61 A. van Oostrom, Philips Res. Rep. Suppl. **11,** 102 (1966).

Op28 J. R. Oppenheimer, Phys. Rev. **31,** 66 (1928).

Os71 C. F. Osborne, J. Phys. F **1,** 416 (1971).

P63 R. E. Prange, Phys. Rev. **131,** 1083 (1963).

P70 E. W. Plummer, Proc. of 30th Annual Physical Electronics Conference, Milwaukee, Wisc., March 1970 (unpublished).

P70a E. W. Plummer, Lecture Notes for "Field Ion Microscopy Short Course," Univ. Florida, March 1970 (unpublished).

P71 E. W. Plummer, unpublished data given at Physical Electronics Conference, Gaithersburg, Md. (1971).

PaMe69 G. H. Parker and C. A. Mead, Appl. Phys. Lett. **14,** 21 (1969).

PBe72 E. W. Plummer and A. E. Bell, J. Vac. Sci. Technol. **9,** 583 (1972).

Pe62 J. C. Penley, Phys. Rev. **128,** 596 (1962).

PeGoCo71, 72 D. Penn, R. Gomer, and M. H. Cohen, Phys. Rev. Lett. **27,** 26 (1971); Phys. Rev. B **5,** 768 (1972).

PFe70 J. Politzer and T. E. Feuchtwang, Surf. Sci. **19,** 443 (1970).

PFe71 J. Politzer and T. E. Feuchtwang, Phys. Rev. B **3,** 597 (1971).

PGaY69 E. W. Plummer, J. W. Gadzuk, and R. D. Young, Solid State Commun. **7,** 487 (1969).

PlGa70 E. W. Plummer and J. W. Gadzuk, Phys. Rev. Lett. **25,** 1493 (1970).

Po72 B. Politzer, Ph.D. thesis, Pennsylvania State Univ., Dept. of Phys. (1972).

PoC70 B. Politzer and P. H. Cutler, Surf. Sci. **22,** 277 (1970); Mat. Res. Bull. **5,** 703 (1970).

PoC72 B. Politzer and P. H. Cutler, Phys. Rev. Lett. **28,** 1330 (1972).

PRh68 E. W. Plummer and T. N. Rhodin, J. Chem. Phys. **49,** 3479 (1968).

PY70 E. W. Plummer and R. D. Young, Phys. Rev. B **1,** 2088 (1970).

Q62 J. J. Quinn, Phys. Rev. **126,** 1453 (1962).

QFe58 J. J. Quinn and R. A. Ferrell, Phys. Rev. **112,** 812 (1958).

Ri59 R. H. Ritchie, Phys. Rev. **114,** 644 (1959).

Ri66 R. H. Ritchie, J. Appl. Phys. **37,** 2276 (1966).

RiGoo62 M. H. Rice and R. H. Good, Jr., J. Opt. Soc. Am. **52,** 239 (1962).

S64 R. Stratton, Phys. Rev. **135,** A794 (1964).

S69 J. R. Smith, Phys. Rev. **181,** 522 (1969).

S70 J. R. Smith, Phys. Rev. Lett. **25,** 1023 (1970).

SaDe50 R. G. Sachs and D. L. Dexter, J. Appl. Phys. **21,** 1304 (1950).

SB72 L. W. Swanson and A. E. Bell, Adv. Electron. Electron Phys. **32,** 194 (1973).

Sc66 F. W. Schmidlin, J. Appl. Phys. **37,** 2823 (1966).

Sc72 J. R. Schrieffer, J. Vac. Sci. Technol. **9,** 561 (1972).

ScGo66 L. D. Schmidt and R. Gomer, J. Chem. Phys. **45,** 1605 (1966).

ScMa67 D. J. Scalapino and S. M. Marcus, Phys. Rev. Lett. **18,** 459 (1967).

SCr69 L. W. Swanson and L. C. Crouser, in *The Structure and Chemistry of Solid Surfaces,* edited by G. A. Somorjai (Wiley, New York, 1969).

SCrCh66 L. W. Swanson, L. C. Crouser, and F. M. Charbonnier, Phys. Rev. **151,** 327 (1966).

SGo65 L. D. Schmidt and R. Gomer, J. Chem. Phys. **43,** 2035 (1965).

Sh69 W. Shepherd, Ph.D. thesis, Dept. of Elec. Eng., Univ. of Minnesota (1969).

Si61, 64 J. A. Simpson, Rev. Sci. Instrum. **32,** 1283 (1961); **35,** 1968 (1964).

SoBe33 A. Sommerfeld and H. A. Bethe in *Handbuch der Physik,* edited by S. Flügge (Springer, Berlin, 1933), Vol. 24, p. 150.

SoMi61, 63, 64, 64a, 66 I. L. Sokol'skaya and N. V. Mileshkina, Fiz Tverd. Tela **3,** 3389 (1961); **5,** 2501 (1963); **6,** 1786 (1964); **7,** 1043 (1964); **8,** 3163 (1966) [Sov. Phys.—Solid State **3,** 2460 (1962); **5,** 1826 (1964); **6,** 1401 (1964); **7,** 838 (1965)].

SP71 D. P. Smith and W. T. Peria, Physical Electronics Conference, Gaithersburg, Md. (March 1971).

SwCr66, 67 L. W. Swanson and L. C. Crouser, Phys. Rev. Lett. **16,** 389 (1966); **19,** 1179 (1967); Phys. Rev. **163,** 622 (1967).

SwCr68 L. W. Swanson and L. C. Crouser, Final Report NASA Contract NASW-1516 (December 1968).

SwCr70 L. W. Swanson and L. C. Crouser, Surf. Sci. **23,** 1 (1970).

T71 C. W. Todd, Ph.D. thesis, Cornell Univ., Dept. of Appl. Physics (1971).

Ta64 J. Taylor, Surf. Sci. **2,** 544 (1964).

TaSc69, 70 P. W. Tamm and L. D. Schmidt, J. Chem. Phys. **51,** 5352 (1969); **52,** 1150 (1970); and (to be published).

ThMcMe67 K. K. Thornber, T. C. McGill, and C. A. Mead, J. Appl. Phys. **38,** 2384 (1967).

TM69 T. T. Tsong and E. W. Müller, Phys. Rev. **181,** 530 (1969).

TM72 A. K. Theophilou and A. Modinos, Phys. Rev. B **6,** 801 (1972).

ToRh72 C. J. Todd and T. N. Rhodin, Surf. Sci. (to be published).

TrBl69 J. C. Tracy and J. M. Blakely, Surf. Sci. **15,** 257 (1969).

VWP73 T. V. Vorburger, B. J. Waclawski, and E. W. Plummer, Bull. Am. Phys. Soc. **18,** 392 (1973).

W97 R. W. Wood, Phys. Rev. **5,** 1 (1897).

WhBl69 R. D. B. Whitcutt and B. H. Blott, Phys. Rev. Lett. **23,** 639 (1969).

Wi69 J. W. Wilkins, in BL69.

WoCz71 C. J. Workowski and J. J. Czyzewski, Acta Phys. Polon. **A39,** 523 (1971).

WoLo70 E. L. Wolf and D. L. Losee, Phys. Rev. B **2,** 3660 (1970).

Y59 R. D. Young, Phys. Rev. **113,** 110 (1959).

YC66 R. D. Young and H. E. Clark, Phys. Rev. Lett. **17,** 351 (1966).

YC66a R. D. Young and H. E. Clark, Appl. Phys. Lett. **9,** 265 (1966).

YK68 R. D. Young and C. E. Kuyatt, Rev. Sci. Instrum. **39,** 1477 (1968).

YM59 R. D. Young and E. W. Müller, Phys. Rev. **113,** 115 (1959).

YMu62 R. D. Young and E. W. Müller, J. Appl. Phys. **33,** 91 (1962).

YSc71 K. Yonehara and L. D. Schmidt, Surf. Sci. **25,** 238 (1971).

Z34 C. Zener, Proc. Roy. Soc. Lond. **A145,** 523 (1934).

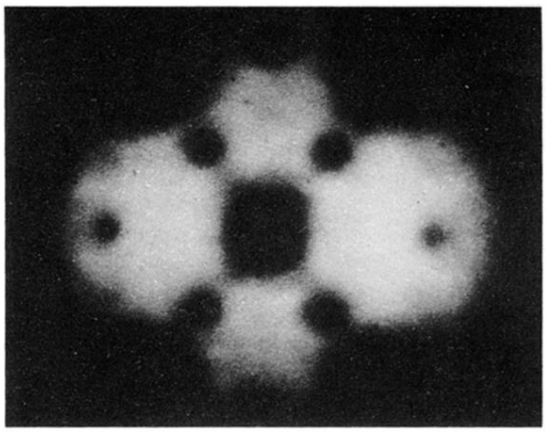

(a)

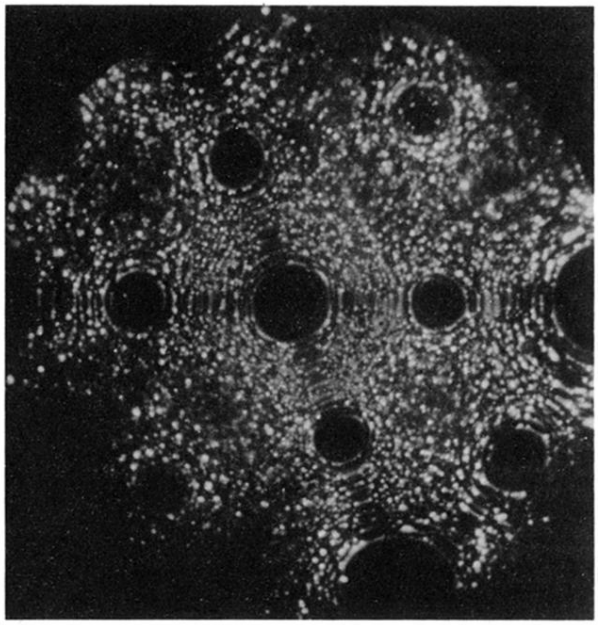

(b)

FIG. 2. (a) Field emission micrograph looking down the (110) plane of a W emitter. The dark (light) regions are high (low) work function or low (high) field planes. (b) Field ion micrograph of the same configuration with the tip cleaned by thermal annealing. (Courtesy of A. Melmed.)

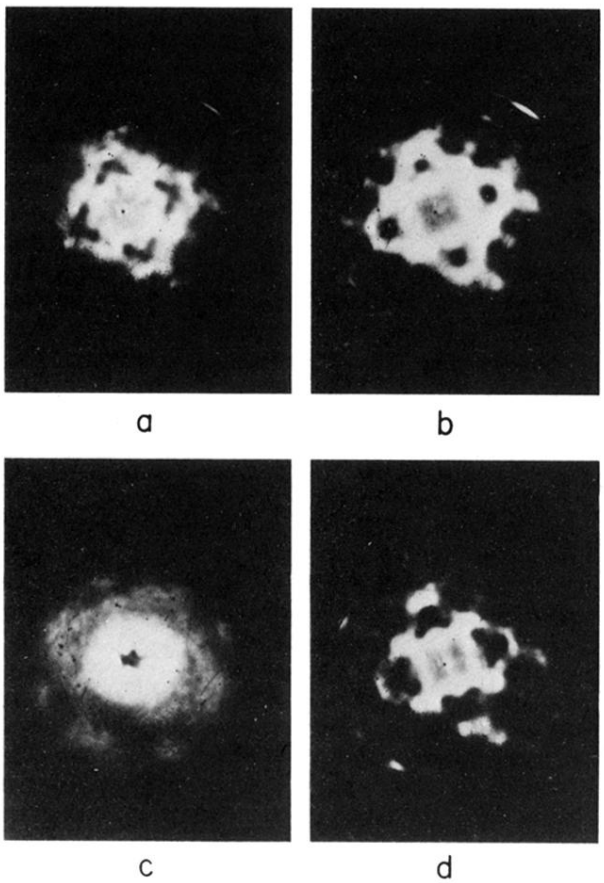

FIG. 24. Ge field emission patterns from test microscope. (a, b) Incompletely cleaned; (a) partial anneal, (b) full anneal. (c, d) Emitter not completely rounded; (c) field evaporated from too rapid field evaporation, (d) clean, annealed. (Sh69.)

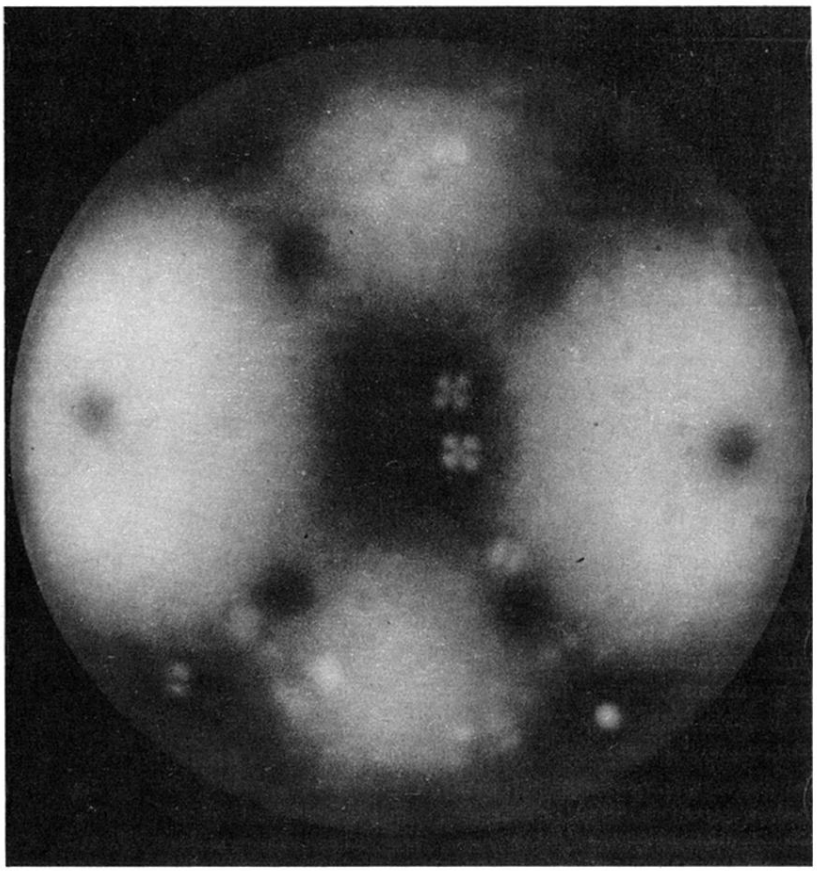

FIG. 45. Field electron micrograph of copper phthalocyanine molecules adsorbed on tungsten at 78 K (compliments of A. J. Melmed).